Physical Optics Modeling of AMC Checkerboard Surfaces for RCS-Reduction and Low

Backscattering Retrodirective Array

by

Meshaal A. Alyahya

A Dissertation in Partial Fulfillment
of the Requirement for the Degree
Doctor of Philosophy

Approved October 2020 by the
Graduate Supervisory Committee:

Constantine A. Balanis, Chair
Joseph C. Palais
James T. Aberle
Georgios C. Trichopoulos

ARIZONA STATE UNIVERSITY

December 2020

ABSTRACT

Artificial magnetic conductor (AMC) surfaces have the unique electromagnetic property that the phase of the reflected fields imitate those of perfect magnetic conductors (PMCs). When a perfect electric conductor (PEC) and an AMC surface are placed on the same plane and illuminated by a plane wave, destructive interference occurs between the fields (due to 180° phase difference between the reflected fields of each surface).

In this dissertation, a design procedure is introduced where a refined algorithm is developed and employed on single-band AMCs leading to a 10-dB RCS-reduction bandwidth of 80%. The AMC circuit model is judiciously utilized to reduce the substrate thickness while simultaneously increasing the bandwidth of the AMC surfaces. Furthermore, dual-band AMC surfaces are synthesized and utilized in combination with single-band AMC surfaces to extend the 10-dB RCS-reduction bandwidth from 80% to about 99%. *Employing the proposed design procedure, a* 99% *bandwidth of 10-dB RCS-reduction bandwidth is achieved while reducing the thickness of the substrate by* 20%.

The second topic of this dissertation aims at analytically modeling the scattering of planar checkerboard surfaces. The high-frequency asymptotic method, Physical Optics (PO), is utilized to analyze the scattering characteristics of complex structures since the PO is computationally efficient and provides intuitive physical insight. Closed-form formulations developed using PO are used to predict the scattering patterns of checkerboard planar surfaces. The PO-based data compare well, along and near specular directions, with simulations by the full-wave Finite Element Method (FEM).

Finally, a Van Atta retrodirective reflector with low backscattering is designed and developed using a microstrip antenna array. Conventional retrodirective reflectors are sensitive to interference by the fields scattered by the antenna structure. By using a virtual feeding network, structural mode scattering is identified and canceled using AMC technology.

To my parents, Ahmed and Badoor and my wife, Walaa

ACKNOWLEDGEMENTS

TABLE OF CONTENTS

LIST OF TABLES

LIST OF FIGURES

Chapter 1

INTRODUCTION

1.1 Motivation

Radar Cross Section (RCS, $\sigma_{\text{3-D}}$) is a far-field parameter that represents the scattering characteristics of a radar target. For a three-dimensional target, the RCS can be expressed as the ratio of the scattered power density (S^s) or fields ($\mathbf{E}^s$, $\mathbf{H}^s$) to the incident power density (S^i) or fields ($\mathbf{E}^i$, $\mathbf{H}^i$) as [1]

$$\sigma_{\text{3-D}} = \lim_{r \to \infty} \left[4\pi r^2 \frac{S^s}{S^i} \right] = \lim_{r \to \infty} \left[4\pi r^2 \frac{|\mathbf{E}^s|^2}{|\mathbf{E}^i|^2} \right] = \lim_{r \to \infty} \left[4\pi r^2 \frac{|\mathbf{H}^s|^2}{|\mathbf{H}^i|^2} \right] \qquad (1.1)$$

where r is the distance between the observation point and the radar target.

RCS reduction is an important objective as it reduces the visibility/signature of the radar target. RCS is also a key factor for antenna characterization, and its reduction is desirable for low-profile applications. In imaging, reducing the RCS of the unwanted background increases the resolution of the image. Since it is critical to control and reduce scattering from radar targets, RCS reduction is an important research area.

1.2 Related Work

The two main techniques for reducing the RCS of a structure are coating it with *radar absorbing materials* (RAMs) and altering its geometry [2]. RAMs contribute to RCS reduction by transforming electromagnetic energy into thermal energy (heat), which is absorbed by lossy material. A classic example of a RAM is the Salisbury screen [3], which is realized by coating the target with a lossy resistive sheet of quarter-wavelength thickness. Ideally,

1

a total absorption of the incident wave is achieved by impedance matching. However, Salisbury screens have a narrow bandwidth, and they add an undesired thickness to the target. The thickness can be reduced when the absorbing sheet is placed on a *magnetic conducting surface* to overcome the quarter-wavelength thickness requirement [4, 5]. Additional techniques to reduce the thickness of radar absorbers have been introduced in [6–8].

The second conventional method for reducing the RCS is to alter the target geometry. The monostatic RCS is reduced by redirecting the scattered electromagnetic waves away from the receiver. However, it often conflicts with aerodynamic requirements of the target. An alternative method, which also reduces the monostatic RCS by redirecting the scattered waves away from the receiver without reshaping the target, is by coating the target with a combination of *perfect magnetic conductors* (PMCs) and *perfect electric conductors* (PECs) to achieve a destructive interference between the fields reflected from each surface. However, since PMCs do not exist in nature, *artificial magnetic conductors* (AMCs), which imitate PMCs at the resonant frequency, can judiciously be used [9, 10].

RCS reduction can be achieved by placing PEC and AMC structures in a checkerboard pattern. Since the phase difference between the reflected fields is 180°, a destructive interference occurs along the specular direction and it redirects the scattered fields of a rectangular plate into four major lobes [11–13]. Furthermore, when the phase difference is within $(180 \pm 37)^\circ$, it achieves a 10-dB RCS reduction compared to that of a PEC structure of the same physical size [13]. Since AMCs are frequency dependent, to improve the 10-dB RCS-reduction bandwidth two different types of AMC surfaces were used to achieve a 63% bandwidth [13]. Furthermore, by selecting the AMC surfaces judiciously, 10-dB RCS-reduction bandwidths of 83% and 91% have been reported [14]. Moreover, broader 10-dB RCS-reduction bandwidths were achieved by further optimizing the AMC surfaces [13–18]. The gain of antennas can be increased, while simultaneously reduce the RCS, using similar approaches [19–22].

2
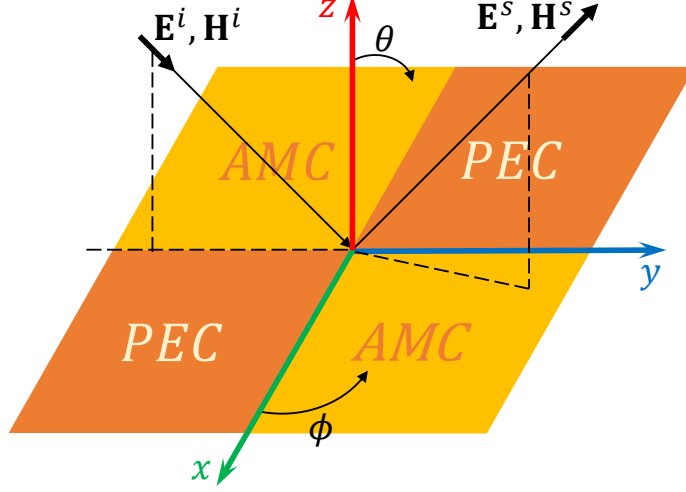
Figure 1.1: A Conventional Checkerboard Type Structure for RCS Reduction.

When a checkerboard surface, as exhibited in Figure 1.1, is illuminated at normal incidence, it redirects the scattered fields into four major lobes away from the normal direction. Conventional array theory can be used to determine the direction of the reflected major lobes for only normal incidence [11]. Furthermore, the angle of incidence is incorporated in the solution for checkerboard surfaces consisting of counter phase elements [0° and 180° phase elements (i.e., PMC and PEC)] [12]. In [23], the array theory-based solution for identifying the directions of the major lobes is further generalized to include the angle of incidence and the reflection phase of each metasurface. Thus, when a plane wave impinges upon a metasurface-based checkerboard surface, the angular directions of the formed major lobes can be found using array theory by [23]

$$\tan \phi_{m,n} = \frac{\sin \theta_i \sin \phi_i \pm (2n+1)\dfrac{\beta_y}{kd_y}}{\sin \theta_i \cos \phi_i \pm (2m+1)\dfrac{\beta_x}{kd_x}} \tag{1.2a}$$

$$\sin^2 \theta_{m,n} = \left[\sin \theta_i \sin \phi_i \pm (2n+1)\frac{\beta_y}{kd_y} \right]^2 + \\ \left[\sin \theta_i \cos \phi_i \pm (2m+1)\frac{\beta_x}{kd_x} \right]^2 \tag{1.2b}$$

3

where $(\theta_{m,n}, \phi_{m,n})$ are the angular directions of the major lobes of order $n+m+1$, while (θ_i, ϕ_i) is the angular direction of the impinging wave. The reflection phase difference between the adjacent AMCs are defined as β_x and β_y along x and y directions, respectively. In this case, the directions of the four major lobes $(\theta_{0,0}, \phi_{0,0})$ for the scattered fields can be determined by setting $m = n = 0$.

1.3   Scope of This Work

For conventional checkerboard-patterned structures, at least a 10-dB RCS reduction can be achieved by maintaining a phase difference of $(180 \pm 37)°$ between the selected AMCs. Broad bandwidths of RCS reduction are achieved using thick substrate or multiple layers of substrate [24]. Moreover, the performance was examined only along specular directions which is modeled using array theory. RCS reduction along non-specular directions has not yet been notably addressed.

In this dissertation, an advanced algorithm using a circuit model of AMCs is developed for single- and dual-band that leads to 10-dB RCS-reduction bandwidths of 80% and 99%, respectively. By following the proposed guidelines, the thickness of the substrate is reduced by 20% while simultaneously increasing the RCS-reduction bandwidth [24].

Since it is favorable to analyze and reduce scattering in non-specular directions, physical optics (PO) is used to investigate in detail the field scattering from PECs, PMCs, and AMCs planar surfaces. Although, PO is accurate at and near specular directions, it sheds physical insight in the scattering process in all directions. Thus, closed form solutions for RCS are presented for the following:

- Rectangular PMC.

- Two conducting plates (PEC and PMC) of different sizes.

- Two AMCs of different sizes and reflection coefficients.

- Four AMCs of different sizes and reflection coefficients.

The solutions are presented in closed form which can aid in predicting the RCS reduction for a checkerboard-patterned structure with AMCs of different sizes. Moreover, these solutions are computationally efficient, allowing rapid and efficient optimization of architectural AMC checkerboard designs for broadband RCS reduction.

As mentioned earlier, the RCS of any target can be reduced using scattering cancellation (i.e., checkerboard AMCs). Furthermore, it was shown that using the developed PO-based solution, the method of checkerboard RCS reduction can be extended to reduce the RCS of antennas. Using a two-dimensional microstrip-antenna array, a Van Atta retrodirective reflector with low backscattering is synthesized and developed. Conventional retrodirective reflectors are sensitive to the interference by the fields scattering from the antenna structure. Using a virtual feeding network, structural mode scattering is identified and canceled using AMC technology [25].

1.4 Outline of the Dissertation

This dissertation is organized into four chapters. In Chapter 2, checkerboard-patterned AMC structures are presented along with their analytical models. Furthermore, the proposed checkerboard-patterned designs with a 10-dB RCS-reduction of 80% and 99% bandwidths are introduced. Additionally, the process of AMC selection is reviewed. In Chapter 3, PO is introduced and the analysis procedure is reviewed. Closed-form RCS solutions are then presented using PO for planar surfaces of varying number of AMCs. These PO-based analytical results are compared to those obtained using full-wave FEM simulations. To validate the solutions, measurements of monostatic RCS are performed and compared with analytical and simulated data. In Chapter 4, the theory of the Van Atta array and its monostatic RCS are reviewed. Chapter 4 also introduces various design and feeding network topologies and provides detailed steps for simulating the reflector using a virtual feed-

ing network. Conventional retrodirective reflectors are sensitive to the interference by the fields scattered from the antenna structure. Thus, a Van Atta retrodirective reflector with low backscattering is designed and developed using a microstrip antenna array. Finally, Chapter 5 summarizes the work performed in this dissertation. Future work is suggested to the design of a Van Atta retrodirective reflector with low backscattering using aperture-coupled microstrip patch antenna arrays.

Chapter 2

DESIGN OF ULTRA-BROADBAND RCS-REDUCTION CHECKERBOARD

SURFACE USING AMC CIRCUIT MODEL

Checkerboard surfaces utilize a combination of different architecturally patterned artificial magnetic conductor (AMC) ground planes to achieve destructive interference of the scattered fields. In this chapter, artificial magnetic conductors that imitate perfect magnetic conductors (PMCs) at the resonant frequency are reviewed. An analysis of the impact of each parameter (i.e., substrate type, thickness, unit cell size, and patch size) of the AMCs on their design criteria is performed. Based on this analysis, 10-dB RCS-reduction bandwidths of 80% and 99%, respectively, were achieved. Design guidelines for the selection of AMCs have been illustrated to synthesize ultra-broadband RCS reduction checkerboard surfaces.

2.1   Artificial Magnetic Conductors

The reflection coefficients of PEC and PMC ground planes are -1 and +1, respectively; therefore, their ideal surface impedances are zero for PEC and infinity for PMC. Thus, the reflected component of the impinging fields on a PEC ground plane will be 180° out of phase, whereas those reflected from a PMC will be in-phase, compared to the incident wave.

Since PMCs do not exist in nature, artificial surfaces, such as corrugated surfaces and artificial magnetic conductors, are synthesized to resemble the PMC characteristics [1].

2.1.1 Corrugations

The impedance of a surface can be changed by geometrically altering its structure. This can be achieved by adding grooves (corrugations) of a quarter wavelength depth ($l \approx \lambda/4$), as shown in Figure 2.1. The width w and thickness t of the corrugations are ideally $t \leq w/10 \leq \lambda/4$. Using transmission line theory, the input impedance of the corrugated surface is given as [1]:

$$Z_{in} = jZ_c \tan(\beta l) \tag{2.1}$$

If the depth of the corrugations (l) is equal to a quarter wavelength ($l = \lambda/4$), the input (surface) impedance will be very large, ideally infinite. However, corrugated surfaces have very narrow bandwidths and are usually bulky.
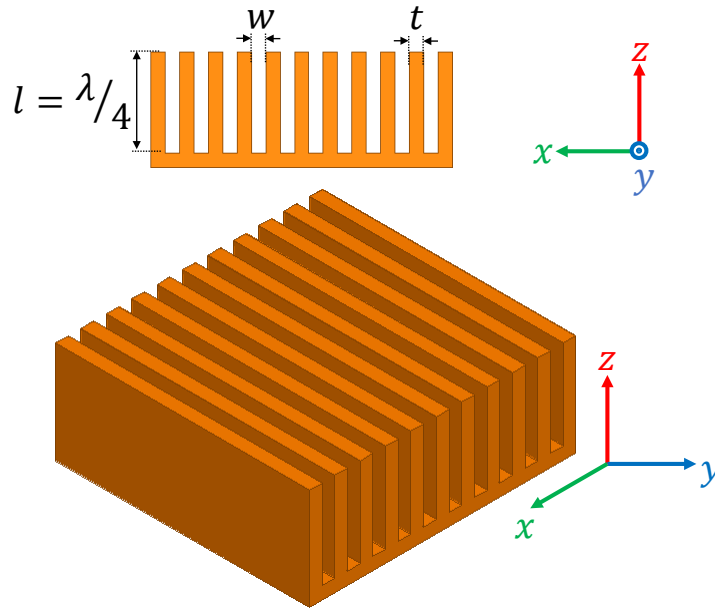
Figure 2.1: Geometry of a Corrugated Surface.

2.1.2 Mushroom Surfaces

Recently, an alternate approach has been introduced to mimic a PMC ground plane response [9,10]. This is achieved by placing a periodic array of square patches on a dielectric-

covered ground plane; different shapes of patches can be used. Vias are used to connect the metallic patches to the ground plane. Figure 2.2 shows a mushroom surface of sixteen unit cells. Each unit cell consists of a patch of width w and gap size g placed on a substrate of thickness h.

(a) Top View.   (b) Side View.
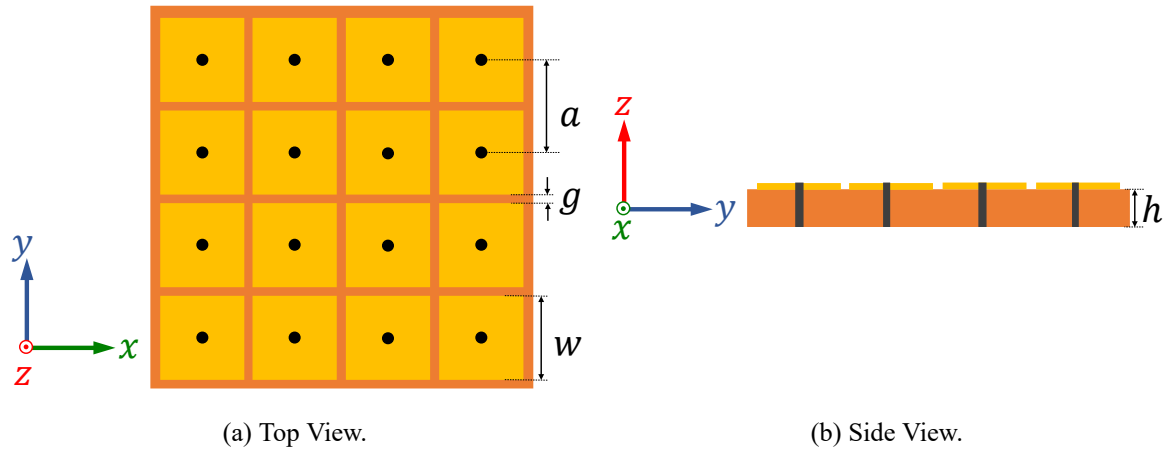
Figure 2.2: Mushroom Surface Geometry.

A unit cell of a mushroom surface is shown in Figure 2.3(a) and its equivalent circuit, when the array periodicity is less than a wavelength, is displayed in Figure 2.3(b).

(a)   (b)
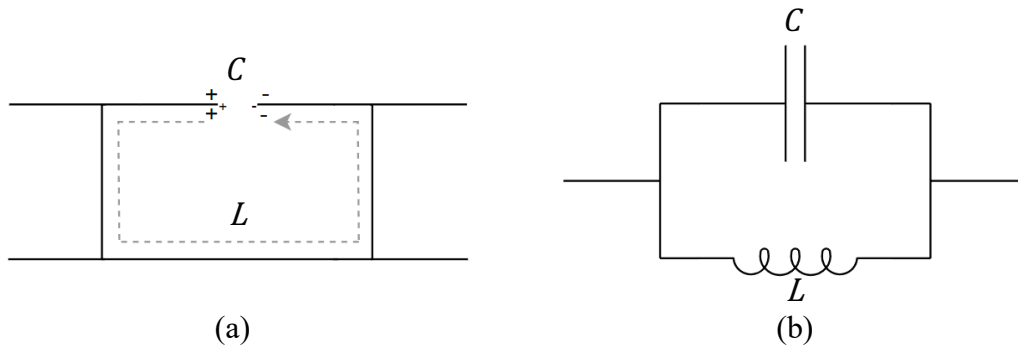
Figure 2.3: (a) Unit Cell. (b) Equivalent Circuit of a Mushroom Surface.

The capacitance is primarily attributed to the electric fields of the impinging waves created across the gap between the patches. On the other hand, an inductance results primarily from the current path introduced by the presence of the vias [1]. Thus, the surface

impedance of the unit cell can be represented by

$$Z_s = j\frac{\omega L}{1 - \omega^2 LC} \tag{2.2}$$

where the resonant frequency, inductance and capacitance are given by [1]

$$\omega_0 = \frac{1}{\sqrt{LC}} \tag{2.3a}$$

$$L = \mu h \tag{2.3b}$$

$$C = \frac{w\varepsilon_0\,(\varepsilon_r + 1)}{\pi}\cosh^{-1}\!\left(\frac{a}{g}\right) \tag{2.3c}$$

The bandwidth (BW) of AMCs is defined as the frequency range over which the phase of the reflection coefficient is between $+90°$ and $-90°$, and it can be expressed as

$$BW = \frac{\sqrt{L/C}}{\sqrt{\mu_0/\varepsilon_0}} \tag{2.4}$$

The reflection phase of mushroom surfaces can be obtained numerically by modeling a unit cell representing an infinite array of the structure using HFSS. For example, an AMC unit cell comprised of square patches of 12 mm and printed on 5.08 mm thick Rogers RT/Duroid-5880 substrate ($\varepsilon_r = 2.2$) is simulated. Its reflection phase is displayed in Figure 2.4. The resonant frequency of the infinite structure is 5.65 GHz, where the reflection phase is 0.

Vias are used to suppress surface waves within the dielectric substrate. However, the reflection phase response of an AMC that uses mushroom surfaces does not depend on the existence of vias [1]. A similar response to that of Figure 2.4 can be obtained from the same finite design with no vias.
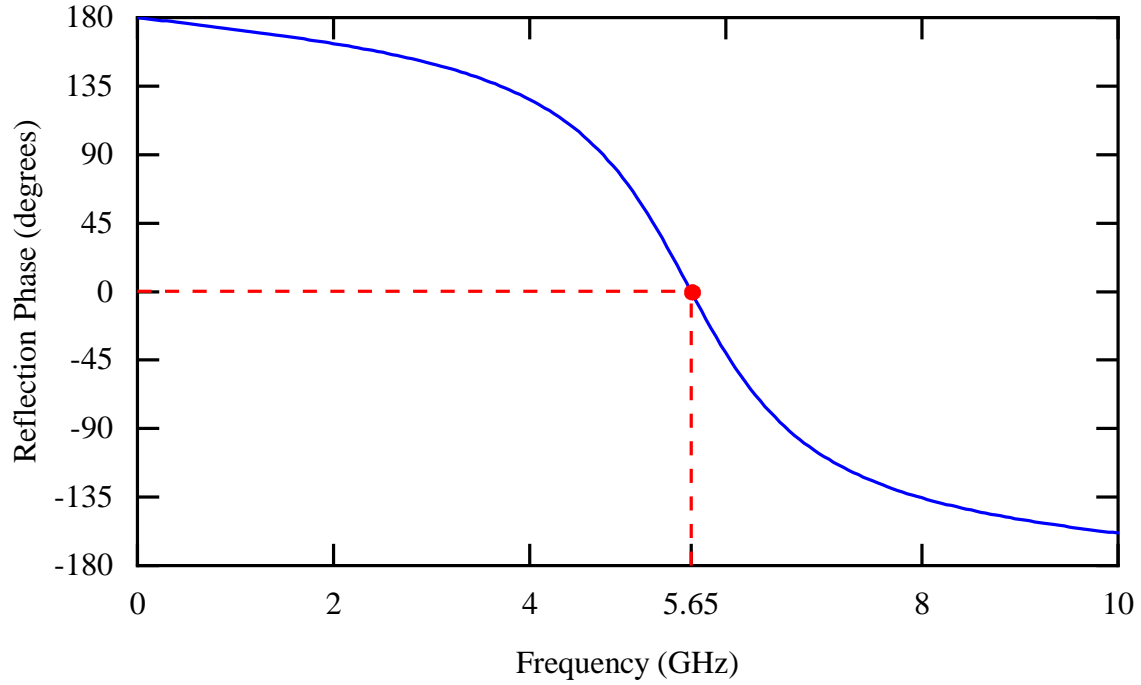
Figure 2.4: Phase of Reflection Coefficient of AMC Mushroom Surface Using Square Patches Simulated Using HFSS.

2.2 Conventional Checkerboard Surfaces

For checkerboard-patterned AMC surfaces similar to the one illustrated in Figure 2.5, the reduction in RCS, compared to that of a PEC ground plane of the same physical size, is represented, approximately by [13]

$$\text{RCS Reduction} = 10 \log_{10} \left| \frac{A_1 e^{jP_1} + A_2 e^{jP_2}}{2} \right|^2 \tag{2.5}$$

where A_1 and A_2 are the amplitudes of the reflection coefficient of AMC 1 and AMC 2, while P_1 and P_2 are the phases of the fields reflected by AMC 1 and AMC 2, respectively.

11
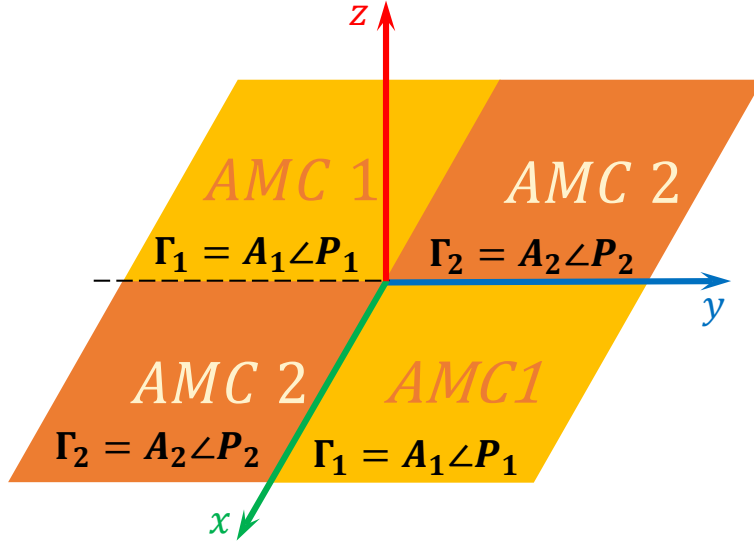
Figure 2.5: A Conventional Checkerboard-Type AMC Structure for RCS Reduction.

Equation (2.5) indicates that at least a 10-dB reduction can be achieved by maintaining a $(180 \pm 37)^{\circ}$ phase difference between AMC 1 and AMC 2 [13]. The RCS reduction versus the phase difference between the two AMCs structures is illustrated in Figure 2.6.
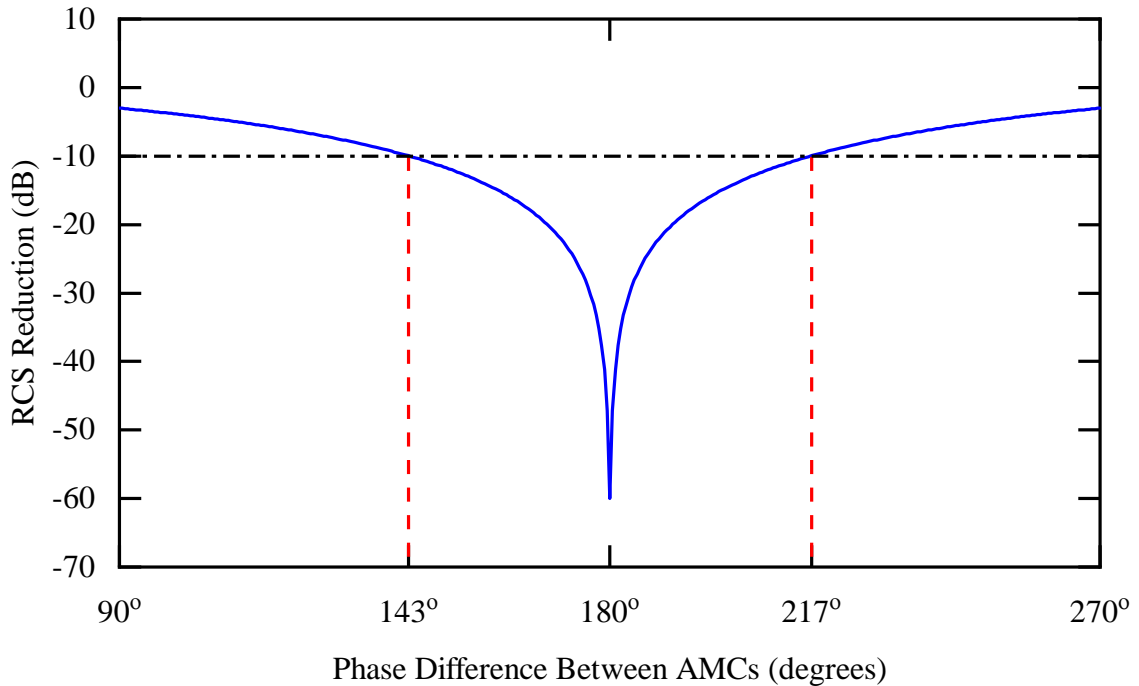
Figure 2.6: RCS Reduction Using (2.5) Versus the Phase Difference Between the two AMC Structures.

2.3   Analysis of AMCs Using an Equivalent Circuit

As illustrated in the previous section, to increase the bandwidth of RCS reduction, two different kinds of AMC surfaces can be selected judiciously to resonate at different frequencies. Accordingly, the 180° phase difference between the two AMC structures can be designed over a wider frequency band.

Broad bandwidths of RCS reductions were achieved in [13, 14] using thick substrates ($h = 6.35$ mm) and the width of the unit cell used was $a = 15$ mm. However, to further decrease the thickness of the substrate while increasing the bandwidth of RCS reduction, the design parameters of each AMC in the checkerboard structure have to be selected judiciously as the bandwidth of 10-dB RCS reduction is directly impacted by such selections.

AMC surfaces of comprised patches, as shown in Figure 2.2, were reviewed in Section 2.1 and they have a single resonance where their reflection phase is zero. The bandwidth of an AMC (reflection coefficient is between $+90°$ and $-90°$) is impacted by the thickness of the substrate h, the outer dimensions of the unit cell a, the patch size w and the dielectric constant of the substrate ε_r.

Utilizing the circuit model of AMCs with square patches, as represented in (2.2)-(2.4), decreasing the dielectric constant of the substrate ε_r is useful to increase the the bandwidth of the designed AMC. Furthermore, Figure 2.7 illustrates the impact of the substrate thickness on the bandwidth of an AMC with $a = 15$ mm, $w = 12$ mm and dielectric constant of the substrate of $\varepsilon_r = 2.2$.

Moreover, Figure 2.8 illustrates the impact of the unit cell's outer dimension a on the bandwidth for a fixed thickness $h = 5.08$ mm, width $w = 3$ mm and dielectric constant of $\varepsilon_r = 2.2$. Although decreasing the outer dimension of the unit cell increases the bandwidth, it also increases the resonant frequency. Thus, the dimensions of the unit cell (h and w) have to be selected judiciously in such a way that a larger bandwidth is achieved with a

thinner substrate without simultaneously increasing the resonant frequency. Utilizing such an approach, it is shown in this chapter that single- and dual-band AMCs can achieve 10-dB RCS-reduction bandwidths of 80% and 97%, respectively.
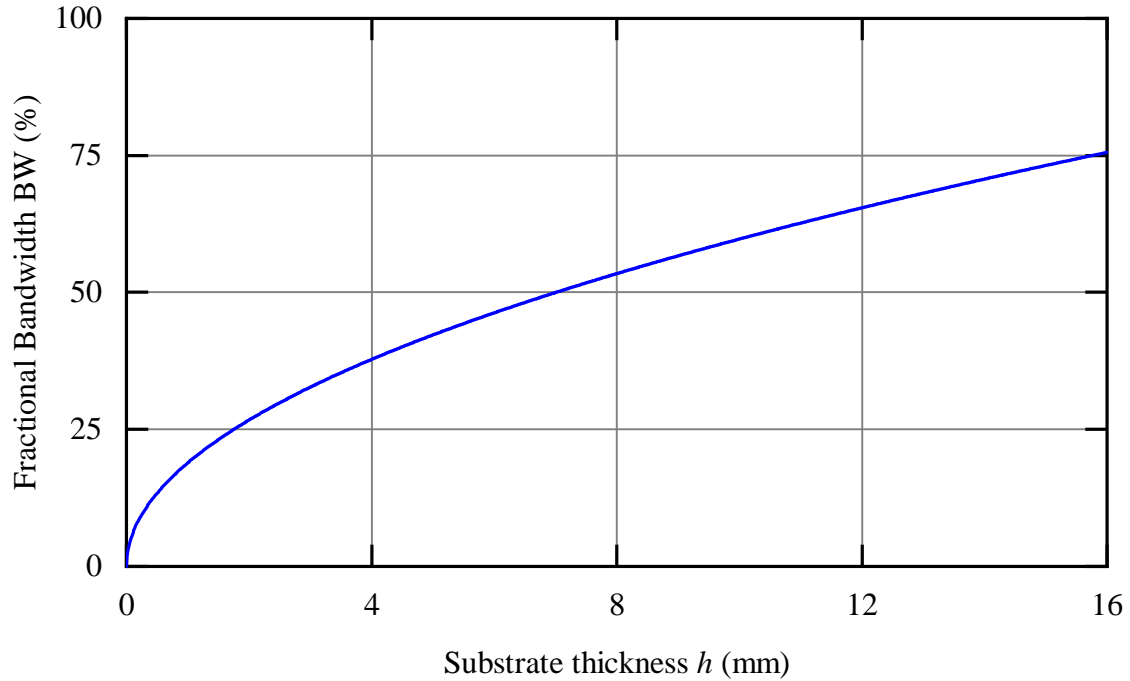
Figure 2.7: Fractional Bandwidth Versus Thickness of a Unit Cell AMC with $a = 15$ mm, $w = 12$ mm and $\varepsilon_r = 2.2$.

2.4 RCS Reduction Using Single-Band AMCs

Based on the analysis described in the previous section, by fixing the outer dimension $a = 10\ mm$ and varying the patch width w, a 10-dB RCS-reduction bandwidth of 80% is achieved. The size of the patch determines the resonant frequency, as illustrated in Figure 2.9. If the patch size is selected judiciously, the RCS-reduction bandwidth can be increased.

Based on the analysis described in the previous section, by fixing the outer dimension $a = 10$ mm and varying the patch width w, a 10-dB RCS-reduction bandwidth of 80% is
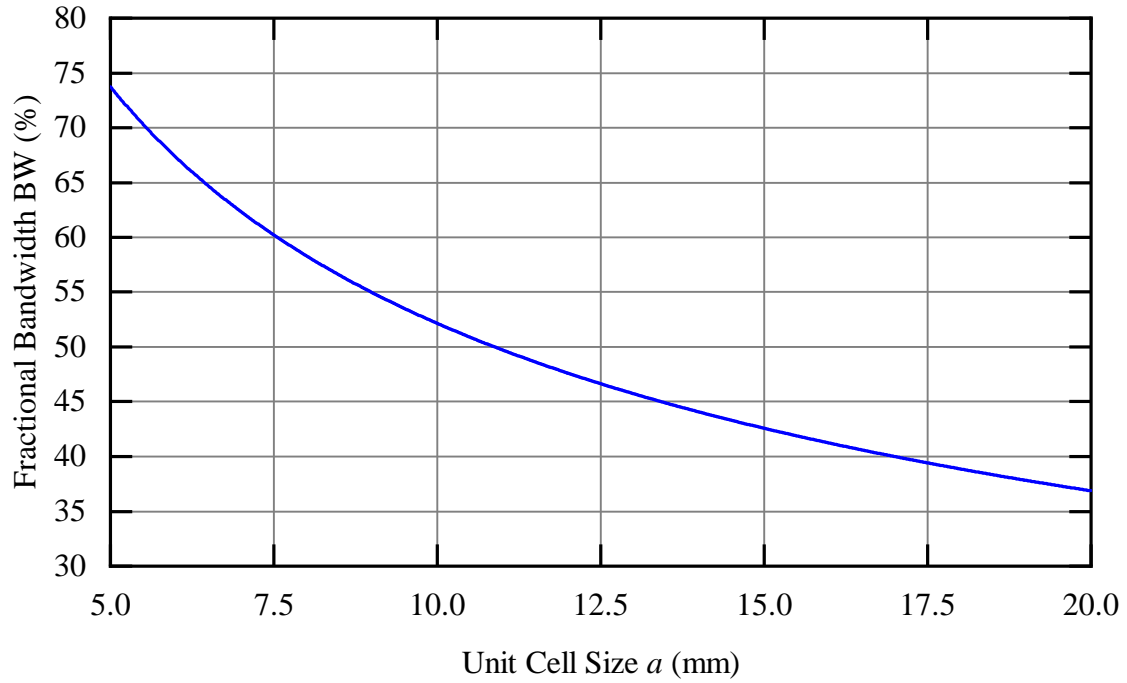
Figure 2.8: Fractional Bandwidth Versus the Size of AMC Unit Cell with $h = 5.08$ mm, $w = 3$ mm and $\varepsilon_r = 2.2$.
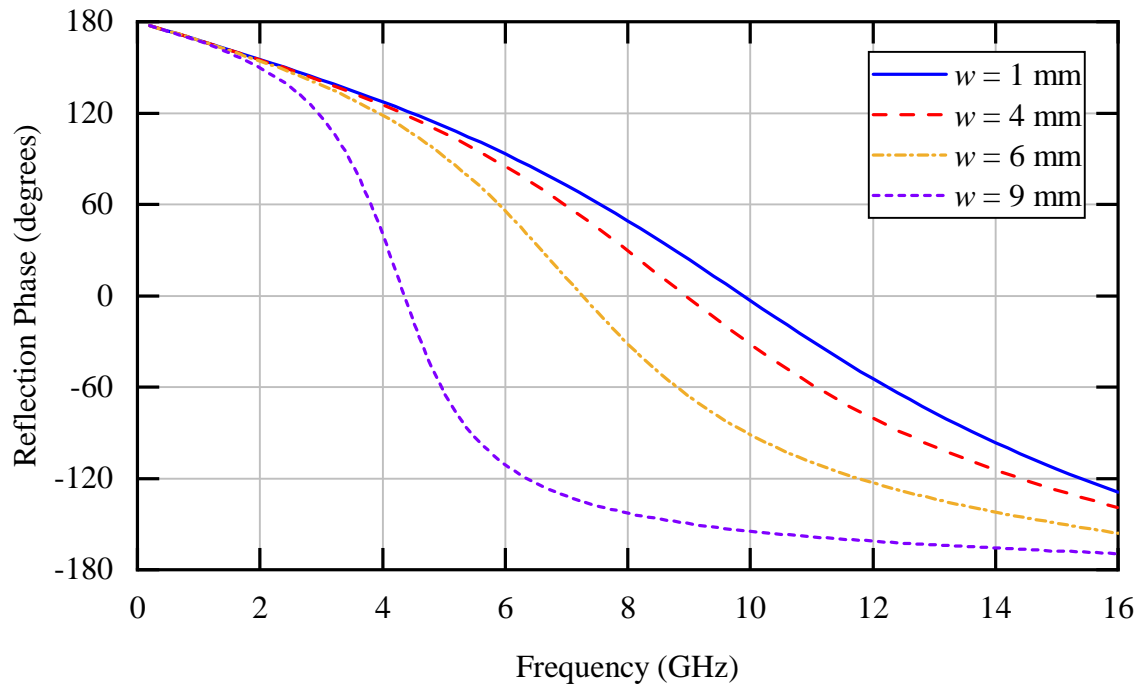
Figure 2.9: Phase of Reflection Coefficients of AMC With Different Patch Sizes.

15

achieved. AMC 1 ($w = 9.3$ mm) and AMC 2 ($w = 3.3$ mm) with both having substrate thickness $h = 5.08$ mm and $\varepsilon_r = 2.2$ resonate at 4 GHz and 9.35 GHz, respectively. The reflection phases along with their phase difference is illustrated in Figure 2.10. AMC 1 and AMC 2 are combined to form a checkerboard-patterned surface which is illustrated in Figure 2.11. The predicted [using (2.5)] and simulated RCS reduction of these AMCs are exhibited in Figure 2.12, a good agreement is found between them with slightly frequency shifted due to the effect of finite size of the AMC surfaces.
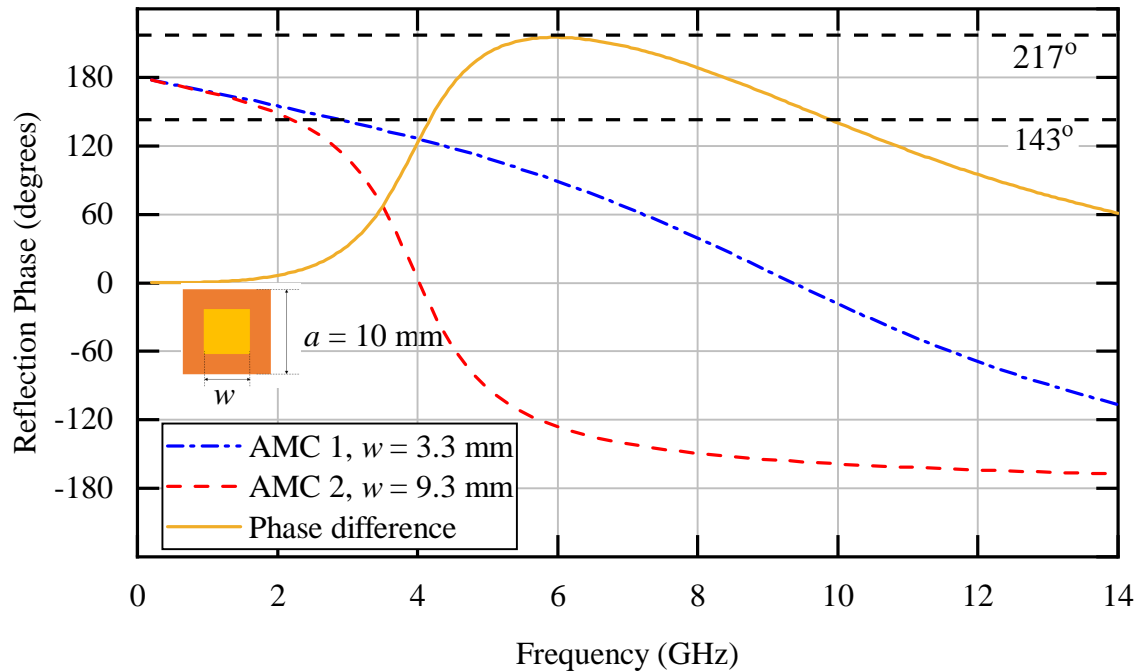
Figure 2.10: Reflection Phases of AMC 1 and AMC 2 Surfaces, and the Phase Difference Between Them.

2.5   RCS Reduction Using Dual-Band AMCs

RCS reduction of 80% bandwidth is achieved using AMC square patches as shown in Section 2.4. The AMC structures were constructed of square patches that resonate at a single frequency. However, to further increase the bandwidth of checkerboard-patterned AMC surfaces, dual resonance AMCs can be used. When a gap is introduced inside the
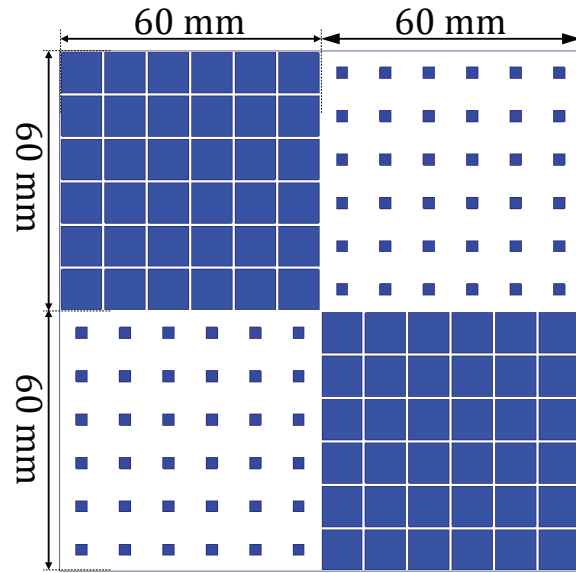
Figure 2.11: A Checkerboard Patterned Structure that Combines AMC 1 and AMC 2 Alternately With Each Comprising 6 × 6 Square Patches.
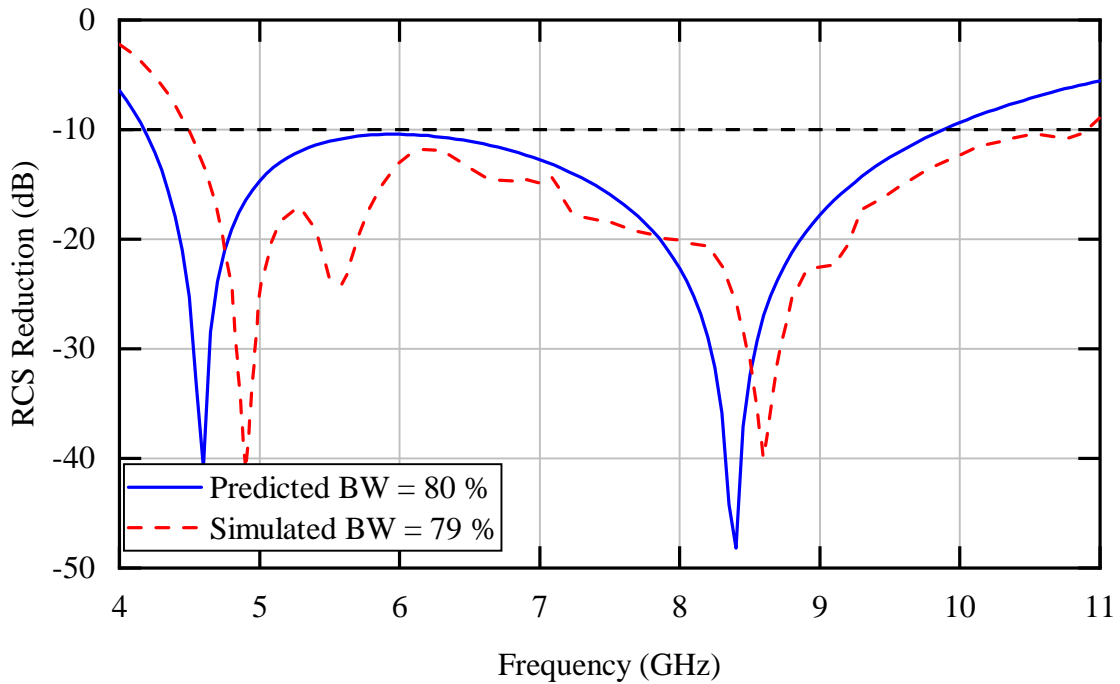
Figure 2.12: Predicted and Simulated RCS Reduction Versus Frequency for the Checkerboard Design Combining AMC 1 and AMC 2.

square-patch AMC shown in Figure 2.13, the AMC exhibits double resonances. The first resonant frequency is attributed to the outer width of the ring patch w_o. This resonance follows the conventional square patch AMC where $w_o = w$. However, the second resonance is controlled by the inner width of the ring patch w_i, and it is independent of the outer dimension w_o.

For a unit cell of size $a = 10.00$ mm, and comprised of a ring patch with the outer width w_o set to 9 mm, the second resonance can then be controlled by the inner width of the ring patch w_i. Figure 2.14 illustrates the influence of w_i on the second resonance.

(a) Top View.   (b) Single Unit Cell.
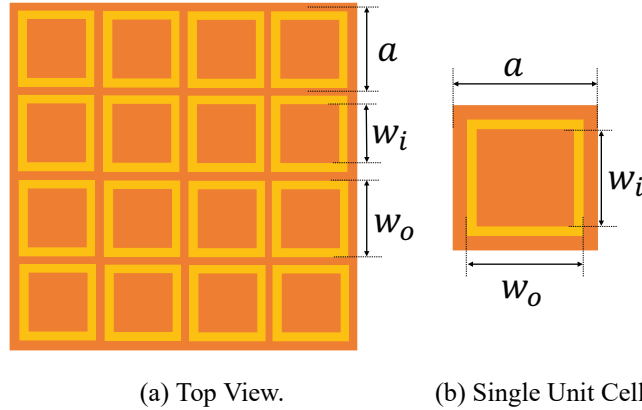
Figure 2.13: Geometry of the AMC Surface Realized as Array of Square Patches.

When the design parameters of a square patch AMC surface (a and w) and a ring-patch AMC surface (a, w_i and w_o) are selected judiciously, a wideband of RCS reduction can be achieved. Following the design parameter discussed earlier, AMC 1 and AMC 2 are selected to have a total of three resonances at 4.65 GHz, 9.15 GHz and 15 GHz. The unit cells of the AMC 1 and AMC 2 structures with both having substrate thickness $h = 5.08$ mm and $\varepsilon_r = 2.2$ are illustrated in Figure 2.15. This selection predicts to achieve an 99% RCS-reduction bandwidth, the reflection phases along with their phase difference is illustrated in Figure 2.16, while the phase difference is maintained within $(180 \pm 37)^\circ$. Then, AMC 1 and AMC 2 are combined to form a checkerboard-patterned surface which is illustrated
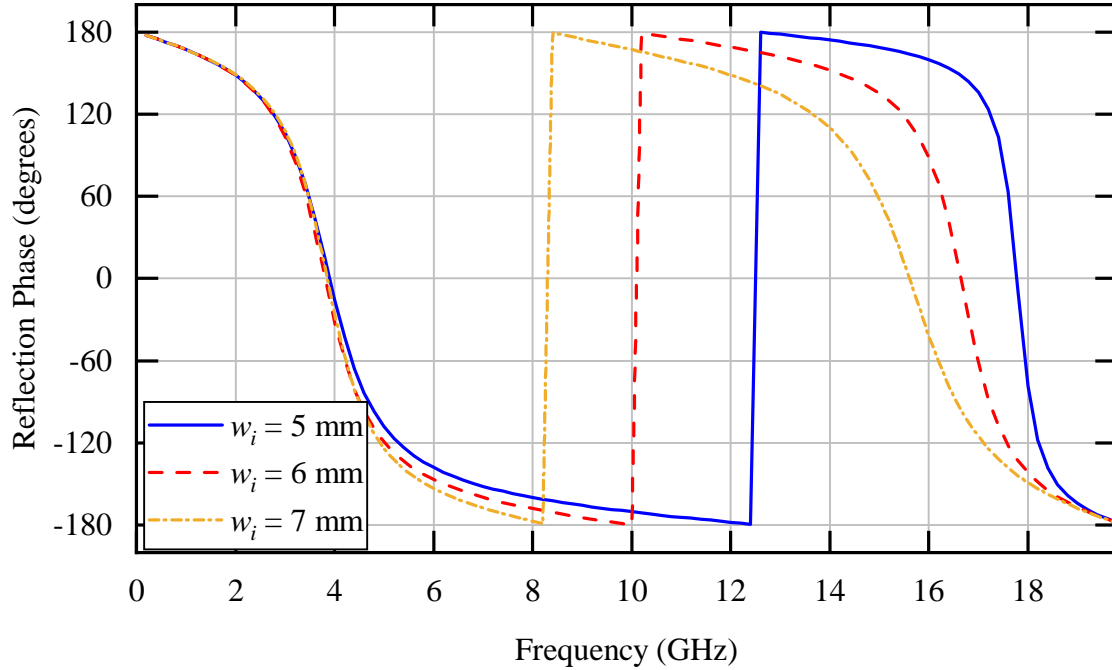
Figure 2.14: Phase of Reflection Coefficients of Different Inner Widths w_i.

in Figure 2.17. The predicted RCS reduction using (2.5) and the simulated data of these AMCs are exhibited in Figure 2.18, and it agrees well with the predicted response. This design achieves a 10-dB RCS-reduction bandwidth of 99% from 4.95 GHz to 14.70 GHz.
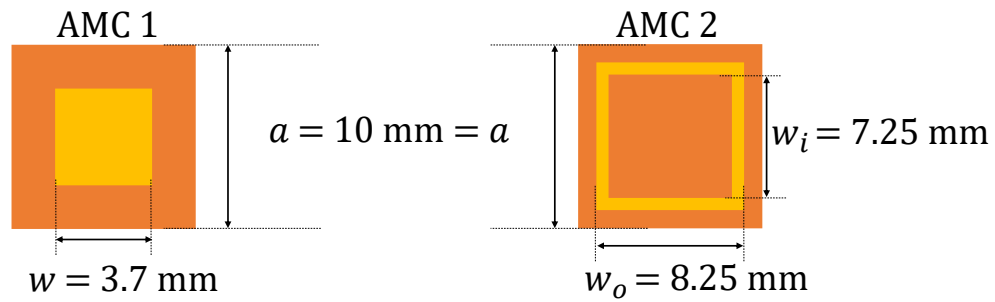
Figure 2.15: Unit Cell of the AMC Structure With a Square Patch (Single Resonance) (AMC 1) and a Ring Patch (Single Resonance) (AMC 2).

The analyses which are shown in this chapter demonstrated that when equation (2.5) and circuit model of AMC are followed judiciously, a broader bandwidth of RCS-reduction can be achieved while reducing the thickness of the substrate. The circuit model aided in
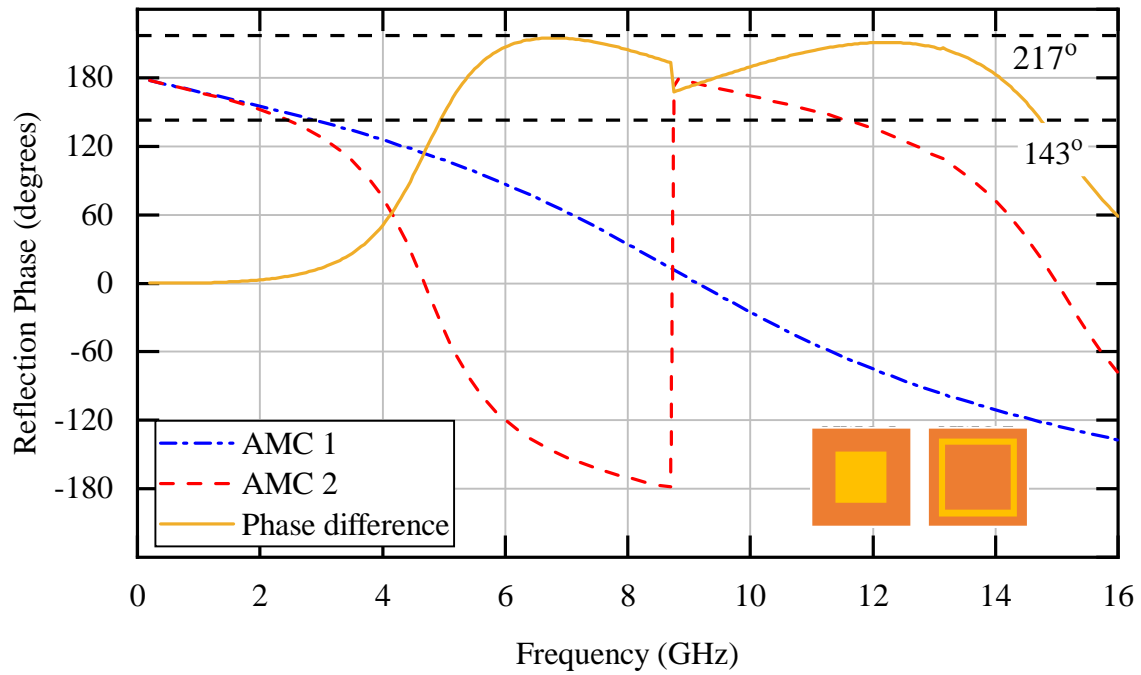
Figure 2.16: Reflection Phases of AMC 1 and AMC 2 Surfaces, and the Phase Difference Between Them.
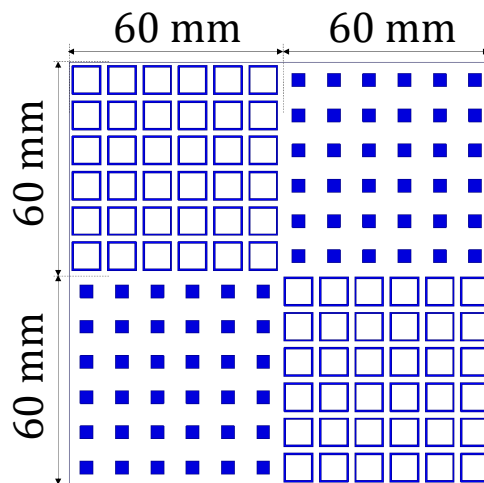
Figure 2.17: A Checkerboard Patterned Structure That Combines AMC 1 and AMC 2 Structures Alternately With Their 6 × 6 Square Patches and 6 × 6 Ring Patches.
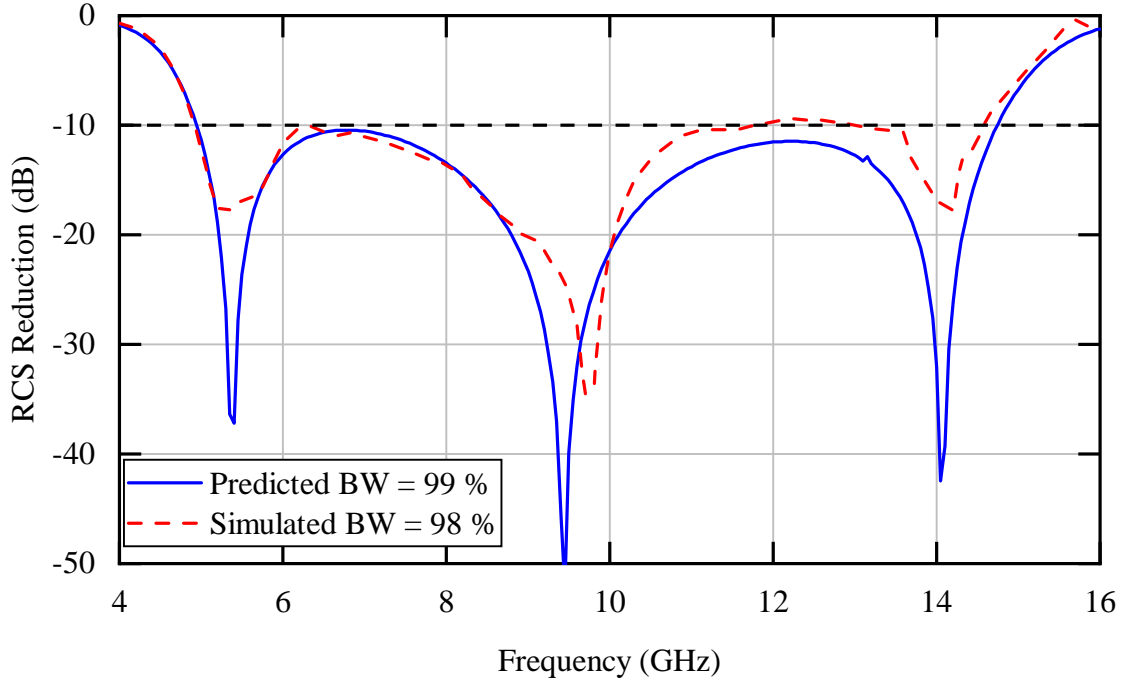
Figure 2.18: Predicted and Simulated Rcs Reduction Versus Frequency for the Checkerboard Design Combining AMC 1 and AMC 2 Structures.

understanding the impact of the unit cell parameters (i.e., outer dimensions, substrate thickness and patch size) on its bandwidth. Thus, a 10-dB RCS-reduction bandwidth of 99% is achieved while the thickness of the substrate is reduced by 20% compared to previous works. In Table 2.1, the RCS-reduction bandwidth performance of the proposed design is compared with other well known wideband checkerboard surfaces. It can be seen that the proposed checkerboard design has the broadest 10-dB RCS-reduction bandwidth.

2.6   Guidelines for Designing Broadband RCS-Reduction AMC

Accordingly, the following design guidelines can be adhered to design ultra-broadband RCS-reduction AMCs:

1. Initially, AMC circuit model should be followed for synthesizing two single-band AMCs and optimizing for the broadband RCS reduction bandwidth (i.e., similar to

Design	Frequency (GHz)	BW (%)	Thickness (mm)	f_h/f_l
Wengang Chen et al. [13] 2015	4.10 - 7.90	63	6.35	1.93
S.H. Esmaeli et al. [15] 2016	9.40 - 23.28	85	2.28	2.48
Anuj Y. Modi et al. [14] 2017	3.75 - 10.00	91	6.35	2.67
Di Sanf et al. [16] 2019	3.78 - 10.08	91	13	2.68
Proposed work (Figure 2.17)	4.95 - 14.70	99	5.08	2.97

Table 2.1: Comparison With Other Wideband RCS Reduction Conventional Checkerboard Designs.

what has been shown in Section 2.4).

2. While designing the conventional checkerboard AMCs, which is constructed by two single-band AMCs, the unit-cell size (a) can be reduced in order to compensate for the reverse impact of reduction by the thickness of the AMCs (h).

3. The RCS-reduction bandwidth can then be expanded further by converting the AMC with lower resonant frequency to dual-band AMC through with the use of the ring patch.

2.7   Summary

In this chapter, checkerboard-patterned AMC structures are presented along with their analytical models. Based on the investigation on the bandwidth of the individual AMC unit cell parameters, a checkerboard design is proposed which exhibits 99% 10-dB RCS-reduction bandwidth.

Chapter 3

PHYSICAL OPTICS MODELING OF SCATTERING BY AMC-BASED CHECKERBOARD SURFACES

In Chapter 2, AMC-based checkerboard surfaces were used to reduce the RCS of a target by redirecting the scattered fields away from the wave incident. The scattering of checkerboard surfaces can be represented analytically using array theory as given by (2.5). However, the RCS-reduction is achieved at the specular direction only and with two AMCs of equal size. Additionally, to understand and provide a physical explanation of the operation principle of checkerboard surfaces, bistatic scattered fields should be observed and analyzed. Such bistatic RCS patterns can be obtained by using full-wave solutions such as the finite element method (FEM). However, FEM generally requires complex computational resources and computational time. Alternatively, conventional array theory can be used to determine the direction of the formed lobes as illustrated [23] and also given by (1.2). However, since array theory assumes that the excitation of each source (i.e., incident wave) is at the center of the scatterer, it becomes inaccurate when the dimensions of the AMCs are small compared to the wavelength of the incident wave. Further, high-frequency asymptotic methods such as Physical Optics (PO) can also be utilized to predict the directions of those lobes through the obtained bistatic RCS patterns. Although edge phenomena (such as diffractions) are not explicitly accounted for, PO can still implicitly account for a part but not total diffraction and thus be utilized with high accuracy along and near specular directions [1, 26, 27]. However, the accuracy of PO deteriorates away from the specular directions and near grazing incidences [1].

In this chapter, PO is used to analyze the scattered fields from checkerboard surface and obtain closed-form bistatic RCS solutions. First, the procedure of obtaining the scattered

fields from conductive objects using PO is detailed based on the potential approach [1].

Then, in order to derive PO-based solutions of scattering by various types of surfaces, PO-based RCS solutions for flat rectangular plates are applied for both TE- and TM-plane wave scattering from:

1. Pure PEC plate [Figure 3.1(a)].

2. Pure PMC plate [Figure 3.1(b)].

3. PEC-PMC hybrid surface [Figure 3.1(c)].

4. AMC1-AMC2 hybrid surface that are constructed using two AMCs of different sizes and reflection coefficients where the axis separating them (z-axis) is perpendicular to the principal plane (xy-plane); z-axis is $\perp$ to the xy-plane [Figure 3.1(d)].

4. AMC1-AMC2 hybrid surface that are constructed using two AMCs of different sizes and reflection coefficients where the axis separating them (x-axis) is parallel to the principal plane (xy-plane); x-axis is $\parallel$ to the xy-plane [Figure 3.1(e)].

6. AMC1-AMC2 hybrid surface that are constructed using two AMCs of different sizes and reflection coefficients and arranged in checkerboard pattern with two separation axes along the x- and z-axis [Figure 3.1(f)].

The models are presented by analytical closed-form expressions, and their response will be compared to full-wave simulations using HFSS and measured data. The advantages and limitations of the applied method to each scatterer will be discussed.

3.1   Physical Optics

Physical optics (PO) techniques are used to analyze the scattering by conducting planar surfaces (PECs) of finite dimensions for TE- and TM-polarized plane waves. These
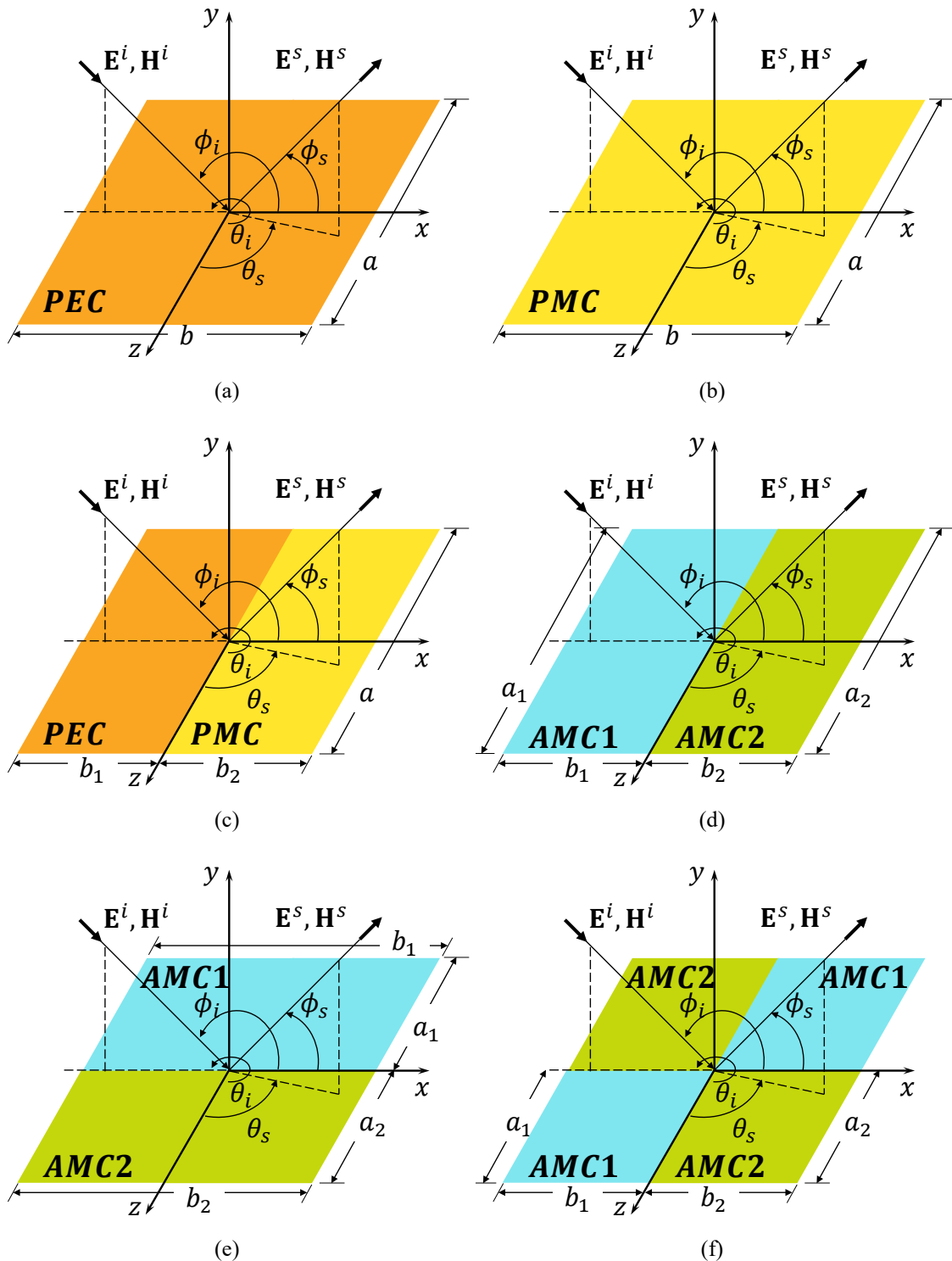
Figure 3.1: Various Scattering Structures and Configurations That Are Going to Be Analyzed in This Chapter. (a) Pure PEC. (b) Pure PMC. (c) PEC-PMC Hybrid Surface. (d) AMC1-AMC2 Hybrid Surface Configuration-1. (e) AMC1-AMC2 Hybrid Surface Configuration-2. (f) AMC1-AMC2 Hybrid Surface That Are Arrange in Checkerboard Pattern.

techniques are basic methods for scattering [1]. When the size of the scatterer is large compared to the wavelength, physical optics techniques are more accurate [26]. The procedure for solving the scattered fields for such a surface is outlined in [1], and it begins with the identification of the incident plane waves and the reflection coefficients of the scattering surface. Then, the source (physical or equivalent) on the scatterer is formulated; the source can be represented as magnetic equivalent current density ($\mathbf{M}$), electric ($\mathbf{J}$), current densities or both. Electric current density can be physical or equivalent; however, the magnetic current density is only an equivalent (non-physical) source [1]. The surface current densities are represented on the surface, and defined based on the boundary conditions, as

$$-\hat{\mathbf{n}} \times (\mathbf{E}_2 - \mathbf{E}_1) = \mathbf{M}_s \tag{3.1a}$$

$$\hat{\mathbf{n}} \times (\mathbf{H}_2 - \mathbf{H}_1) = \mathbf{J}_s \tag{3.1b}$$

From the above defined sources ($\mathbf{J}_s$ and $\mathbf{M}_s$), there are two procedures to solve for the radiated fields. They can be solved directly by integrating Maxwell's equation or wave solutions; however, the integration becomes complicated for complex geometries [1].

The second procedure of solving for the scattered fields requires two steps. First, vector potentials ($\mathbf{A}$ and $\mathbf{F}$) are defined as a function of the current densities $\mathbf{J}_s$, $\mathbf{M}_s$. The second step is then to solve for the radiated electric and magnetic fields from the vector potentials. For surface electric and magnetic current densities, ($\mathbf{J}_s$ and $\mathbf{M}_s$), the $\mathbf{A}$ and $\mathbf{F}$ vector potentials are defined as [1]

$$\mathbf{A} = \frac{\mu}{4\pi} \iint_S \mathbf{J}_s \left(x', y', z' \right) \frac{e^{-j\beta R}}{R} \, ds' \tag{3.2a}$$

$$\mathbf{F} = \frac{\varepsilon}{4\pi} \iint_S \mathbf{M}_s \left(x', y', z' \right) \frac{e^{-j\beta R}}{R} \, ds' \tag{3.2b}$$

Then, the radiated magnetic and electric fields, based on vector potentials $\mathbf{A}$ and $\mathbf{F}$, are

obtained by

$$\mathbf{H_A} = \frac{1}{\mu} \nabla \times \mathbf{A} \tag{3.3a}$$

$$\mathbf{E_F} = -\frac{1}{\varepsilon} \nabla \times \mathbf{F} \tag{3.3b}$$

In the far field ($r > 2D^2/\lambda$ where D is the largest dimension of the scattering surface), (3.2a) and (3.2b) can be approximated by

$$\mathbf{A} \simeq \frac{\mu e^{-j\beta r}}{4\pi r} \mathbf{N} \tag{3.4a}$$

$$\mathbf{F} \simeq \frac{\varepsilon e^{-j\beta r}}{4\pi r} \mathbf{L} \tag{3.4b}$$

where

$$\mathbf{N} = \iint_S \mathbf{J}_s e^{j\beta r' \cos\psi} \, ds' \tag{3.5a}$$

$$\mathbf{L} = \iint_S \mathbf{M}_s e^{j\beta r' \cos\psi} \, ds' \tag{3.5b}$$

A detailed procedure to simplify the solution of the scattered far fields using (3.2a) through (3.4b) is documented in [1]. Thus, the scattered E- and H- field spherical components in the far field to be represented by [1]

$$E_r^s \simeq 0 \tag{3.6a}$$

$$E_\theta^s \simeq -\frac{j\beta e^{-j\beta r}}{4\pi r} (L_\phi + \eta N_\theta) \tag{3.6b}$$

$$E_\phi^s \simeq +\frac{j\beta e^{-j\beta r}}{4\pi r} (L_\theta - \eta N_\phi) \tag{3.6c}$$

$$H_r^s \simeq 0 \tag{3.6d}$$

$$H_\theta^s \simeq +\frac{j\beta e^{-j\beta r}}{4\pi r} \left(N_\phi - \frac{L_\theta}{\eta} \right) \tag{3.6e}$$

$$H_\phi^s \simeq -\frac{j\beta e^{-j\beta r}}{4\pi r} \left(N_\theta + \frac{L_\phi}{\eta} \right) \tag{3.6f}$$

27

where N_θ, N_ϕ, L_θ and L_ϕ are

$$N_\theta = \iint_S \left(J_x \cos \theta_s \cos \phi_s + J_y \cos \theta_s \sin \phi_s - J_z \sin \theta_s\right) e^{+j\beta r' \cos \psi} \, ds' \qquad (3.7a)$$

$$N_\phi = \iint_S \left(-J_x \sin \phi_s + J_y \cos \phi_s\right) e^{+j\beta r' \cos \psi} \, ds' \qquad (3.7b)$$

$$L_\theta = \iint_S \left(M_x \cos \theta_s \cos \phi_s + M_y \cos \theta_s \sin \phi_s - M_z \sin \theta_s\right) e^{+j\beta r' \cos \psi} \, ds' \qquad (3.7c)$$

$$L_\phi = \iint_S \left(-M_x \sin \phi_s + M_y \cos \phi_s\right) e^{+j\beta r' \cos \psi} \, ds' \qquad (3.7d)$$

For a surface placed along the xz-plane, as the case for the scatterers that are shown in Figure 3.1, the differential path can be defined as

$$r' \cos \psi = x' \sin \theta_s \cos \phi_s + z' \cos \theta_s \qquad (3.8)$$

and the differential area is given as

$$ds' = dx' dz' \qquad (3.9)$$

3.2   Incident Plane Wave Polarization and Induced Current Densities

The scattered fields of the aforementioned scattering structures (Figure 3.1) are found in this chapter for both TE^z (parallel) and TM^z (perpendicular) plane waves. Both parallel and perpendicular plane wave polarizations are shown in Figure 3.2, where the incident vector β is on the xy-plane which is defined by $\theta_i = 90°$ and $90° \leqslant \phi_i \leqslant 180°$. Thus, the scattering principal plane (i.e., xy-plane) that contains the maximum scattered field is defined as $\theta_s = 90°$ and $0 \leqslant \phi_s \leqslant 180°$.

Parallel Polarization TE^z Perpendicular Polarization TM^z

(a)   (b)
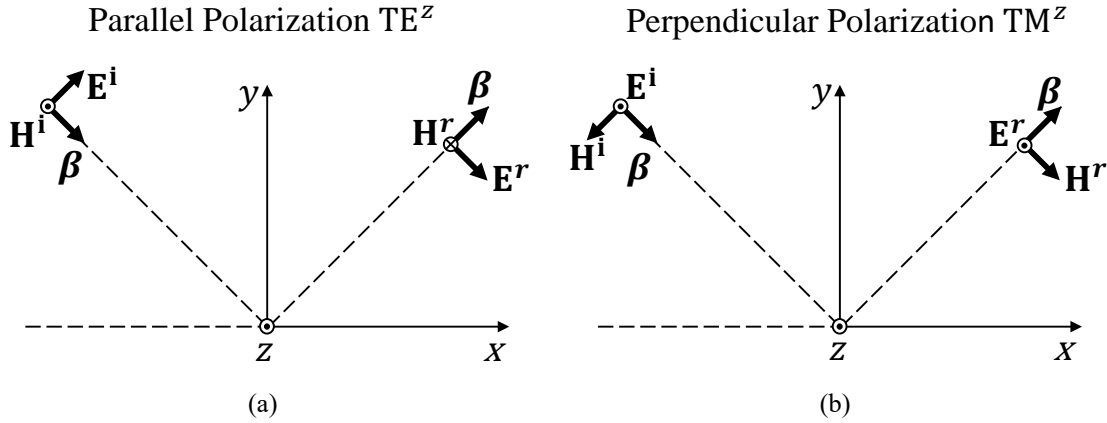
Figure 3.2: Parallel and Perpendicular Uniform Plane Waves.

3.2.1 Parallel Polarization (TE^z)

Based on the geometry of Figure 3.2(a), the parallel-polarized incident fields can be written as

$$\mathbf{E}^i = \eta H_0 \left(\hat{\mathbf{a}}_x \sin \phi_i - \hat{\mathbf{a}}_y \cos \phi_i \right) e^{j\beta(x \cos \phi_i + y \sin \phi_i)} \tag{3.10a}$$

$$\mathbf{H}^i = \hat{\mathbf{a}}_z H_0 e^{j\beta(x \cos \phi_i + y \sin \phi_i)} \tag{3.10b}$$

and for the a planner surface scatterer placed on the xz-plane, the reflected fields can be expressed as

$$\mathbf{E}^r = \eta \Gamma_{\parallel} H_0 \left(\hat{\mathbf{a}}_x \sin \phi_r - \hat{\mathbf{a}}_y \cos \phi_r \right) e^{-j\beta(x \cos \phi_r + y \sin \phi_r)} \tag{3.11a}$$

$$\mathbf{H}^r = -\hat{\mathbf{a}}_z \Gamma_{\parallel} H_0 e^{-j\beta(x \cos \phi_r + y \sin \phi_r)} \tag{3.11b}$$

where ϕ_r is the reflection angle that is computed by applying the boundary conditions along the infinite interface [1]. Additionally, the reflected fields can be expressed in terms of the incident angle ϕ_i where $\phi_r = 180 - \phi_i$ as

$$\mathbf{E}^r = \eta \Gamma_{\parallel} H_0 \left(\hat{\mathbf{a}}_x \sin \phi_i + \hat{\mathbf{a}}_y \cos \phi_i \right) e^{j\beta(x \cos \phi_i - y \sin \phi_i)} \tag{3.12a}$$

$$\mathbf{H}^r = -\hat{\mathbf{a}}_z \Gamma_{\parallel} H_0 e^{j\beta(x \cos \phi_i - y \sin \phi_i)} \tag{3.12b}$$

29

Then, by using the boundary conditions of (3.1a) and (3.1b), the induced equivalent magnetic current density ($\mathbf{M}_s$) of the surface (i.e., $y = 0$) can be found as

$$\mathbf{M}_s = -\hat{\mathbf{n}} \times \mathbf{E}^{total} = -\hat{\mathbf{a}}_y \times \mathbf{E}^i \left(1 + \Gamma_\parallel\right)$$

$$\mathbf{M}_s = \hat{\mathbf{a}}_z \eta H_0 \sin \phi_i e^{j\beta x \cos \phi_i} \left(1 + \Gamma_\parallel\right) \tag{3.13}$$

Thus,

$$M_x = M_y = 0 \text{ and } M_z = \eta H_0 \sin \phi_i e^{j\beta x \cos \phi_i} \left(1 + \Gamma_\parallel\right) \tag{3.14}$$

and the physical electric current density ($\mathbf{J}_s$) can be found as

$$\mathbf{J}_s = \hat{\mathbf{n}} \times \mathbf{H}^{total} = \hat{\mathbf{a}}_y \times \mathbf{H}^i \left(1 - \Gamma_\parallel\right)$$

$$\mathbf{J}_s = \hat{\mathbf{a}}_x H_0 e^{j\beta x \cos \phi_i} \left(1 - \Gamma_\parallel\right) \tag{3.15}$$

and

$$J_y = J_z = 0 \text{ and } J_x = H_0 e^{j\beta x \cos \phi_i} \left(1 - \Gamma_\parallel\right) \tag{3.16}$$

3.2.2   *Perpendicular Polarization (TM^z)*

Similar to the procedure that is used of the parallel-polarized fields, the perpendicularly-polarized incident fields of Figure 3.2(b) can be written as

$$\mathbf{E}^i = \hat{\mathbf{a}}_z E_0 e^{j\beta(x \cos \phi_i + y \sin \phi_i)} \tag{3.17a}$$

$$\mathbf{H}^i = \frac{E_0}{\eta} \left(-\hat{\mathbf{a}}_x \sin \phi_i + \hat{\mathbf{a}}_y \cos \phi_i\right) e^{j\beta(x \cos \phi_i + y \sin \phi_i)} \tag{3.17b}$$

where the reflected fields of an infinite scatterer placed on the xz-plane can be expressed as

$$\mathbf{E}^r = \hat{\mathbf{a}}_z \Gamma_\perp E_0 e^{-j\beta(x \cos \phi_r + y \sin \phi_r)} \tag{3.18a}$$

$$\mathbf{H}^r = \frac{E_0 \Gamma_\perp}{\eta} \left(\hat{\mathbf{a}}_x \sin \phi_r - \hat{\mathbf{a}}_y \cos \phi_r\right) e^{-j\beta(x \cos \phi_r + y \sin \phi_r)} \tag{3.18b}$$

and in terms of the incident angle ϕ_i where $\phi_r = 180 - \phi_i$, the reflected fields can be expressed as

$$\mathbf{E}^r = \hat{\mathbf{a}}_z \Gamma_\perp E_0 e^{j\beta(x\cos\phi_i - y\sin\phi_i)} \tag{3.19a}$$

$$\mathbf{H}^r = \frac{E_0 \Gamma_\perp}{\eta} \left(\hat{\mathbf{a}}_x \sin\phi_i + \hat{\mathbf{a}}_y \cos\phi_i \right) e^{j\beta(x\cos\phi_i - y\sin\phi_i)} \tag{3.19b}$$

Again, by using the boundary conditions of (3.1a) and (3.1b), the induced surface magnetic equivalent current density ($\mathbf{M}_s$) of the surface (i.e., $y = 0$) can be represented by

$$\mathbf{M}_s = -\hat{\mathbf{n}} \times \mathbf{E}^{\text{total}} = -\hat{\mathbf{a}}_y \times \mathbf{E}^i (1 + \Gamma_\perp)$$

$$\mathbf{M}_s = -\hat{\mathbf{a}}_x E_0 e^{j\beta x\cos\phi_i} (1 + \Gamma_\perp) \tag{3.20}$$

Thus,

$$M_y = M_z = 0 \text{ and } M_x = -E_0 e^{j\beta x\cos\phi_i} (1 + \Gamma_\perp) \tag{3.21}$$

and electric current density ($\mathbf{J}_s$) can be represented by

$$\mathbf{J}_s = \hat{\mathbf{n}} \times \mathbf{H}^{\text{total}} = \hat{\mathbf{a}}_y \times \mathbf{H}^i (1 - \Gamma_\perp)$$

$$\mathbf{J}_s = \hat{\mathbf{a}}_z \frac{E_0 \Gamma_\perp}{\eta} \sin\phi_i e^{j\beta x\cos\phi_i} (1 - \Gamma_\perp) \tag{3.22}$$

and

$$J_x = J_y = 0 \text{ and } J_z = \frac{E_0}{\eta} \sin\phi_i e^{j\beta x\cos\phi_i} (1 - \Gamma_\perp) \tag{3.23}$$

3.3 Scattering From PEC

Using physical optics and neglecting edge effects, the RCS of a rectangular finite PEC plate (Figure 3.1a), and represented here as Figure 3.3, for both TE^z - TM^z and polarized incident fields [Figure 3.2], is reported by [1]. Appendix A.1 shows the derivation steps in detail of how to obtain the closed-form bistatic RCS.
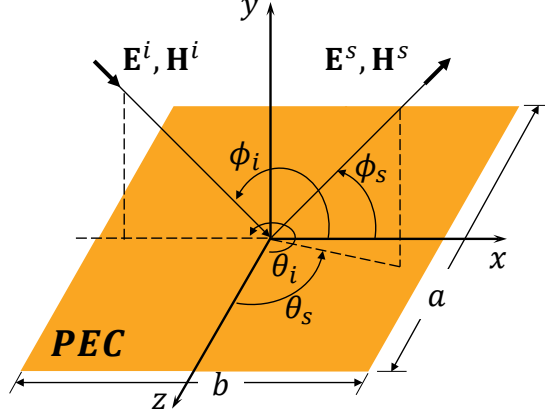
Figure 3.3: Uniform Plane Wave Incident on a Rectangular PEC.

Thus, for TE^z-polarized incident fields [i.e., given by (3.10)], the closed-form bistatic RCS in the principal xy-plane is given by

$$\sigma_{3\text{-D}} \approx 4\pi \left(\frac{ab}{\lambda}\right)^2 \sin^2 \phi_s \left[\frac{\sin(X)}{X}\right]^2 \tag{3.24}$$

while for TM^z-polarized incident fields [i.e., given by (3.17)]

$$\sigma_{3\text{-D}} \approx 4\pi \left(\frac{ab}{\lambda}\right)^2 \sin^2 \phi_i \left[\frac{\sin(X)}{X}\right]^2 \tag{3.25}$$

where

$$X = \frac{\beta b}{2}(\cos\phi_s + \cos\phi_i) \tag{3.26}$$

Plots of (3.24) and (3.25), for $a = b = 4\lambda$, and $\phi_i = 105°$ and 135°, along with PO data obtained from HFSS, are shown and compared to FEM data in Figures 3.4 and 3.5; for both polarizations, the maximums occur along the specular direction when $\theta_s = 90°$ and $\phi_s = 180° - \phi_i$.

Tables 3.1 and 3.2 summarize the RCS values at the specular angles based on (3.24) and (3.25), respectively. The solutions of RCS (PO) are accurate at and near the specular directions ($\phi_s = 180° - \phi_i$) compared to those of HFSS (FEM); the PO solutions become less accurate away from the specular directions. This is a shortcoming of PO where its
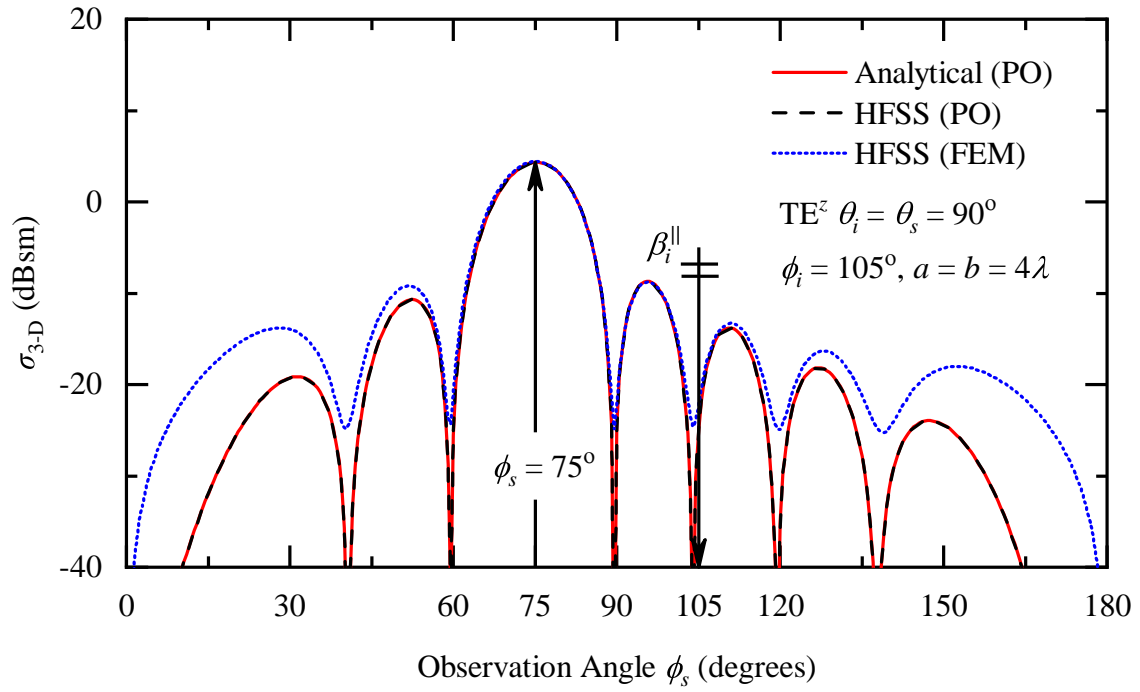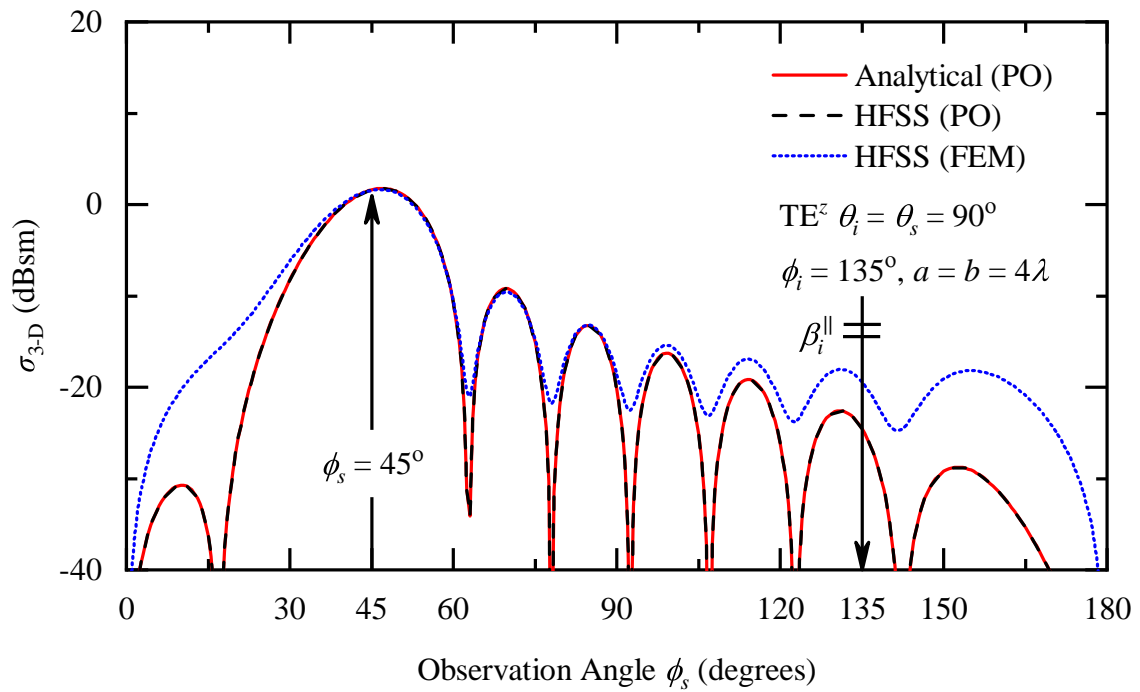
Figure 3.4: Comparison and Validation of Bistatic RCS Patterns Predicted Using PO (Analytical) and PO (HFSS) With Reference to Fem Data With ∥ Polarization $\left(\mathrm{TE}^z\right)$ of a PEC Plate, (a) $a = b = 4\lambda$, $\phi_i = 105°$, and (b) $a = b = 4\lambda$, $\phi_i = 135°$.
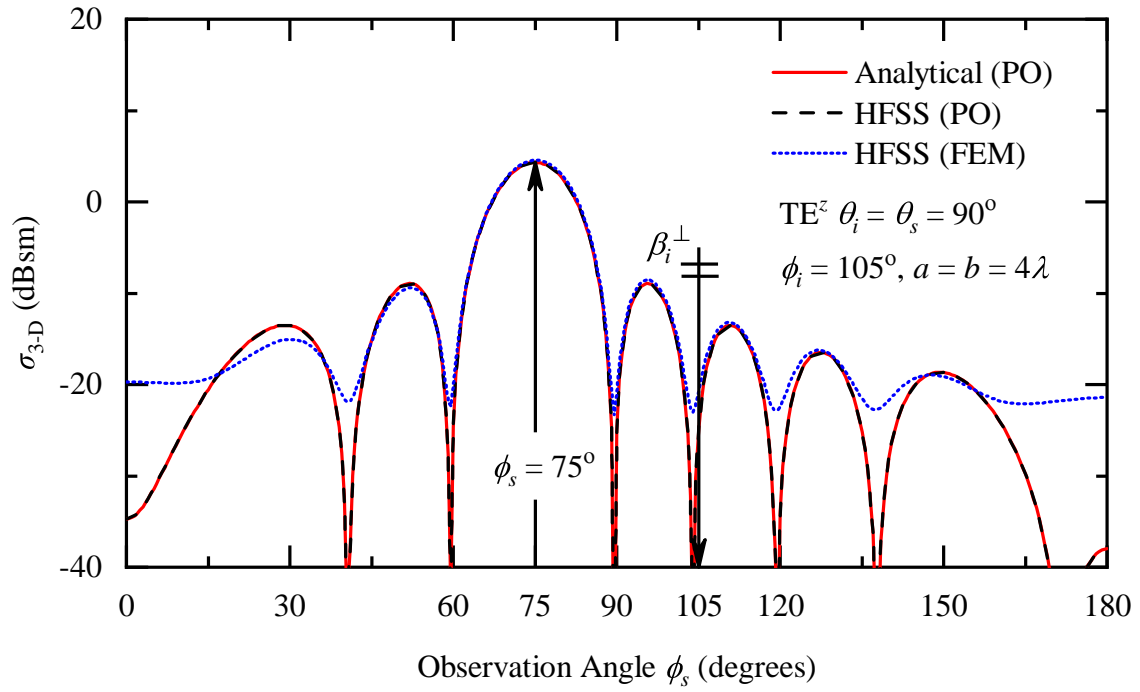
(a)
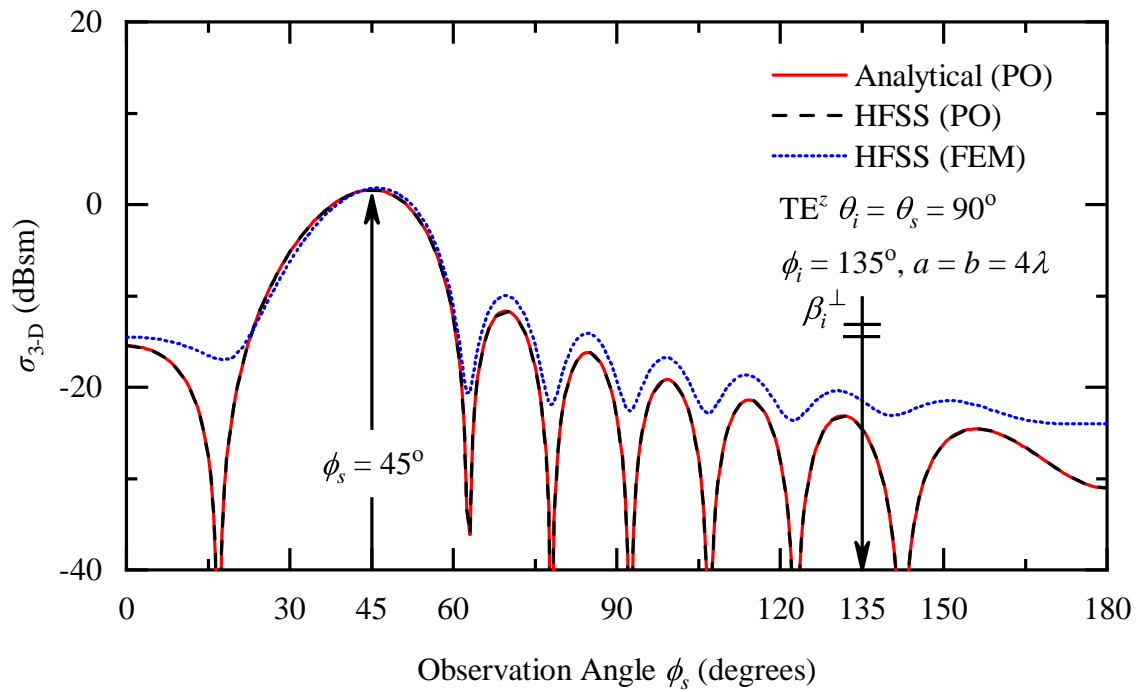
(b)

Figure 3.5: Comparison and Validation of Bistatic RCS Patterns Predicted Using PO (Analytical) and PO (HFSS) With Reference to Fem Data With ⊥ Polarization $\left(TM^z\right)$ of a PEC Plate, (a) $a = b = 4\lambda$, $\phi_i = 105°$, and (b) $a = b = 4\lambda$, $\phi_i = 135°$.

Table 3.1: RCS of the Maximums of Parallel Plane Waves Incident on PEC Plate.

$\sigma_{3\text{-D}}$ (dBsm) TE^z (parallel)			
ϕ_i	Analytical (PO)	HFSS (PO)	HFSS (FEM)
105°	0.80	0.80	1.14
135°	-1.91	-1.91	-1.68

Table 3.2: RCS of the Maximums of Perpendicular Plane Waves Incident on PEC Plate.

$\sigma_{3\text{-D}}$ (dBsm) TM^z (perpendicular)			
ϕ_i	Analytical (PO)	HFSS (PO)	HFSS (FEM)
105°	0.80	0.80	1.15
135°	-1.91	-1.91	-1.42

accuracy diminishes away from the specular direction. Moreover, it can be observed that simulate data obtained using HFSS (PO) agrees very well with the closed-form analytical model; this can be used in the coming sections to verify the correctness of more complicated structures.

3.4   Scattering From PMC

Considering the three-dimensional PMC scatterer shown in Figure 3.1b, and represented here as Figure 3.6, the scattered far-zone fields can be obtained using PO or by applying duality to the existing solutions of PEC. Appendix A.2 shows in detail how the closed form bistatic RCSs are obtained. The presented solutions verify the duality as the TE^z RCS of PEC is identical to the TM^z RCS of PMC and vice versa.

Thus, for TE^z-polarized incident fields [i.e., given by (3.10)], the closed-form bistatic RCS in the principal xy-plane is given by

$$\sigma_{3\text{-D}} \approx 4\pi \left(\frac{ab}{\lambda}\right)^2 \sin^2 \phi_i \left[\frac{\sin(X)}{X}\right]^2 \tag{3.27}$$
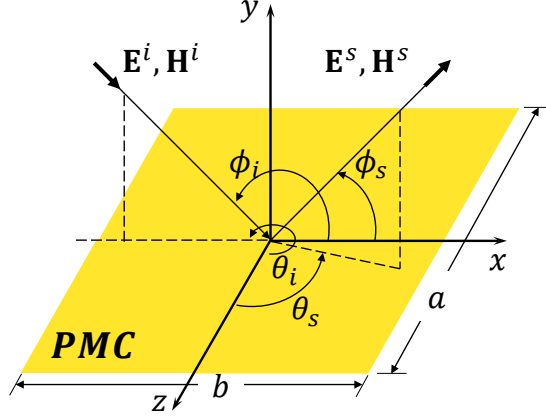
Figure 3.6: Uniform Plane Wave Incident on a Rectangular PMC.

while for TM^z-polarized incident fields [i.e., given by (3.17)]

$$\sigma_{\text{3-D}} \approx 4\pi \left(\frac{ab}{\lambda}\right)^2 \sin^2 \phi_s \left[\frac{\sin(X)}{X}\right]^2 \tag{3.28}$$

where

$$X = \frac{\beta b}{2} (\cos \phi_s + \cos \phi_i) \tag{3.29}$$

Plots of (3.27) and (3.28), for $a = b = 4\lambda$, and $\phi_i = 105°$ and $135°$ along with PO data obtained from HFSS are shown and compared to FEM data in Figures 3.7 and 3.8; for both polarizations, the maximums occur at the specular direction when $\theta_s = 90°$ and $\phi_s = 180° - \phi_i$.

Tables 3.3 and 3.4 summaries the RCS values at specular direction ($\phi_s = 180° - \phi_i$) for the (3.27) and (3.28), respectively.

Table 3.3: RCS of the Maximums of Parallel Plane Waves Incident on PMC Plate.

$\sigma_{\text{3-D}}$ (dBsm) TE^x (parallel)			
ϕ_i	Analytical (PO)	HFSS (PO)	HFSS (FEM)
15°	0.80	0.80	1.42
45°	-1.91	-1.91	-1.95
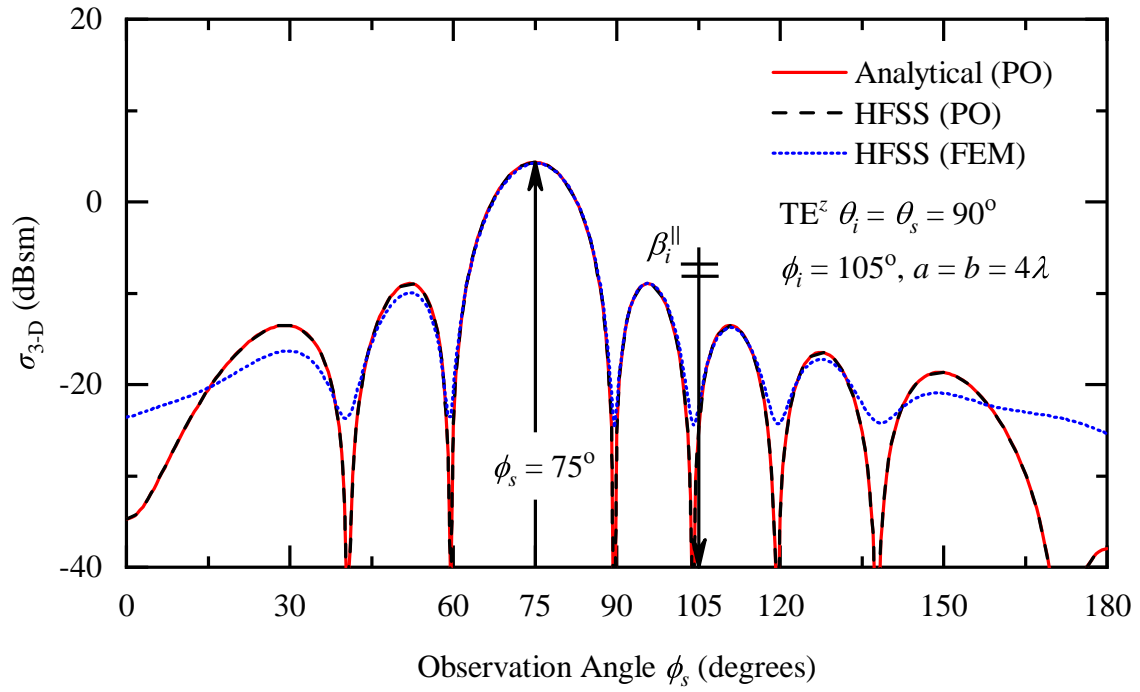
(a)
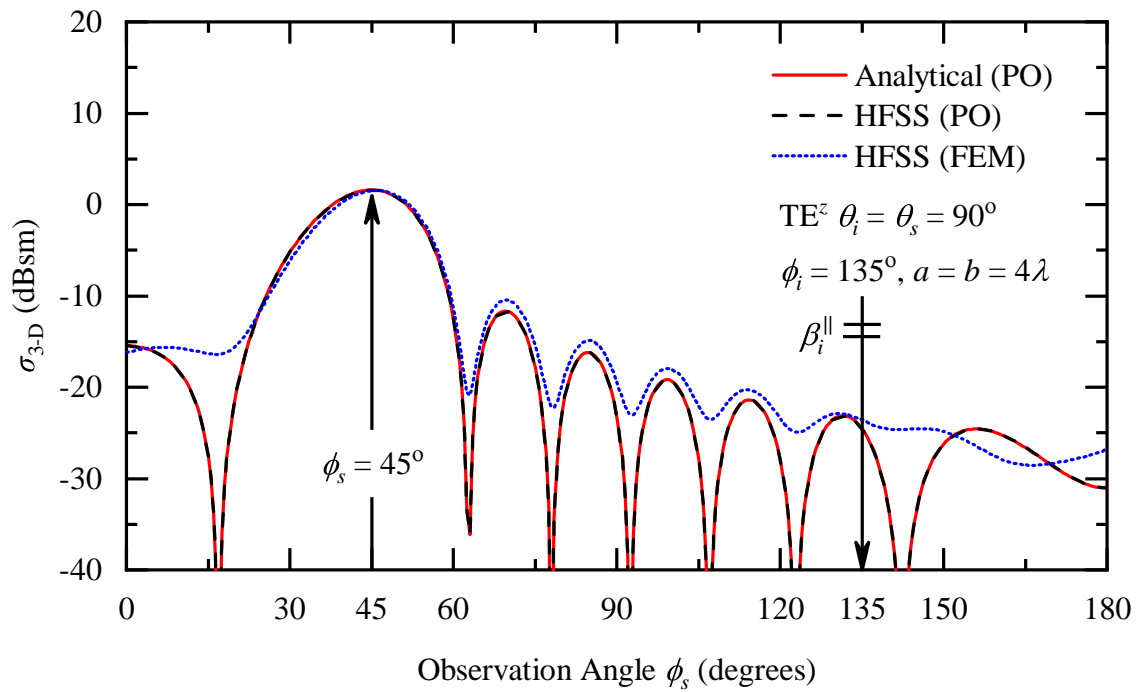
(b)

Figure 3.7: Comparison and Validation of Bistatic RCS Patterns Predicted Using PO (Analytical) and PO (HFSS) With Reference to Fem Data With ∥ Polarization $\left(\mathrm{TE}^z\right)$ of a PMC Plate, (a) $a = b = 4\lambda$, $\phi_i = 105°$, and (b) $a = b = 4\lambda$, $\phi_i = 135°$.

(a)

(b)

Figure 3.8: Comparison and Validation of Bistatic RCS Patterns Predicted Using PO (Analytical) and PO (HFSS) With Reference to Fem Data With $\perp$ Polarization $\left(\text{TM}^z\right)$ of a PMC Plate, (a) $a = b = 4\lambda$, $\phi_i = 105°$, (b) $a = b = 4\lambda$, $\phi_i = 135°$.

Table 3.4: RCS of the Maximums of Perpendicular Plane Waves Incident on PMC Plate.

$\sigma_{3\text{-D}}$ (dBsm) TM^x (perpendicular)			
ϕ_i	Analytical (PO)	HFSS (PO)	HFSS (FEM)
15°	0.80	0.80	1.07
45°	-1.91	-1.91	-2.42

Similar to the PEC case, the solutions of the RCS (PO) are accurate at and near the specular directions ($\phi_s = 180° - \phi_i$) compared to those of HFSS (FEM); the solutions become less accurate away from the specular directions. Moreover, Figure 3.9 compares the scattering from PEC and PMC for both polarizations using FEM for $a = b = 4\lambda$ and $\theta_i = 15°$. The observed difference in the patterns is predicted as the pattern of the PEC is impacted by the the scattered angle and the PMC by incident angle for parallel plane wave, and vice-versa for perpendicular plane wave. The maxima are observed to be the same ($\phi_s = 180° - \phi_i$) for both plates as this can be expected from (3.25) through (3.27) where the maximum of the scattered field from a flat plate always occurs at the specular direction. However, for TE^x with PEC (3.24) and TM^x with PMC (3.28), the maxima of the scattered fields only occur exactly at the specular direction when the plate becomes large compared to the wavelength.
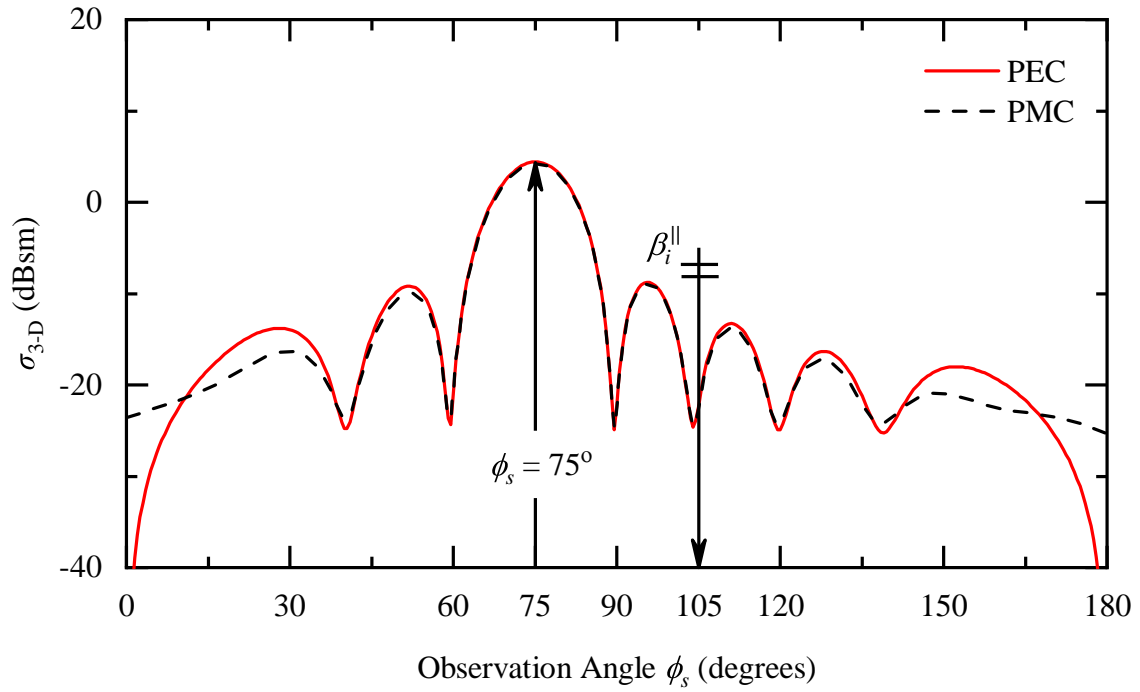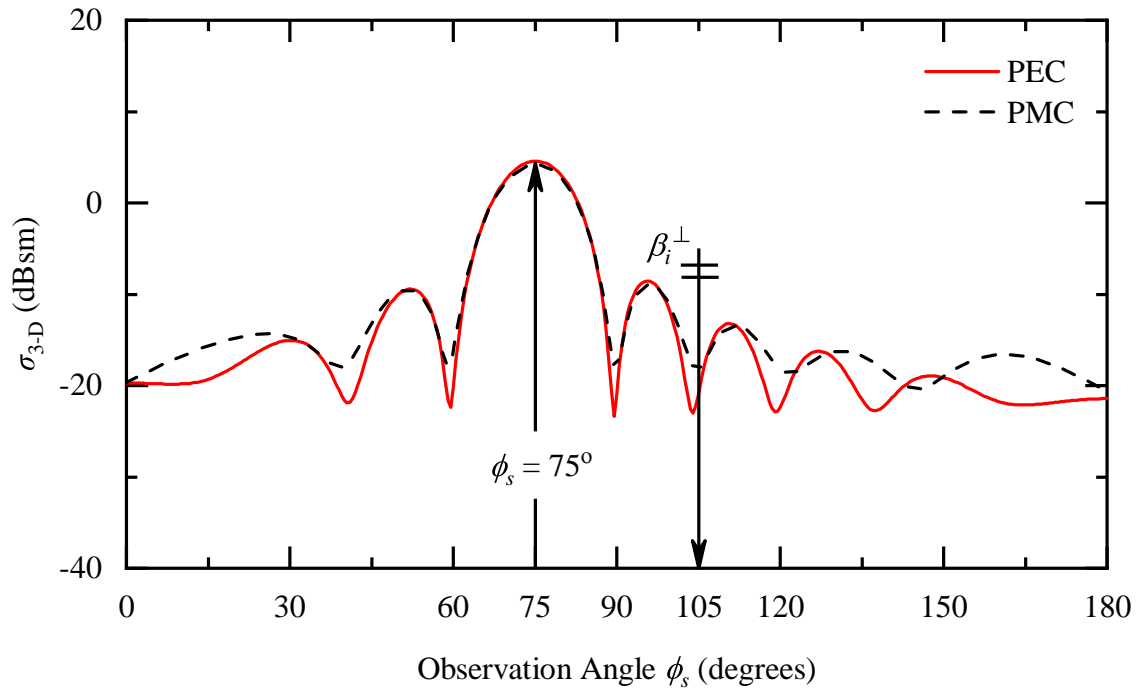
Figure 3.9: Comparison of PEC and PMC Bistatic RCS Patterns Obtained From FEM Data, (a) ∥ Polarization (TE^z), and (b) ⊥ Polarization (TM^z).

40

3.5   Scattering From PEC-PMC Hybrid Surfaces

In the previous two sections, the RCS of pure finite PEC and PMC surfaces was formulated; it was concluded that the PO predicts with high accuracy the RCS at and near the specular directions. Further, the PO closed-form solutions are computationally efficient compared to full-wave FEM simulations. Thus, before applying and generalizing PO for checkerboard-patterned surfaces, it is essential to apply and verify the PO first on rectangular plates consisting of counter phase elements [$0°$ and $180°$ phase elements (i.e., PMC and PEC)]. Thus, combining such arrangement rectangular PEC and PMC, as illustrated in Figure 3.1(c), and represented here as Figure 3.10, forming a "hybrid" plate, physical optics is applied to derive the three-dimensional scattered fields for both parallel and perpendicular polarizations. The solutions are then compared to FEM and PO simulations using HFSS. The closed-form solutions are very accurate, especially, at and near the specular directions.
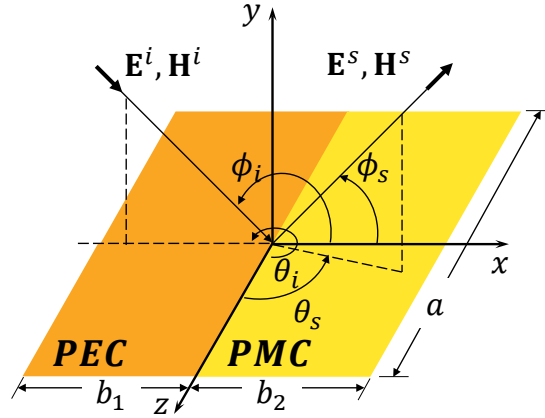
Figure 3.10: Uniform Plane Wave Incident on a PEC-PMC Hybrid Surface.

Detailed steps for the derived analytical expressions are included in Appendix A.3 based on the procedure that is revised in Section 3.1. Therefore, the scattered fields in the principal plan (xy-plane) for a parallel polarization (TE^z) can be written as

$$E_r^s \approx E_\theta^s \approx 0 \qquad\qquad (3.30a)$$

41

$$E_\phi^s \approx \eta H_0 a \frac{j\beta}{2\pi} \left\{ b_1 \sin\phi_s \left[\frac{\sin(2X_1)}{2X_1} - j\sin X_1 \frac{\sin(X_1)}{X_1} \right] \right.$$

$$\left. - b_2 \sin\phi_i \left[\frac{\sin(2X_2)}{2X_2} + j\sin X_2 \frac{\sin(X_2)}{X_2} \right] \right\} \frac{e^{-j\beta r}}{r}$$

(3.30b)

where

$$X_1 = \frac{\beta b_1}{2}(\cos\phi_s + \cos\phi_i) \quad \text{and} \quad X_2 = \frac{\beta b_2}{2}(\cos\phi_s + \cos\phi_i)$$

(3.30c)

Therefor, the RCS can then be written as

$$\sigma_{3\text{-D}} \approx \lim_{r\to\infty} \left[4\pi r^2 \frac{|\mathbf{E}^s|^2}{|\mathbf{E}^i|^2} \right] = \frac{4\pi r^2}{\eta^2 H_0^2} \left| E_\phi^s \right|^2$$

(3.31)

where E_ϕ^s is found from (3.30b).

Analogously, the scattered fields in the principal plan (xy-plane) for a perpendicular polarization (TM^z) can be written as

$$E_r^s \approx E_\phi^s \approx 0$$

(3.32a)

$$E_\theta^s \approx E_0 a \frac{j\beta}{2\pi} \left\{ b_1 \sin\phi_i \left[\frac{\sin(2X_1)}{2X_1} - j\sin X_1 \frac{\sin(X_1)}{X_1} \right] \right.$$

$$\left. - b_2 \sin\phi_s \left[\frac{\sin(2X_2)}{2X_2} + j\sin X_2 \frac{\sin(X_2)}{X_2} \right] \right\} \frac{e^{-j\beta r}}{r}$$

(3.32b)

where X_1 and X_2 can be found from (3.30c). Therefor, RCS can then be written as

$$\sigma_{3\text{-D}} \approx \lim_{r\to\infty} \left[4\pi r^2 \frac{|\mathbf{E}^s|^2}{|\mathbf{E}^i|^2} \right] = \frac{4\pi r^2}{E_0^2} \left| E_\theta^s \right|^2$$

(3.33)

where E_ϕ^s is found from (3.32b).

Plots of (3.31) and (3.33) for $a = b_1 = b_2 = 2.5\lambda$ and $\phi_i = 90°$ and $120°$ are shown in Figures 3.11 and 3.12. The RCS patterns obtained using PO show an excellent agreement with that simulated by the finite element method using HFSS near and around the specular directions. As predicted due the out-of-phase reflected fields of the hybrid plates, a major

42

null occurs at the specular directions of all the illustrated cases. Figure 3.13 shows the FEM solution of TE^x- and TM^x-plane wave obliquely incident on hybrid plates (PEC/PMC).

The location of the two major maximums around the null at specular directions is controlled by the size of the plates (b_1 and b_2) along the y-directions. Additionally, the levels of those maximum is attributed to the over all sizes of the plates (a, b_1 and b_2). Figure 3.14 illustrates the impact of the b_1 and b_2 of the beamwidth and the location of the two major maximums. It is observed that as the size increases along the y directions, the major lobes approach the specular location and their beamwidth becomes narrower.
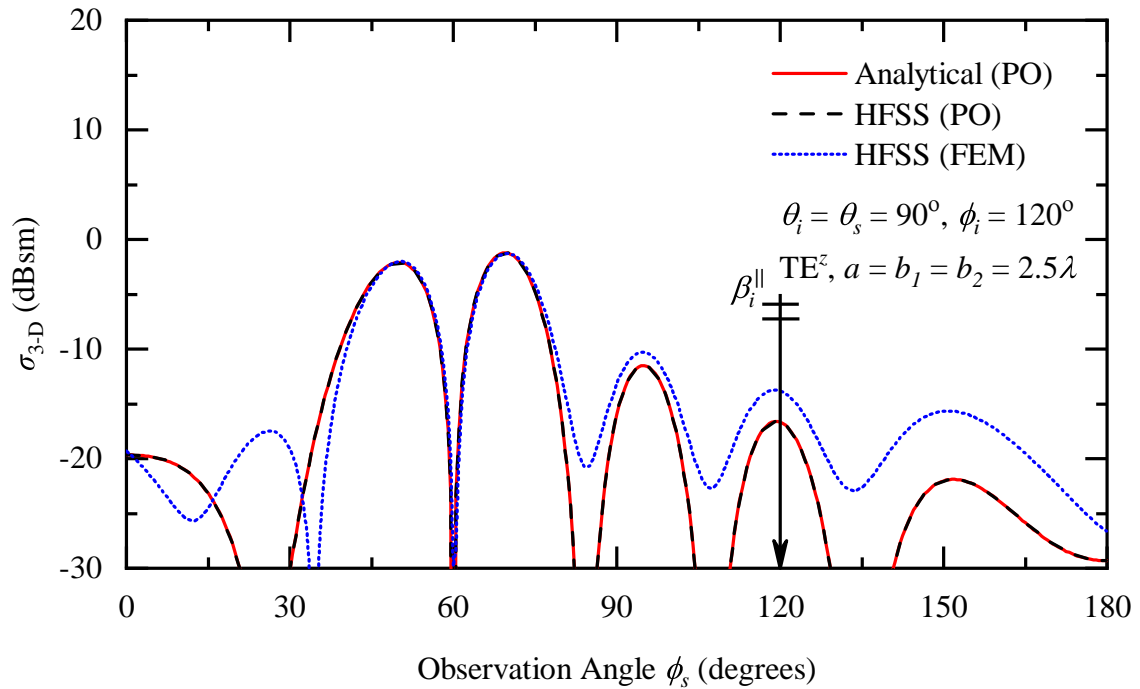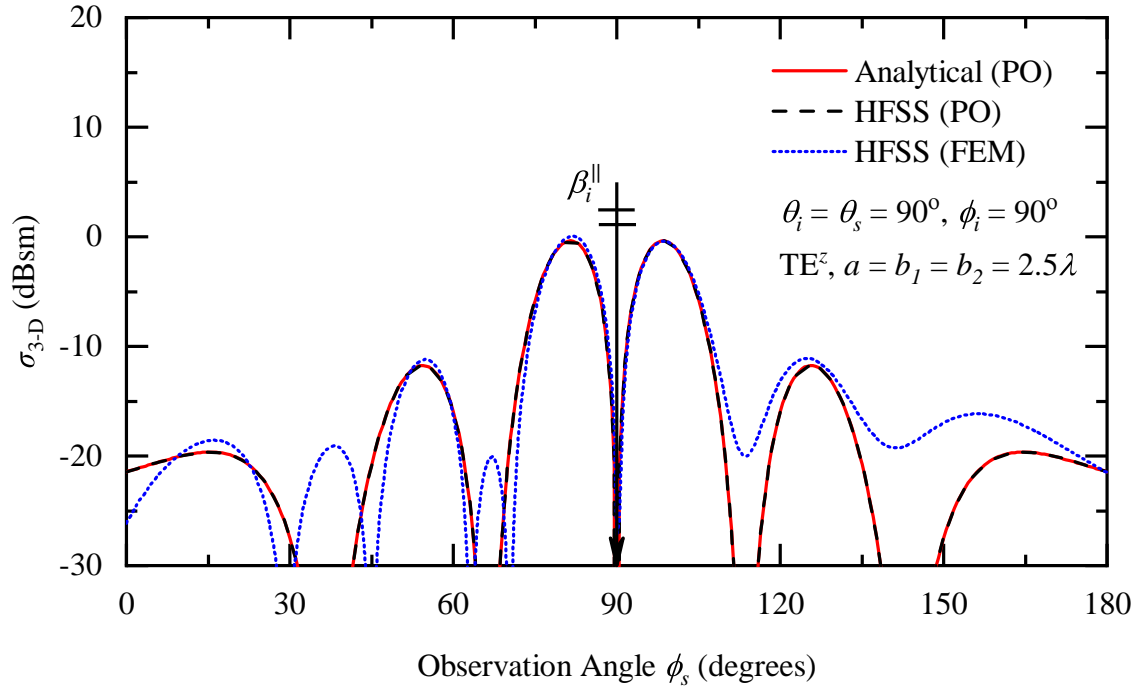
Figure 3.11: Comparison and Validation of Bistatic RCS Patterns Predicted Using PO (Analytical) and PO (HFSS) With Reference to FEM Data With ∥ Polarization $\left(\text{TE}^z\right)$ of PEC-PMC Hybrid Surfaces, (a) $a = b_1 = b_2 = 2.5\lambda$, $\phi_i = 90°$, and (b) $a = b_1 = b_2 = 2.5\lambda$, $\phi_i = 120°$.
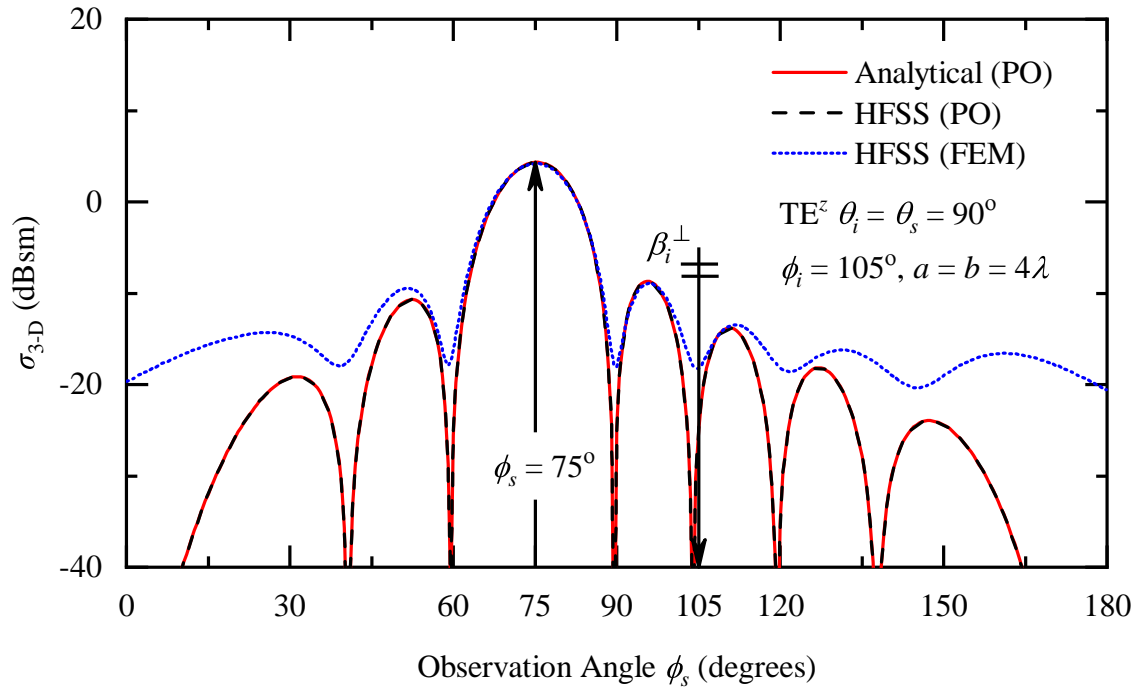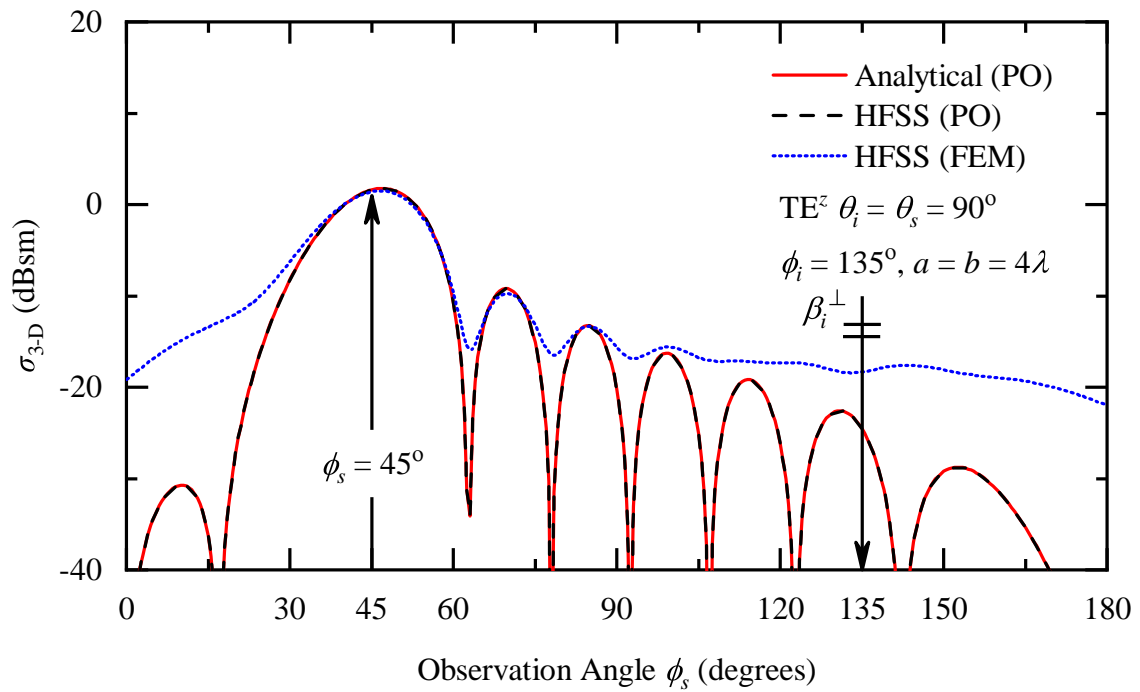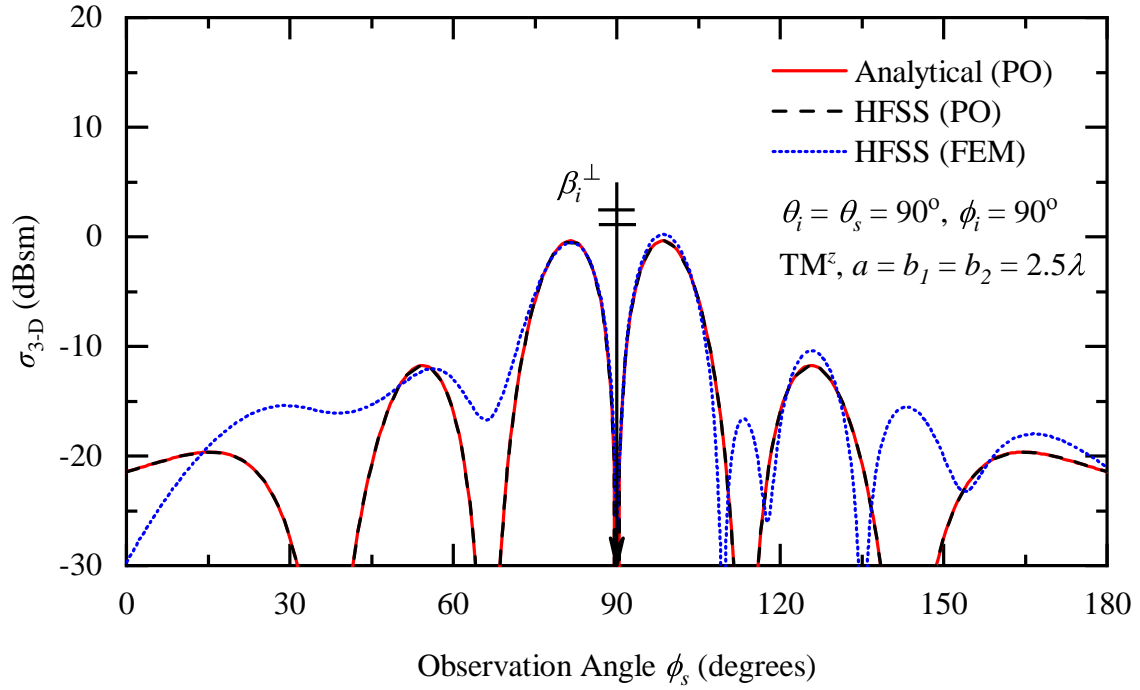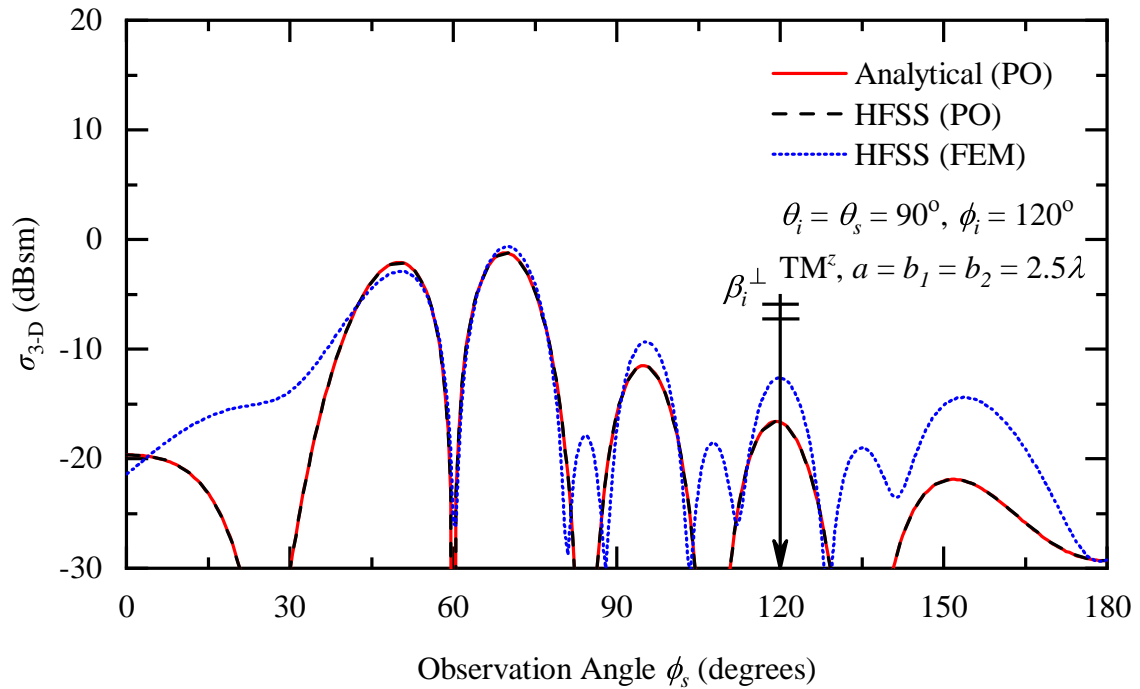
Figure 3.12: Comparison and Validation of Bistatic RCS Patterns Predicted Using PO (Analytical) and PO (HFSS) With Reference to FEM Data With $\perp$ Polarization $\left(\text{TM}^z\right)$ of PEC-PMC Hybrid Surfaces, (a) $a = b_1 = b_2 = 2.5\lambda$, $\phi_i = 90°$, and (b) $a = b_1 = b_2 = 2.5\lambda$, $\phi_i = 120°$.

(a)

(b)
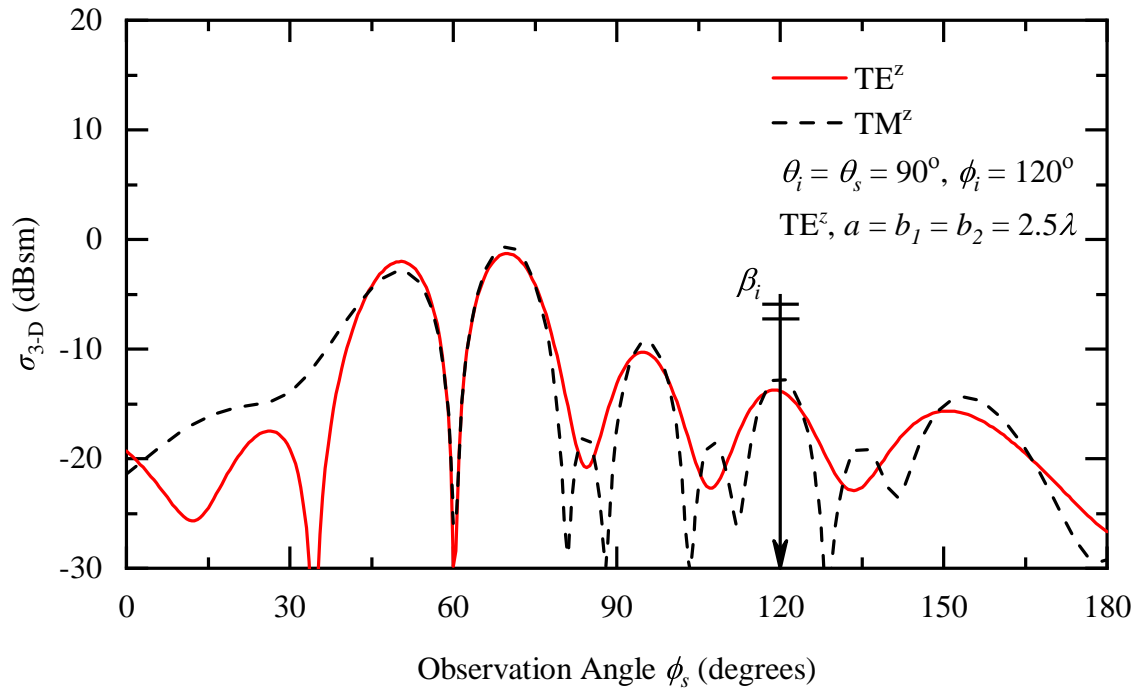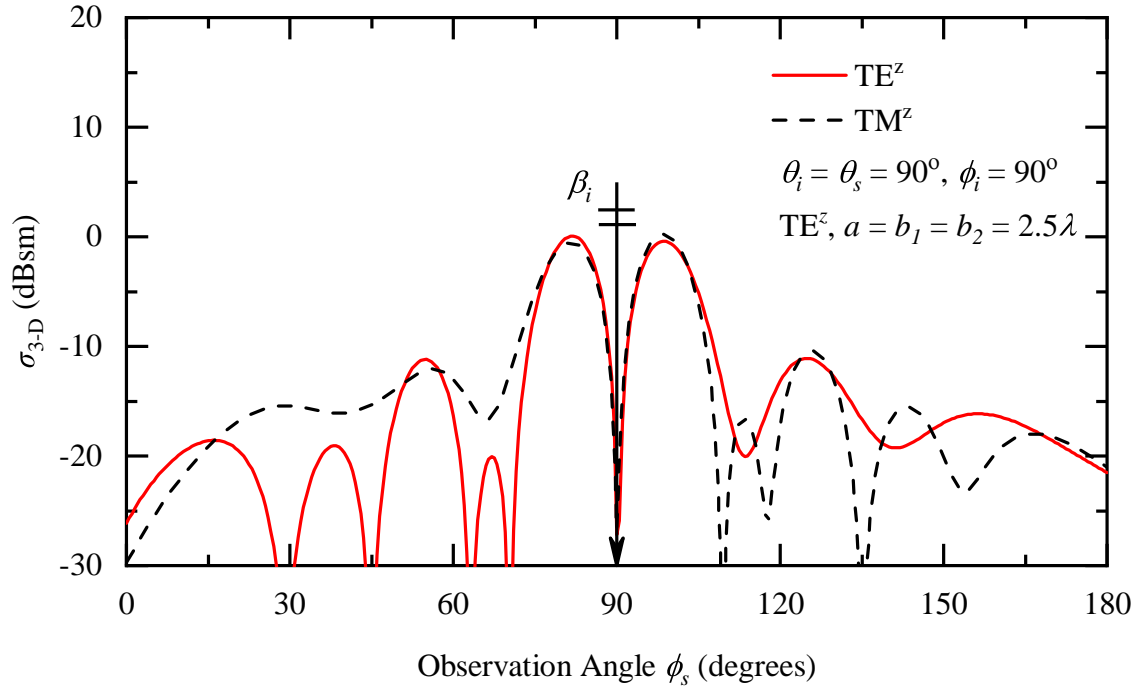
Figure 3.13: FEM Solution of (a)TE^z-, and (b)TM^z-Plane Wave Obliquely Incident on PEC-PMC Hybrid Surfaces
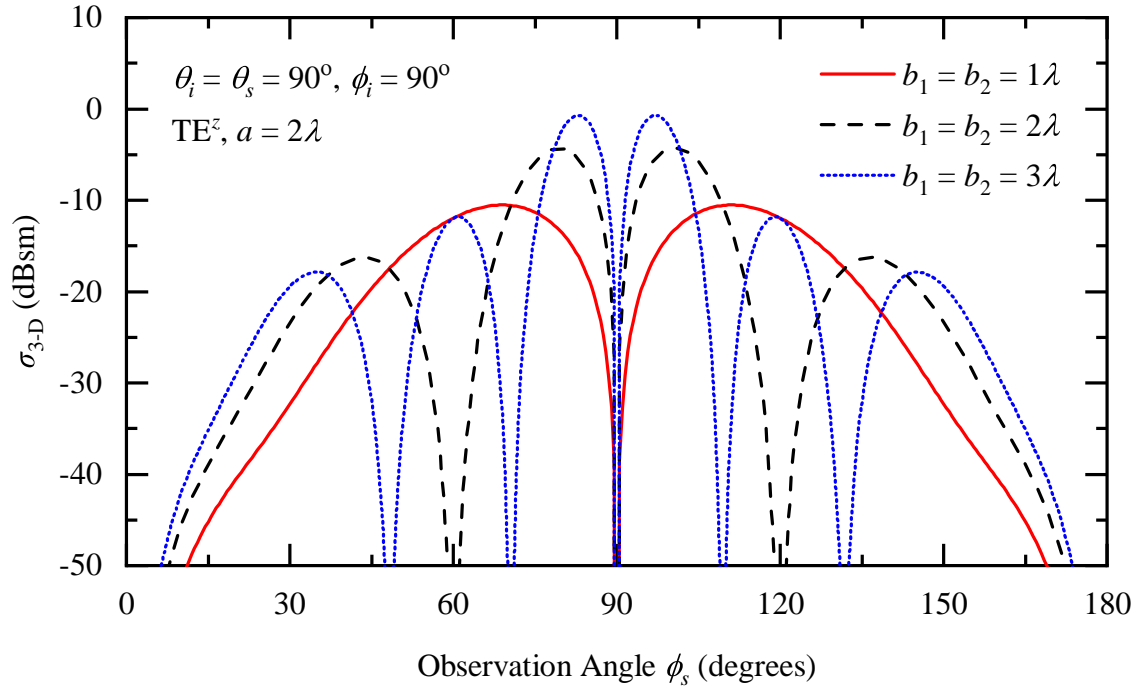
(a)
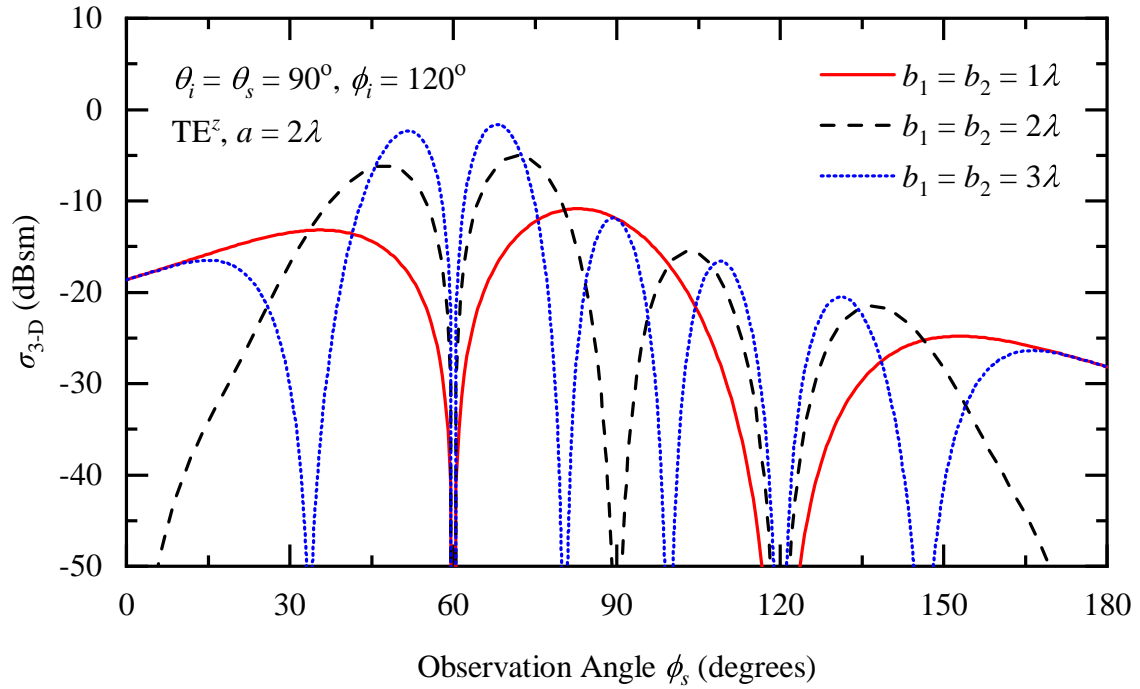
(b)

Figure 3.14: TE^z-Plane Wave Obliquely Incident on Hybrid Plates (PEC/PMC) With Varying Lengths Along the y Direction With (a) $\phi_i = 90°$, and (b) $\phi_i = 120°$.

47

3.6 Scattering From AMC1-AMC2 Hybrid Surfaces

Physical optics shows promising results for the analysis presented in the previous section, especially at and near the specular directions for PEC-PMC hybrid surfaces. In this section, a generalized closed-form solutions from PEC-PMC hybrid surfaces to AMC1-AMC2 hybrid surfaces are derived when the reflection phase is fixed to be 0° or 180° for three different configurations. The structures of interest are illustrated in Figure 3.1(d)-(f), and represented here as Figures 3.15(a)-(c). This allows for further analysis of the RCS in terms of reflection coefficients (Γ), physical dimensions of each plate (a and b), incident (ϕ_i) and scattered (ϕ_s) angles.

The total scattered fields from all the configurations that are presented in this section are found by adding the scattered fields from each surface, through superposition, as

$$\mathbf{E}^s_{\text{total}} = \mathbf{E}^s_{\text{AMC1}} + \mathbf{E}^s_{\text{AMC2}} \tag{3.34}$$

3.6.1 Configuration-1

The closed-form bistatic RCS in the principal xy-plane by the AMC1-AMC2 hybrid surfaces (Configuration-1) that is represented by Figure 3.15(a) for TE^z-polarized incident fields [i.e., given by (3.10)] is derived in Appendix A.4 and can be written as

$$\sigma_{\text{3-D}} \approx \lim_{r \to \infty} \left[4\pi r^2 \frac{|\mathbf{E}^s|^2}{|\mathbf{E}^i|^2} \right] = \frac{4\pi r^2}{\eta^2 H_0^2} \left| E^s_{\text{AMC1}} + E^s_{\text{AMC2}} \right|^2 \tag{3.35}$$

Since (in the principal xy-plane)

$$E^s_{r_{\text{AMC1}}} \approx E^s_{\theta_{\text{AMC1}}} \approx E^s_{r_{\text{AMC2}}} \approx E^s_{\theta_{\text{AMC2}}} \approx 0 \tag{3.36}$$

both E^s_{AMC1} and E^s_{AMC2} reduce to

$$E^s_{\text{AMC1}} = E^s_{\phi_{\text{AMC1}}} \tag{3.37a}$$

48
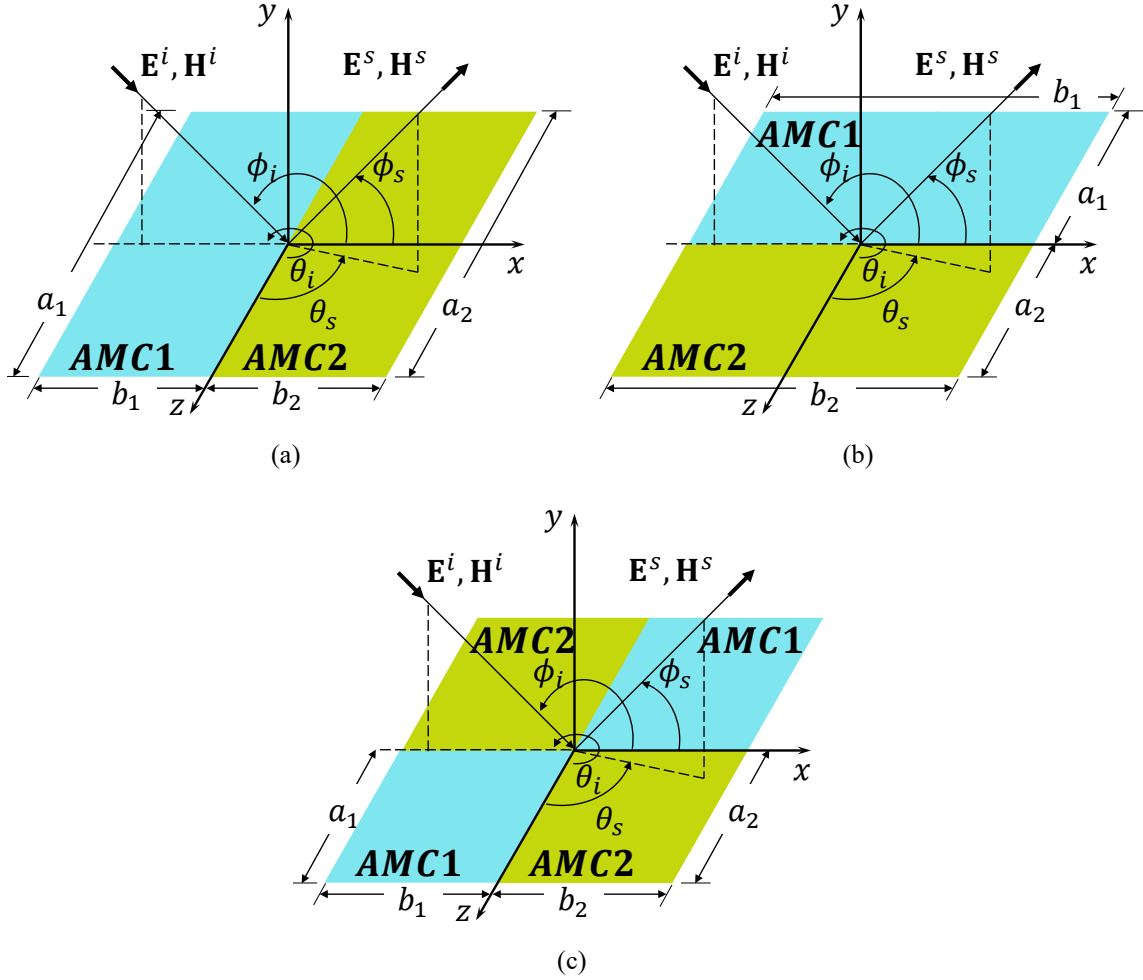
Figure 3.15: AMC1-AMC2 Hybrid Surfaces Scattering Structures. (a) Configuration-1. (b) Configuration-2. (c) Configuration-3.

$$E^s_{\text{AMC2}} = E^s_{\phi_{\text{AMC2}}} \tag{3.37b}$$

Then, $E^s_{\phi_{\text{AMC1}}}$ and $E^s_{\phi_{\text{AMC2}}}$ can be written as

$$E^s_{\phi_{\text{AMC1}}} \approx C_1 \left[\frac{\sin(2X_1)}{2X_1} - j\sin X_1 \frac{\sin(X_1)}{X_1} \right] \left[\sin\phi_s \left(1 - |\Gamma_{\text{AMC1}}|e^{j\angle\Gamma_{\text{AMC1}}} \right) \right.$$
$$\left. - \sin\phi_i \left(1 + |\Gamma_{\text{AMC1}}|e^{j\angle\Gamma_{\text{AMC1}}} \right) \right] \frac{e^{-j\beta r}}{r} \tag{3.38a}$$

where

$$C_1 = a_1 b_1 \eta H_0 \frac{j\beta}{4\pi} \tag{3.38b}$$

49

$$X_1 = \frac{\beta b_1}{2} \left(\cos \phi_s + \cos \phi_i \right) \tag{3.38c}$$

and

$$E^s_{\phi_{AMC2}} \approx C_2 \left[\frac{\sin (2X_2)}{2X_2} + j \sin X_2 \frac{\sin (X_2)}{X_2} \right] \left[\sin \phi_s \left(1 - |\Gamma_{AMC2}| e^{j \angle \Gamma_{AMC2}} \right) \right.$$
$$\left. - \sin \phi_i \left(1 + |\Gamma_{AMC1}| e^{j \angle \Gamma_{AMC1}} \right) \right] \frac{e^{-j\beta r}}{r} \tag{3.39a}$$

where

$$C_2 = a_2 b_2 \eta H_0 \frac{j\beta}{4\pi} \tag{3.39b}$$

$$X_2 = \frac{\beta b_2}{2} \left(\cos \phi_s + \cos \phi_i \right) \tag{3.39c}$$

3.6.2 *Configuration-2*

The closed-form bistatic RCS in the principal xy-plane by the AMC1-AMC2 hybrid surfaces (Configuration-2) that is represented by Figure 3.15(b) for TE^z-polarized incident fields [i.e., given by (3.10)] is derived in Appendix A.5 and can be written as

$$\sigma_{3\text{-D}} \approx \lim_{r \to \infty} \left[4\pi r^2 \frac{|\mathbf{E}^s|^2}{|\mathbf{E}^i|^2} \right] = \frac{4\pi r^2}{\eta^2 H_0^2} \left| E^s_{AMC1} + E^s_{AMC2} \right|^2 \tag{3.40}$$

and similar to the cases of Configuration-1 that since (in the principal xy-plane)

$$E^s_{r_{AMC1}} \approx E^s_{\theta_{AMC1}} \approx E^s_{r_{AMC2}} \approx E^s_{\theta_{AMC2}} \approx 0 \tag{3.41}$$

both E^s_{AMC1} and E^s_{AMC2} reduce to $E^s_{AMC1} = E^s_{\phi_{AMC1}}$ and $E^s_{AMC2} = E^s_{\phi_{AMC2}}$, respectively.
Then, $E^s_{\phi_{AMC1}}$ and $E^s_{\phi_{AMC2}}$ can be written as

$$E^s_{\phi_{AMC1}} \approx C_1 \frac{\sin (X_1)}{X_1} \left[\sin \phi_s \left(1 - |\Gamma_{AMC1}| e^{j \angle \Gamma_{AMC1}} \right) \right.$$
$$\left. - \sin \phi_i \left(1 + |\Gamma_{AMC1}| e^{j \angle \Gamma_{AMC1}} \right) \right] \frac{e^{-j\beta r}}{r} \tag{3.42a}$$

where

$$C_1 = a_1 b \eta H_0 \frac{j\beta}{4\pi} \tag{3.42b}$$

50

$$X_1 = \frac{\beta b_1}{2} (\cos \phi_s + \cos \phi_i) \tag{3.42c}$$

and

$$E^s_{\phi_{\text{AMC2}}} \approx C_2 \frac{\sin(X_2)}{X_2} \Big[\sin \phi_s \left(1 - |\Gamma_{\text{AMC2}}| e^{j\angle\Gamma_{\text{AMC2}}}\right)$$
$$- \sin \phi_i \left(1 + |\Gamma_{\text{AMC2}}| e^{j\angle\Gamma_{\text{AMC2}}}\right)\Big] \frac{e^{-j\beta r}}{r} \tag{3.43a}$$

where

$$C_2 = a_2 b_2 \eta H_0 \frac{j\beta}{4\pi} \tag{3.43b}$$

$$X_2 = \frac{\beta b_2}{2} (\cos \phi_s + \cos \phi_i) \tag{3.43c}$$

Plots of (3.35) for the AMC1-AMC2 hybrid surfaces of *Configuration*-1 [i.e., Figure 3.15(a)] with $a_1 = b_2 = b_1 = b_2 = 1.5\lambda$ are shown and compared to FEM data when the phase difference between the two AMCs is $\Delta P = \angle\Gamma_{\text{AMC2}} - \angle\Gamma_{\text{AMC1}} = 90°$ in Figures 3.16(a) and (b) for $\phi_i = 90°$ and 120°, respectively. Similarly, plots of (3.40) for the AMC1-AMC2 hybrid surfaces of *Configuration*-2 [i.e., Figure 3.15(b)] with $a_1 = b_2 = b_1 = b_2 = 1.5\lambda$ are shown and compared to FEM data when the phase difference between the two AMCs is $\Delta P = \angle\Gamma_{\text{AMC2}} - \angle\Gamma_{\text{AMC1}} = 90°$, in Figures 3.17(a) and (b) for $\phi_i = 90°$ and 120°, respectively.

The comparisons of both Figures 3.16 and 3.17 between the analytically obtained RCSs and the FEM data show that the PO analytical models are valid at and around the specular direction for hybrid surfaces even with the reflection phases of the AMCs are not limited to 180° and 0° (i.e., PEC and PMC ground planes). Additionally, to illustrate the difference of the RCS-reduction performance of each, the RCSs are examined when $\Delta P = \angle\Gamma_{\text{AMC2}} - \angle\Gamma_{\text{AMC1}} = 0°, 143°, 217°$ and 180° for both *Configurations*-1 and -2. For *Configuration*-1, the data are depicted in Figures 3.18(a) and (b) for $\phi_i = 90°$ and 120°, respectively, and similarly, in Figures 3.19(a) and (b) for *Configuration*-2. As expected, for both configurations and incident angles that when $\Delta P = 0°$ (i.e., the hybrid surface

is one large ground plane), the maximum RCS occurs in the specular direction. Subsequently, when a $180° \pm 37∘$ phase difference is introduced between the two surfaces such as $\Delta P = 143°$ or $217°$, a 10 dB RCS-reduction in the RCS response occurs compared to the case when the $\Delta P = 0°$. Ultimately, a complete destructive interference occurs as expected when the two AMCs of the hybrid surfaces have a $\Delta P = 180°$ phase difference between them. One key difference between the responses of the two configuration when $\Delta P = 180°$ is *Configuration-1* achieves destructive interference in the reflected fields mainly at the secular directions; however, *Configuration-2* achieves destructive interference along the entire principal plane (i.e., xy-plane). Thus for a monostatic RCS-reduction at an obliquely plane wave incident, the second configuration achieves better response, as compared to the first, where it has been verified and shown in [28]. PO was utilized for modeling metasurface-based RCS reduction techniques of dihedral corner reflector on the convex and concave region [28].
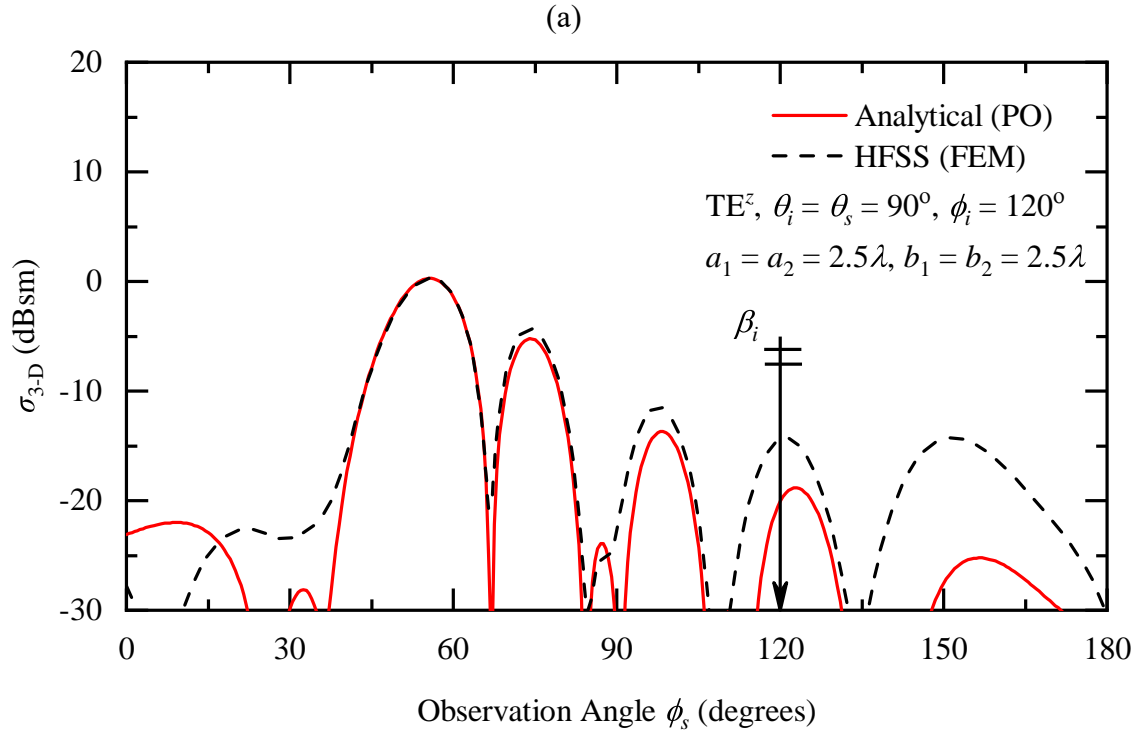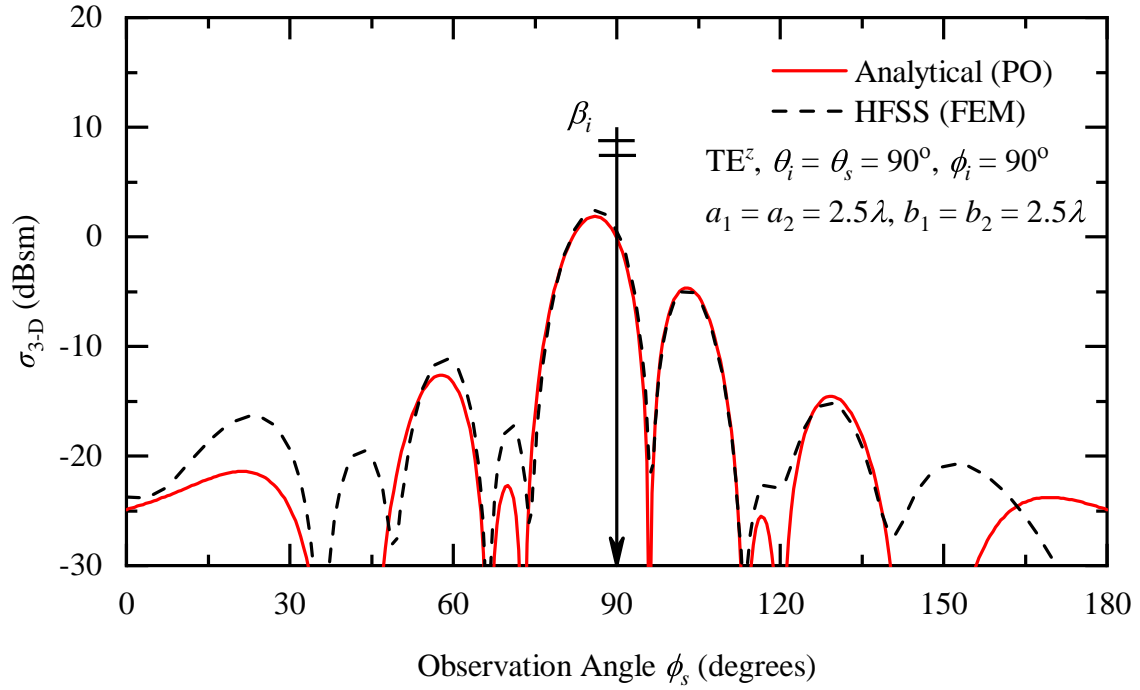
Figure 3.16: Comparison and Validation of Bistatic RCS Patterns Predicted Using PO (Analytical) With Reference to FEM Data For *Configuration*-1 (a) $\phi_i = 90°$, and (b) $\phi_i = 120°$.
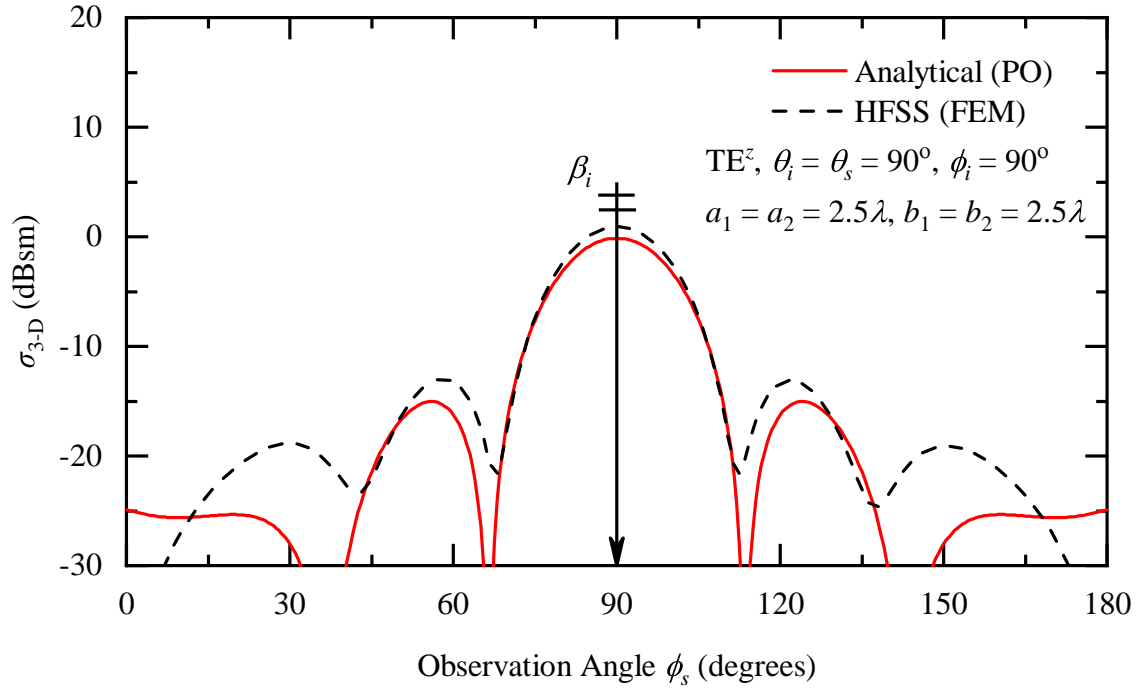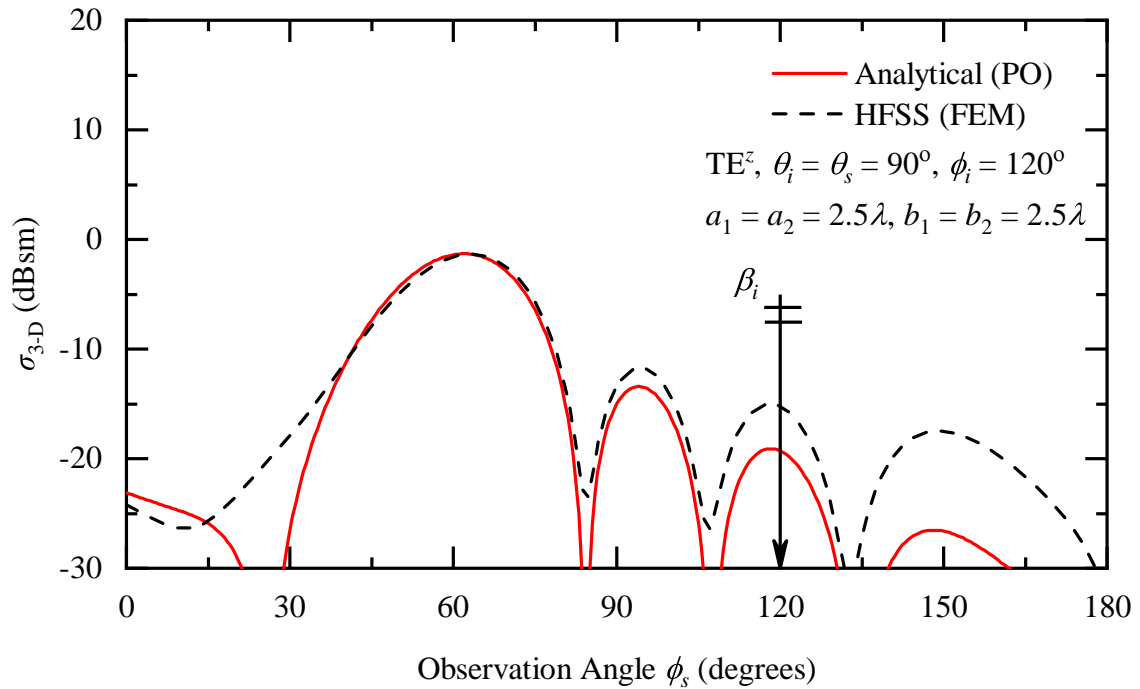
Figure 3.17: Comparison and Validation of Bistatic RCS Patterns Predicted Using PO (Analytical) With Reference to FEM Data For *Configuration*-1 (a) $\phi_i = 90°$, and (b) $\phi_i = 120°$.
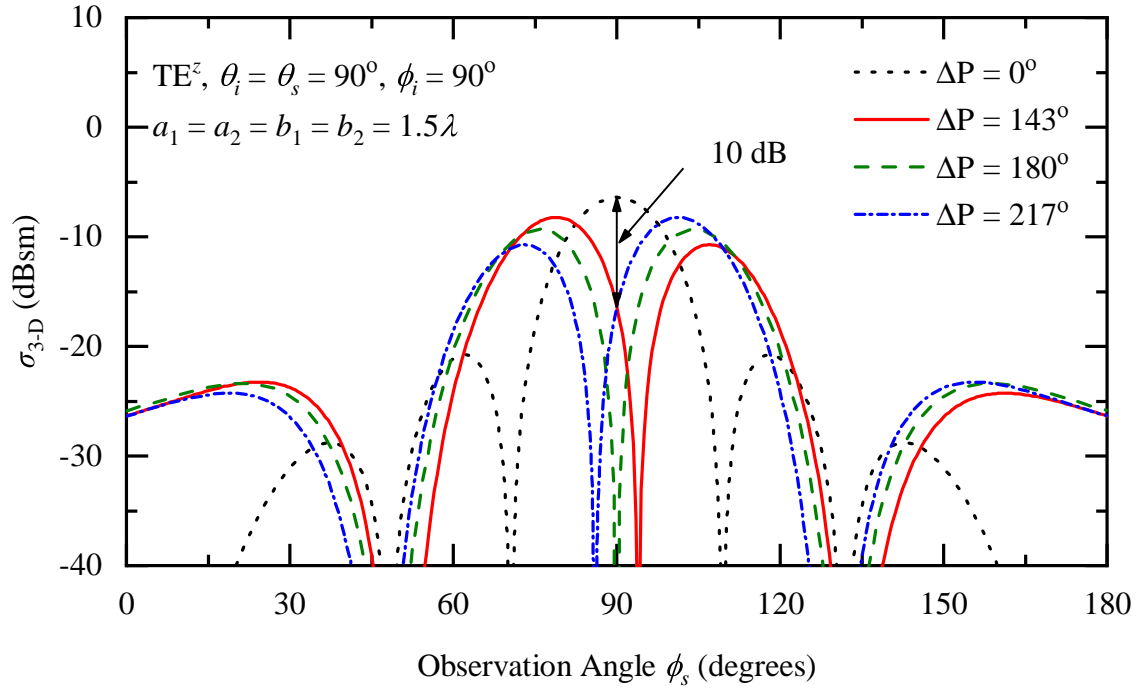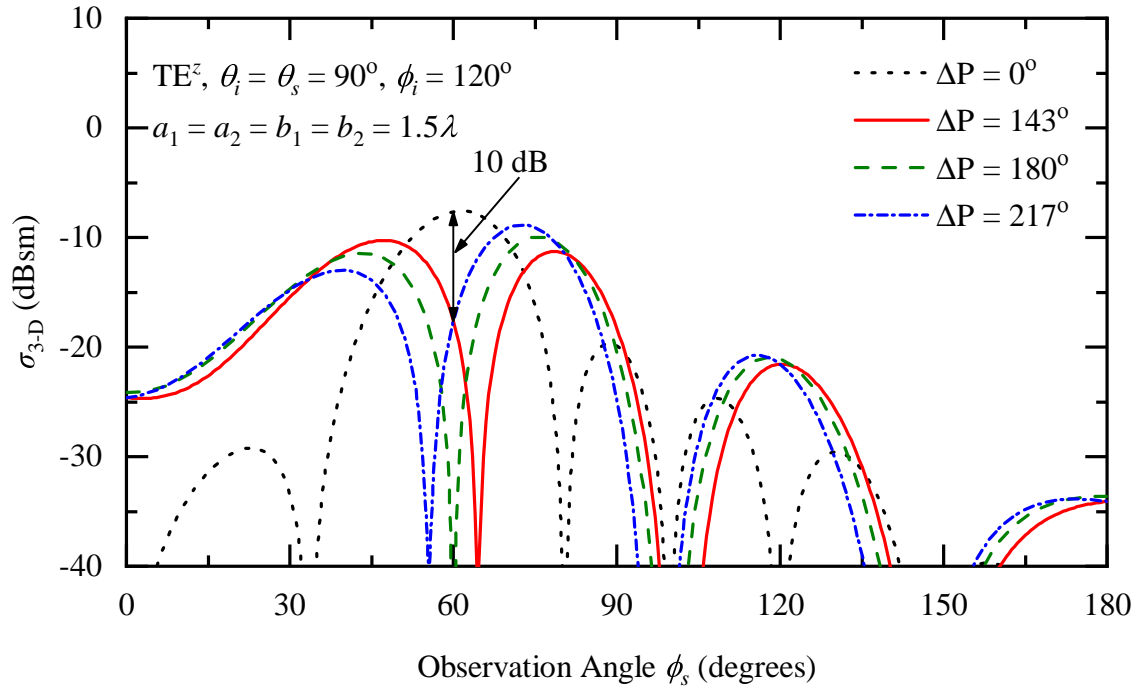
Figure 3.18: Plane Wave Incident on AMC1-AMC2 Hybrid Plates of *Configuration*-1 While Varying the Phase Difference ΔP Between Their Reflection Coefficients (a) $\phi_i = 90°$, and (b) $\phi_i = 120°$.
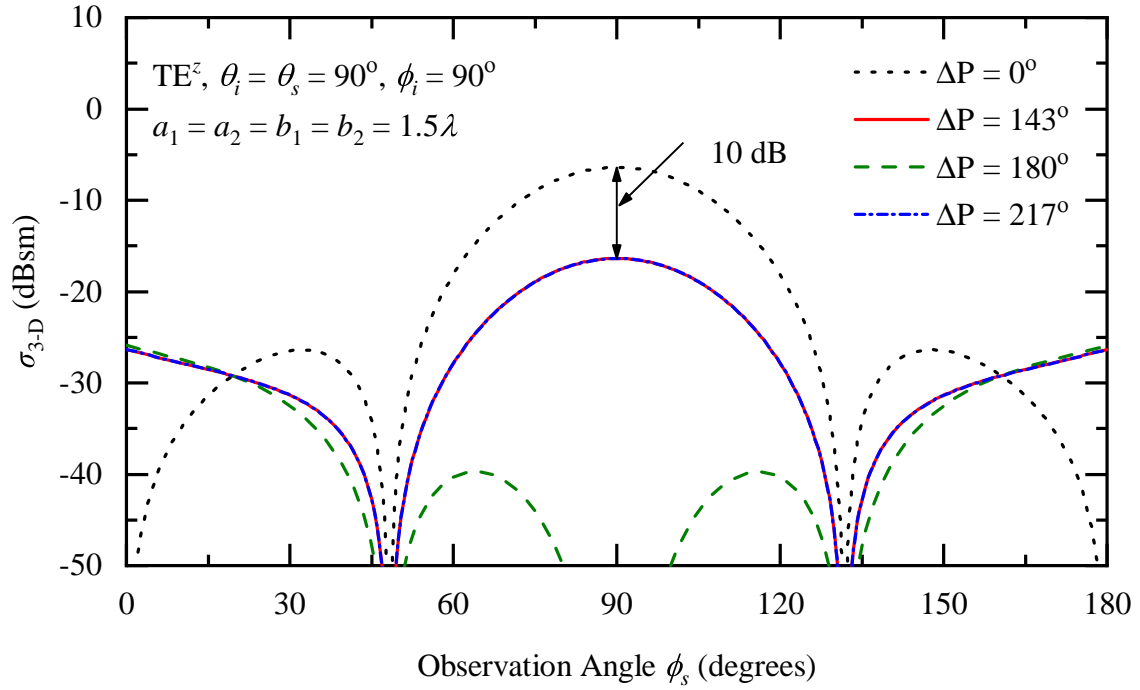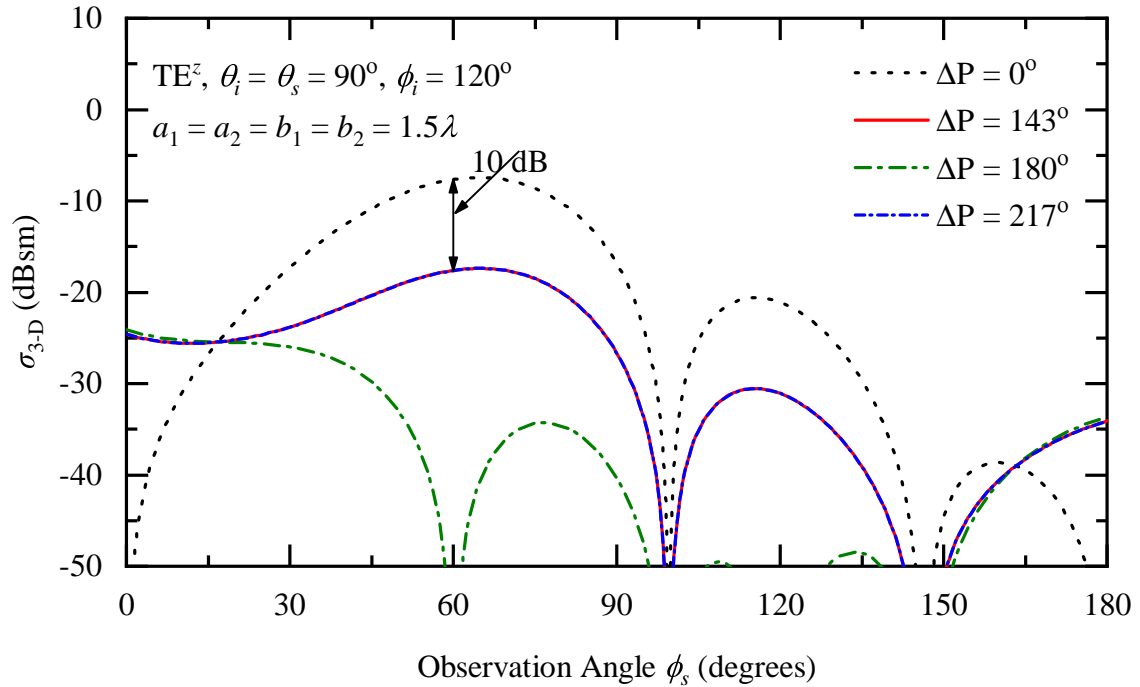
Figure 3.19: Plane Wave Incident on AMC1-AMC2 Hybrid Plates of *Configuration*-2 While Varying the Phase Difference ΔP Between Their Reflection Coefficients (a) $\phi_i = 90°$, and (b) $\phi_i = 120°$.

3.6.3   Configuration-3

One of the features of physical optics is to allow for rapid and efficient optimization of architectural AMC checkerboard designs for broadband RCS-reduction. Generalizing both (3.35) and (3.40) to be applied to four different AMCs, as shown in Figure 3.20(b), would allow for more freedom in design non-uniform checkerboard structures for RCS-reduction as compared to the design equation of (2.5), which is limited to conventional checkerboard surfaces (i.e., two of equal areas) of Figure 3.20(a).
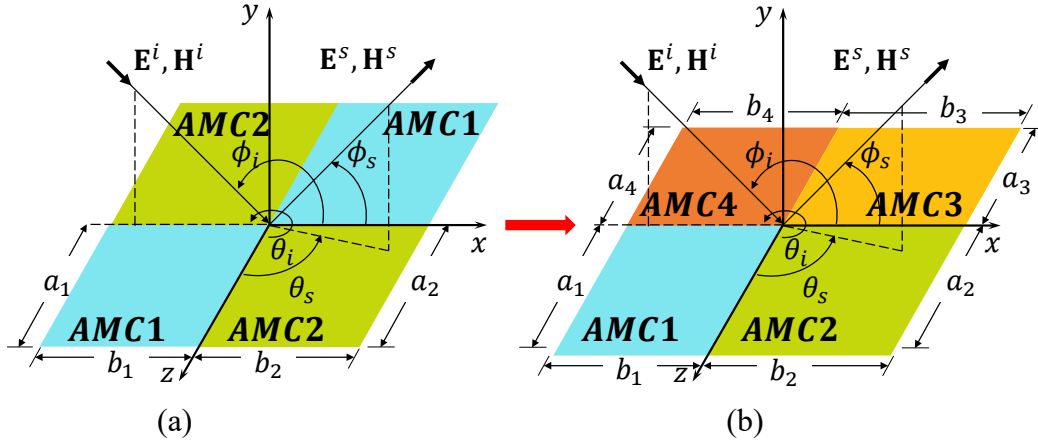
Figure 3.20: Uniform Plane Wave Incident on a (a) Conventional and (b) Non-Uniform Checkerboard Surfaces.

Thus, following similar procedure as outlined in Section 3.1, the RCS of non-uniform checkerboard surfaces which is shown in Figure 3.20(b) and can be written as

$$\sigma_{\text{3-D}} \approx \lim_{r \to \infty} \left[4\pi r^2 \frac{|\mathbf{E}^s|^2}{|\mathbf{E}^i|^2} \right] = \frac{4\pi r^2}{\eta^2 H_0^2} \left| E^s_{\phi_{\text{AMC1}}} + E^s_{\phi_{\text{AMC2}}} + E^s_{\phi_{\text{AMC3}}} + E^s_{\phi_{\text{AMC4}}} \right|^2 \quad (3.44)$$

where $E^s_{\phi_{\text{AMC1}}}$ and $E^s_{\phi_{\text{AMC1}}}$ can be found directly from (3.38a) and (3.39a), receptively. Similar to Subsection 3.6.2, $E^s_{\phi_{\text{AMC3}}}$ and $E^s_{\phi_{\text{AMC4}}}$ can be written as

$$E^s_{\phi_{\text{AMC3}}} \approx C_3 \left[\frac{\sin(2X_3)}{2X_3} + j \sin X_3 \frac{\sin(X_3)}{X_3} \right] \left[\sin \phi_s \left(1 - |\Gamma_{\text{AMC3}}| e^{j \angle \Gamma_{\text{AMC3}}} \right) \right.$$

$$\left. - \sin \phi_i \left(1 + |\Gamma_{\text{AMC3}}| e^{j \angle \Gamma_{\text{AMC3}}} \right) \right] \frac{e^{-j\beta r}}{r}$$

$$(3.45a)$$

where $C_3 = a_3 b_3 \eta H_0 \frac{j\beta}{4\pi}$ and $X_3 = \frac{\beta b_3}{2}(\cos\phi_s + \cos\phi_i)$ and

$$E^s_{\phi_{\text{AMC4}}} \approx C_4 \left[\frac{\sin(2X_4)}{2X_4} - j\sin X_4 \frac{\sin(X_4)}{X_4} \right] \left[\sin\phi_s \left(1 - |\Gamma_{\text{AMC4}}|e^{j\angle\Gamma_{\text{AMC4}}}\right) \right.$$
$$\left. - \sin\phi_i \left(1 + |\Gamma_{\text{AMC4}}|e^{j\angle\Gamma_{\text{AMC4}}}\right) \right] \frac{e^{-j\beta r}}{r}$$

(3.46a)

where $C_4 = a_4 b_4 \eta H_0 \frac{j\beta}{4\pi}$ and $X_4 = \frac{\beta b_4}{2}(\cos\phi_s + \cos\phi_i)$.

Additionally, for normal incident ($\phi_i = 90°$), the monostatic RCS ($\phi_i = 90°$) is reduced to

$$\sigma_{\text{3-D}} \approx \frac{4\pi}{\lambda^2} \left| a_1 b_1 |\Gamma_{\text{AMC1}}| e^{j\angle\Gamma_{\text{AMC4}}} + a_2 b_2 |\Gamma_{\text{AMC2}}| e^{j\angle\Gamma_{\text{AMC2}}} \right.$$
$$\left. + a_3 b_3 |\Gamma_{\text{AMC3}}| e^{j\angle\Gamma_{\text{AMC3}}} + a_4 b_4 |\Gamma_{\text{AMC4}}| e^{j\angle\Gamma_{\text{AMC4}}} \right|^2$$

(3.47)

A non-uniform checkerboard structure, which was reported in [14], is used to verify (3.44). The structure has four AMC surfaces as illustrated in Figure 3.21 and a fabricated finite prototype shown in Figure 3.22; the reflection phases of AMCs are exhibited in Figure 3.23. Applying (3.44) for the specified size and reflection coefficients of each surface, the RCS is obtained and compared with measurements in in Figure 3.24; a good agreement is indicated.
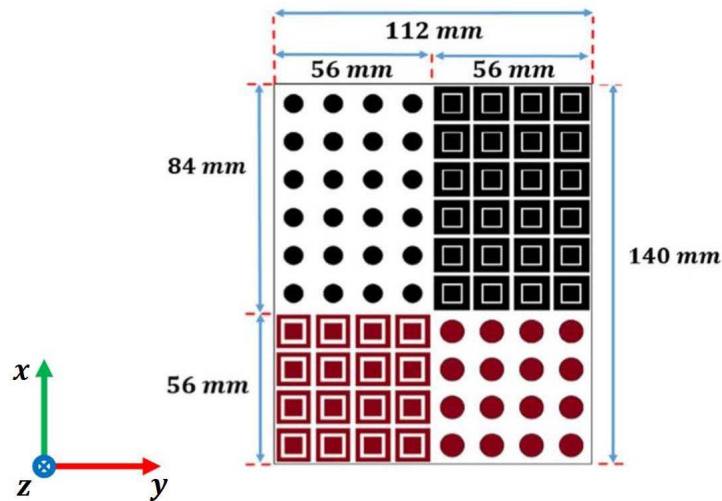
Figure 3.21: A Prototype of a Non-Uniform Checkerboard Surface [14].
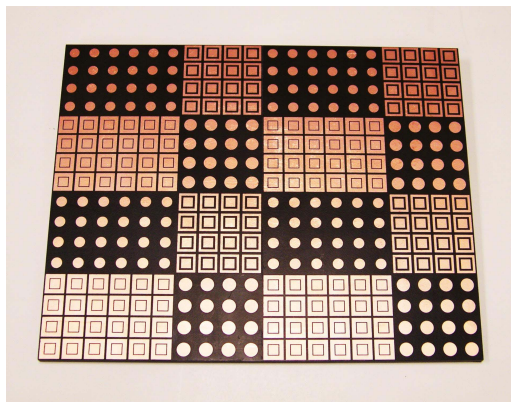
Figure 3.22: A Fabricated Finite Prototype of Figure 3.21 [14].
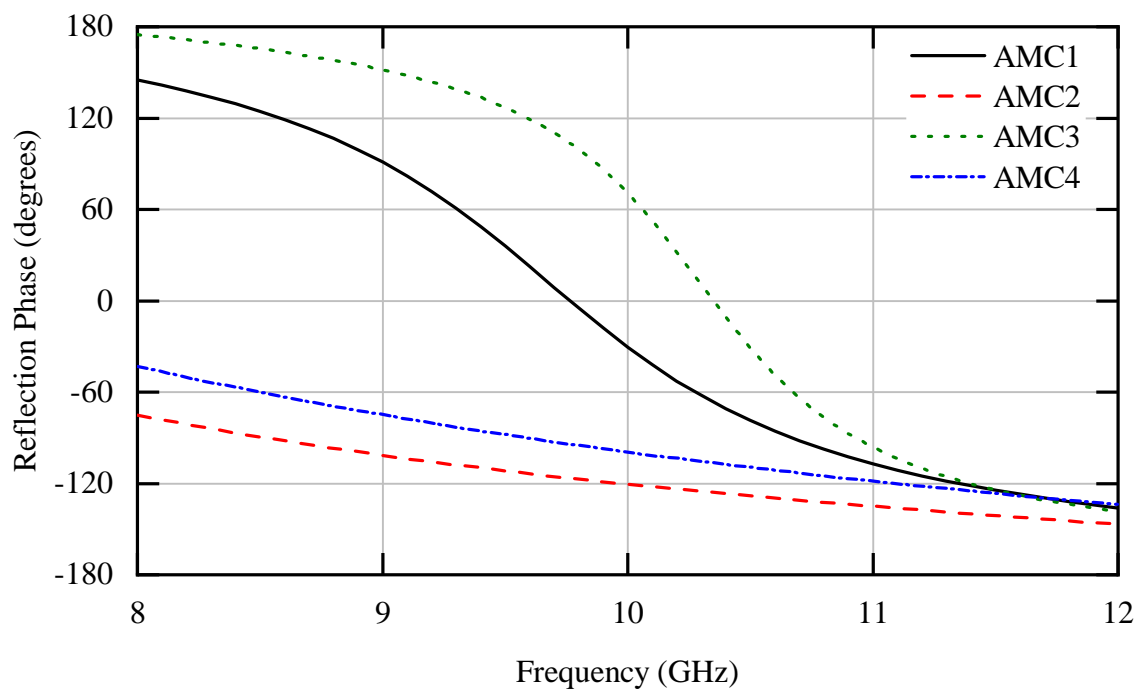
Figure 3.23: Reflection Phases of AMC1, AMC2, AMC3 and AMC4 Surfaces.
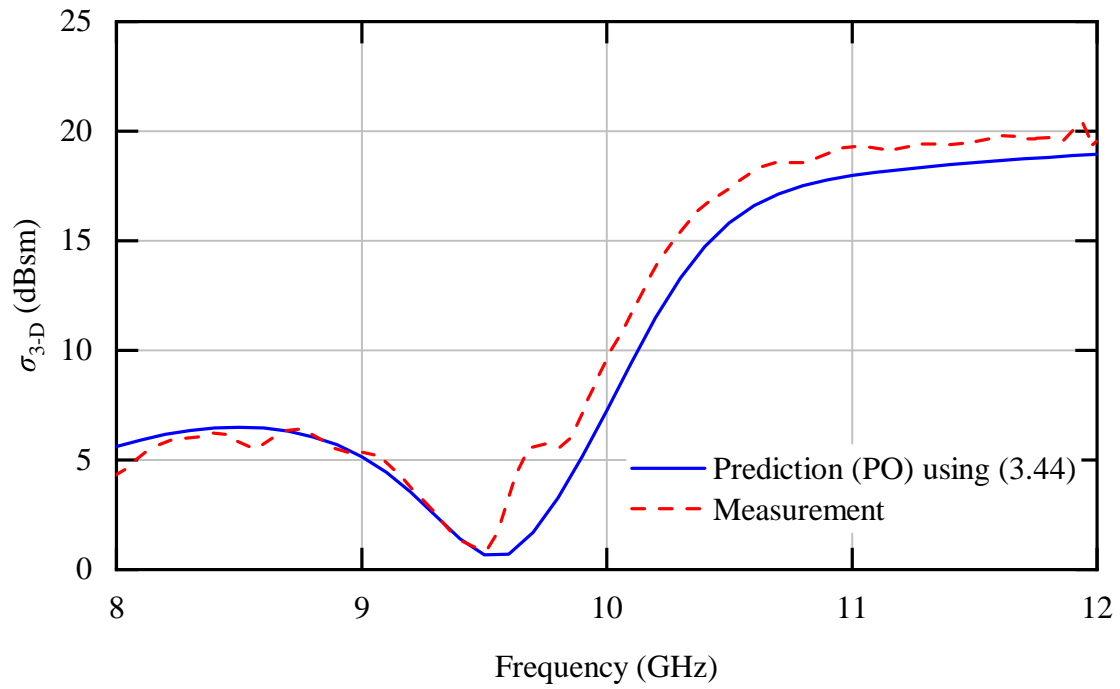
Figure 3.24: Comparison of RCS Obtained From Measurement and PO Prediction of Non-Uniform Checkerboard Surface (i.e., Figure 3.22).

Chapter 4

A RETRODIRECTIVE MICROSTRIP ANTENNA ARRAY WITH LOW

BACKSCATTERING

In Chapter 2, target low observability was achieved by reducing the RCS of such targets using scattering cancellation (i.e., checkerboard AMCs). Furthermore, it was shown in Chapter 3 that the same concept can be applied to reduce the backscattering of antennas. In this chapter, a two-dimensional microstrip antenna array is utilized to design a retrodirective reflector such as a Van Atta reflector.

4.1   Conventional Van Atta Reflector

In many radar and communication systems, reflectors are utilized because of their ability to maximize the re-radiation towards the direction of wave incidence. Such a response can be achieved using a *retrodirective reflector*, first proposed in [29]. The retrodirective reflector is an antenna array whose elements are interconnected by transmission lines such that the received signal is then reradiated towards the direction of incidence [30–32]. In automotive collision avoidance systems, a high scattered field can be achieved only toward near-normal directions to the target surface. Thus, by equipping vehicles and road obstacles with retrodirective reflectors, the self-phasing feature of such reflectors will increase scattering beamwidths and targets will become more visible [32]. Furthermore, retrodirective reflectors have been investigated for the application of wireless power transfer [33–35]. A device that requires wireless power can send a beacon signal that is then received, amplified, and sent back to the user by the retrodirective antenna array.

Generally, retrodirective arrays can be synthesized with basic radiating elements such as dipoles [31]. Also, they can be designed using patch antennas [36–38]. However, due

to the high-backscattering from the structure (consisting of antenna arrays), it *degrades* the performance of the retrodirective reflector by destructively interfering with the desired reradiated fields. Thus, a low-backscattering array of long slots was investigated [39], and it was shown that this reflector could reradiate fields without interference from the array structure's scattering. *However, a retrodirective reflector comprised of a patch antenna array is a better option due to the simplicity of design and the low profile of patch antenna elements if the high backscattering by the patch antenna array can be mitigated.* Thus, artificial magnetic conductor (AMC) technology is utilized to reconfigure the performance of such antenna arrays by reducing scattering from such structures [9, 10].

In this chapter, a Van Atta retrodirective reflector with a smoother backscattering pattern is synthesized and developed using a two-dimensional microstrip-antenna array. Reradiated fields of the conventional retrodirective reflectors are sensitive to the interference by the scattered fields from the antenna array structure. Using a virtual feeding network, structural mode scattering is identified and canceled using metasurfaces.

4.2   Theory of Passive Retrodirective Arrays

A schematic diagram of a 1-D Van Atta array is illustrated in Figure 4.1, where four array elements are connected using the two transmission lines (i.e., elements '1' and '4' are connected with each-other while element '2' is connected to element '3'). In order to direct the reradiated waves back to the direction of the incident wave, these transmission lines must either be of equal lengths or the difference between their lengths should be a multiple of the wavelength. Since these two transmission lines transfer the signals received by elements '1' and '2' to elements '3' and '4', respectively, the lengths of the transmission lines connecting the antenna element should be kept equal to make the functioning frequency independent. Therefore both transmission lines must have equal lengths, $l_1 = l_2 = l$. When a plane wave is incident obliquely upon the array at an angle θ_i, a phase delay Δ between

the antenna elements is introduced [40]

$$\Delta = \beta_0 d \sin \theta_t \tag{4.1}$$

where β_0 is the phase propagation constant in free space and can be given as $\beta_0 = 2\pi/\lambda_0$.
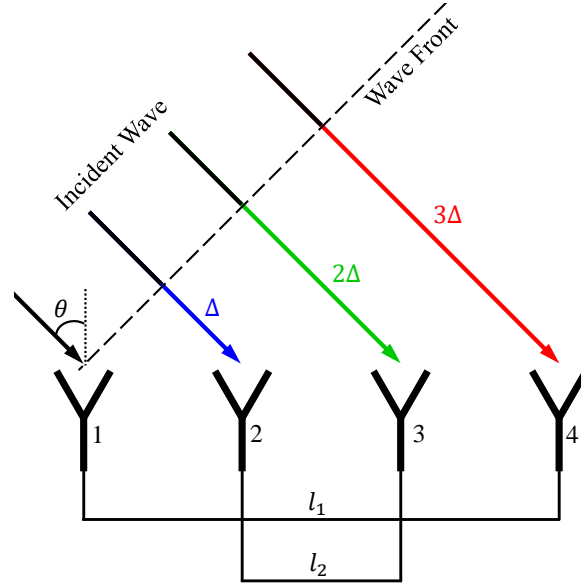
Figure 4.1: A Schematic Diagram of a 1-D Van Atta Retrodirective Array Where Four Elements Are Used in the Array.

The monostatic RCS of the retrodirective reflector, based on the reradiated fields only, can be derived following the approach in [38, 39] and represented by

$$\sigma^R = \frac{\lambda_0^2}{4\pi} G_0^2 \tag{4.2}$$

where G_0 is the gain of the array in the principle plane, θ is the incident/elevation angle, and λ_0 is the free-space wavelength. *It is important to emphasize that the monostatic RCS (σ^R) of (4.2) is based only on the reradiating fields ($\mathbf{E^R}$) by the reflector array.* However, the total RCS by the reflector array (σ^T) corresponds to the total radiated fields ($\mathbf{E^T}$) which can be determined by adding the reradiated fields ($\mathbf{E^R}$) and the scattered fields by the structure ($\mathbf{E^S}$), such as

$$\mathbf{E^T} = \mathbf{E^R} + \mathbf{E^S} \tag{4.3}$$

63

Figure 4.2 shows a comparison of the ideal monostatic RCS between a retrodirective reflector (σ^R) of (4.2) and a flat PEC plate, where both have the same size. The retrodirective response is obtained by having a planar array of 4×4 radiating elements, each of gain $G_0(\theta)$ and with $0.5\lambda_0$ spacing between them. Thus, the total size of both the reflector array and the flat PEC plate is $2\lambda_0 \times 2\lambda_0$. It is clear from Figure 4.2 that the fully passive reflector array can offer a maximum reradiation towards the direction of incidence. However, due to the limitation of the patch antenna towards the grazing angles, the maximum reradiation pattern follows the radiation pattern of the single antenna.
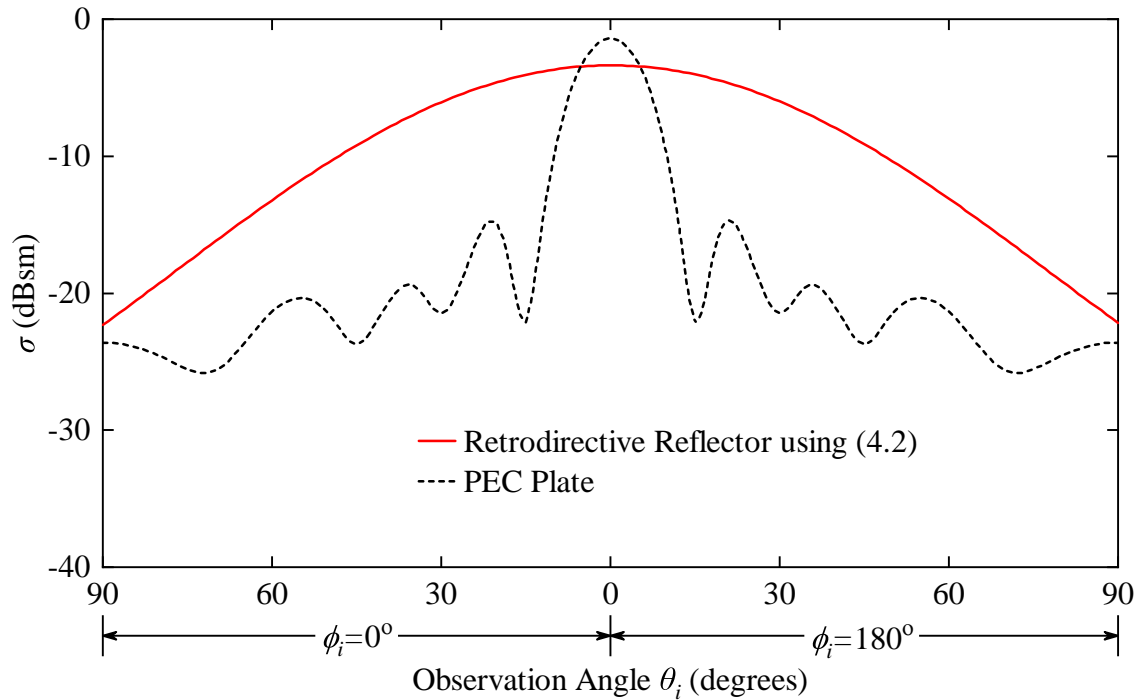
Figure 4.2: Comparison of the Ideal Monostatic RCS Between a Retrodirective Reflector (σ^R) Obtained by Using (4.2) and a Flat PEC.

4.3 Design of the Patch Antenna and Its Feeding Network

In principle, a retrodirective array can be implemented with any kind of antenna element where the bandwidth performance and beamwidth of the array will be directly impacted by

the performance parameters of the single radiating element. Due to their design simplicity and their low profile, patch antennas are chosen to design the utilized retrodirective array.

4.3.1 Aperture-Coupled Patch Antenna With Microstrip Line Feeding Network

Figure 4.3 illustrates the retrodirective reflector that is constructed using a 4×4 finite array of rectangular microstrip-patch antennas.

| (a) | (b) |
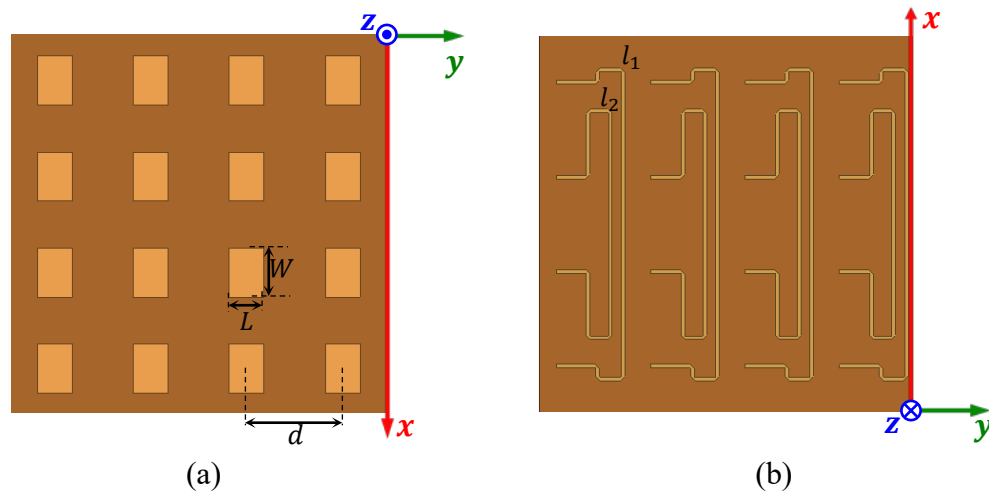
Figure 4.3: The Geometry of the Four by Four Finite Array of Rectangular Microstrip Patch Antennas That Are Connected in the Van Atta Configuration in the *xz-Plane*, (a) Top. (B) Bottom.

The elements are interconnected as per the Van Atta configuration (i.e., illustrated in Figure 4.1) in the *xz*-plane. The feeding network is constructed using 50-ohm microstrip transmission lines of equal length (i.e., $l = l_1 = l_2$). The dimensions of the square array along the *x*- and *y*-direction are 120 mm, corresponding to $2\lambda_0$; λ_0 is the free-space wavelength at 5 GHz. The top side of the structure consists of sixteen patch elements resonating at 5 GHz. With reference to Figure 4.3, the array spacing is $d = 30$ mm ($0.5\lambda_0$), and the patch dimensions are $L = 11$ mm and $W = 15.4$ mm. All the elements are designed on Rogers-RO3006 dielectric substrate (thickness = 1.28 mm, $\varepsilon_r = 6.15$ and $\tan \delta = 0.0022$ at 10 GHz) backed by a PEC.

The above-mentioned design, modeled in HFSS, was illuminated by a plane wave inci-

dent along the principal plane (*xz*-plane) defined by $\phi_i = 0°, 180°$ and for $0° \leq \theta_i \leq 90°$. The configuration was simulated with two different lengths (l) of the transmission lines that are connecting the antenna elements. The total monostatic RCSs (σ^T) of the retrodirective array for the two transmission lines are depicted in Figure 4.4. *The difference between the two responses is primarily due to the change in the phase of $\mathbf{E}^\mathbf{R}$ with respect to $\mathbf{E}^\mathbf{S}$ when the length of the transmission lines is changed.*
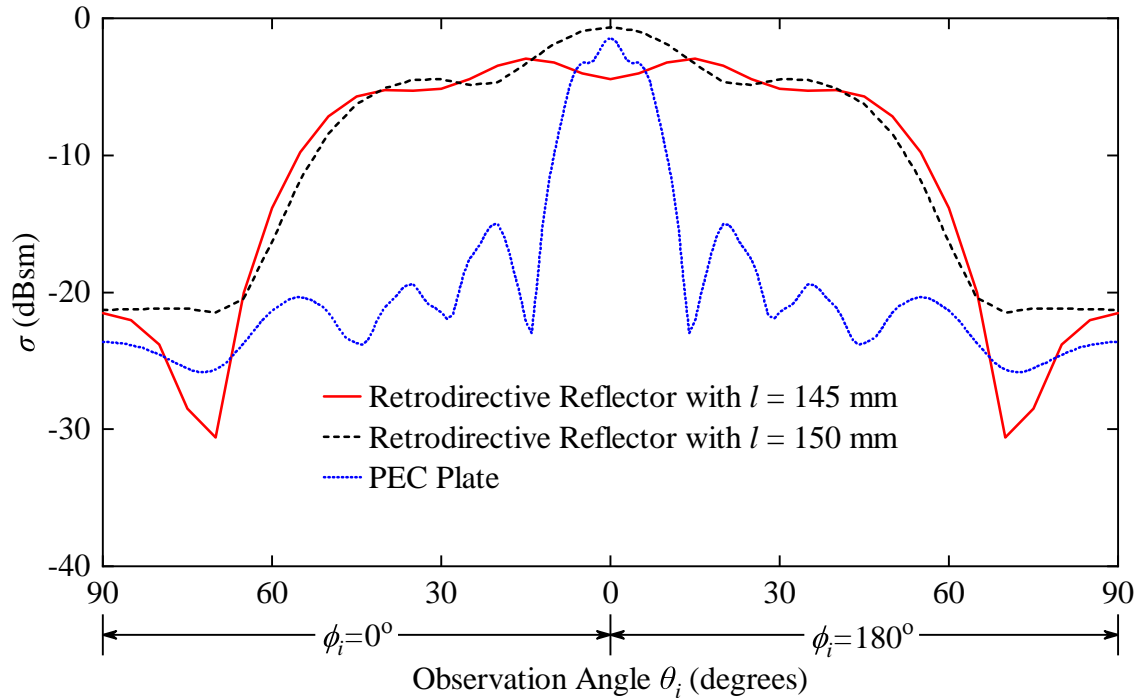
Figure 4.4: The Monostatic RCSs of a Retrodirective Array With Two Different Transmission Line Lengths Compared to the Monostatic RCS of a PEC Plate of the Same Size.

Table 4.1 summarizes the values of the broadside RCS ($\theta_i = 0°$) of the retrodirective array for the two different lengths of transmission line. It is assumed that the phase of the scattered fields by the array structure ($\mathbf{E}^\mathbf{S}$) does not vary significantly with the change of length l of the transmission line (this will be verified in the next section). Thus, the total scattered ($\mathbf{E}^\mathbf{T}$) will depend on the varying phase introduced by the transmission line. As seen in Table 4.1, for the first length of $l = 145$ mm, the two components ($\mathbf{E}^\mathbf{S}$ and

66

$\mathbf{E^R}$) of $\mathbf{E^T}$ added destructively near broadside incidence, while for the second length of $l = 150$ mm, the two components are in-phase and thus the total RCS is higher than the reradiated σ^R obtained using (4.2). With the current retrodirective setup (aperture-coupled patch antenna with microstrip line feeding network), it is extremely difficult to extract the two components of the total scattered fields. In the next section, it will be shown that the virtual feeding network can be used to identify the two separate components of the total scattered field, and it can permit the targeting and cancellation of one of the components, especially the scattering by the structural mode, which is undesirable.

	$l = 145$ mm	$l = 150$ mm	Analytical using (4.2)
σ (dBsm)	-4.42	-0.63	-3.24

Table 4.1: The Broadside ($\theta_i = 0°$) RCS of the Retrodirective Array For Two Different Coaxial Cable Lengths.

4.3.2 Aperture-Coupled Patch Antenna with Virtual Feeding Network

An alternative method for simulating the retrodirective reflector, detailed in Subsection 4.3.1, is to use a virtual feeding network. The basic concept of a virtual feeding network is to capture how much voltage (magnitude and phase) is received by each antenna element, and then feed the measured voltages to the respective antenna elements following the Van Atta configuration shown in Figure 4.1. All the radiating elements of the array are terminated with an impedance equal to the input impedance of the antenna (ideally 50 ohms). Then, at the termination point, the received voltage from the illuminating plane wave is determined by integrating along the electric field lines around the microstrip lines, similar to quasi-static simulators. This integration is performed based on the mode of propagation, which is Quasi-Transverse Electromagnetic (Quasi-TEM), as illustrated in Figure 4.5 [41]. The above-mentioned process is achieved by using a co-simulation between the full-wave simulator (Ansys Electromagnetic Suite/HFSS) [42], and a Python code that is written to integrate the

electric fields and then feed the calculated voltages to their respective elements in the full-wave simulator. Figure 4.6 shows the structure that was configured in HFSS [42]. Here, each of the antenna ports (i.e., transmitting antennas) is terminated with an impedance that is equal to the input impedance of the corresponding connected antenna (i.e., receiving antenna) to replicate the connection between them.

—— E-fields   - - - - H-fields
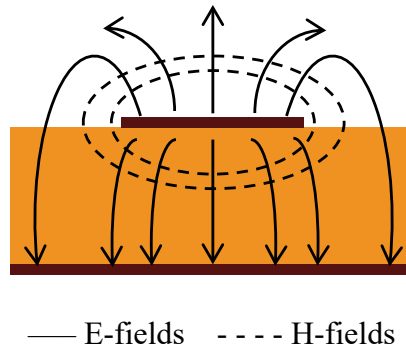
Figure 4.5: Electric and Magnetic Field Lines For the TEM Mode of a Coaxial Line.

(a)   (b)
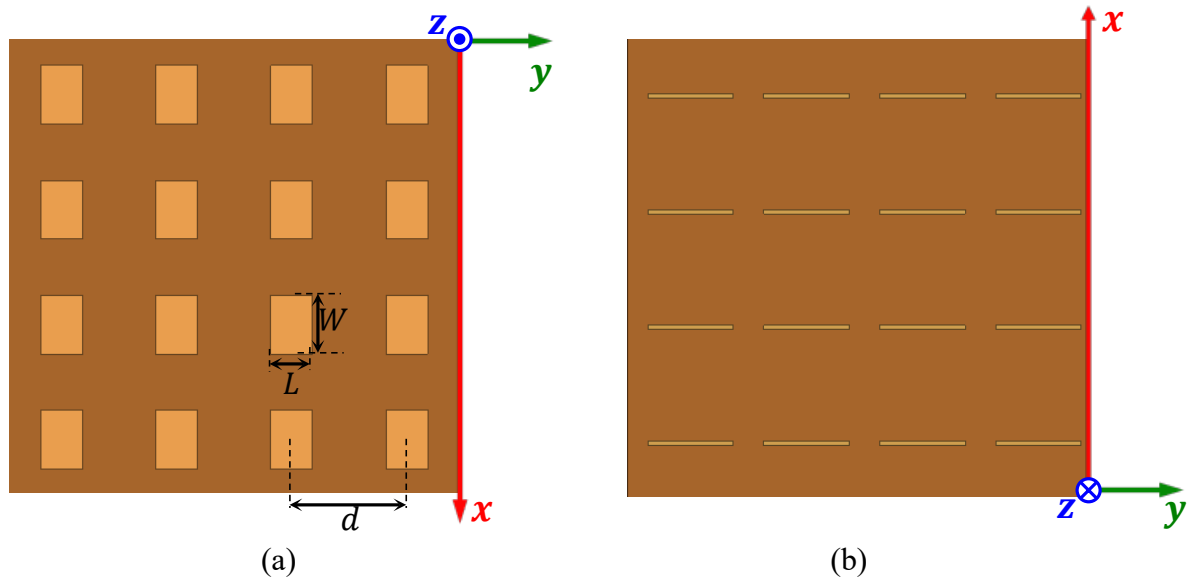
Figure 4.6: (a) Top and (b) Bottom Geometries of the 4x4 Finite Array of Rectangular Microstrip-Patch Antennas That Are Terminated and Virtually Connected in the Van Atta Configuration in the *xz*-Plane.

Similar to the arrangement of Subsection 4.3.1, the structure is illuminated by a plane wave incident in the principal plane (*xz*-plane) defined by $\phi_i = 0°, 180°$ and for $0 \leq \theta_i \leq$

68

90°. Again, by using the Python script, the voltage captured by each antenna element at each incident angle is recorded and fed again to their counterpart reradiating element. This process allows for the decoupling of the total scattered fields $\mathbf{E^T}$ into the two main components: reradiated fields $\mathbf{E^R}$ and structural mode scattering $\mathbf{E^S}$; their corresponding RCSs are shown in Figure 4.7. It can be shown that the phase of $\mathbf{E^S}$ is primarily dependent on the structure, and it is not impacted by the phase introduced by the connecting cables; however, the phase of $\mathbf{E^R}$ can be altered based on the connecting cables. Thus, to illustrate the impact of the phase difference (Δ_{RS}) at the broadside (θ_i) between $\mathbf{E^S}$ and $\mathbf{E^R}$, the total RCS by the retrodirective array is shown in Figure 4.7 when $\Delta_{RS} = 0°$ and 180°, respectively.
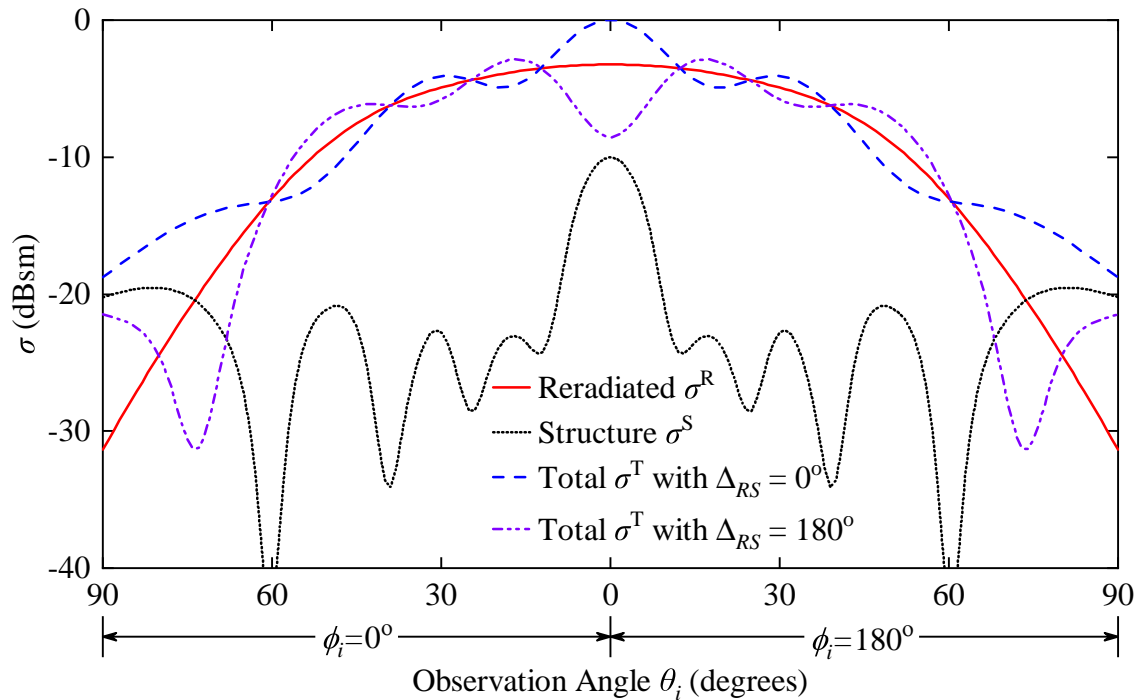
Figure 4.7: The Monostatic RCSs Based on the Reradiated, Scattered, and the Total Fields When the Phase Difference (Δ_{RS}) Between $\mathbf{E^R}$ and $\mathbf{E^S}$ is 0° and 180°.

4.4 Retrodirective Reflector With Low Backscattering Using Metamaterials

It was shown in the previous section that the scattered fields from the structure introduce ripples in the total RCS by the reflector, especially near the broadside, where the RCS of the structure is large. Ideally, $\mathbf{E^S}$ can be canceled by a judiciously synthesized metasurface, like that of the widely-known concept of checkerboard metasurfaces [43–45].

4.4.1 Design of Metasurfaces based on AMCs for RCS Reduction of Retrodirective Array

The RCS of the array structure can be reduced by placing an AMC (i.e., shown in Figure 4.8(a)), whose reflection is similar in magnitude but with a 180° phase difference compared to that of $\mathbf{E^S}$ next the retrodirective reflector as illustrated in Figure 4.8(b). As shown in Figure 4.7, the RCS of the structural mode is around -10 dBsm and the phase of its reflected fields is around 130°. Thus, an AMC surface of square patches is designed where their width and unit cell dimensions are selected to have a reflection phase of around $-50°$ and an RCS of -10 dBsm, similar to the monostatic RCS corresponding to the structural mode of the antenna. The geometries of the synthesized finite sized AMC metasurface are depicted in Figure 4.8(a). As a result, as illustrated in Figure 4.8(b), the final design of the proposed retrodirective reflector is obtained by placing the original antenna array of Figure 4.6 adjacent to the synthesized AMC of Figure 4.8(a). This configuration will introduce fields by the AMC with a phase difference of 180° compared to the phase of the scattered fields by the antenna structure.

This design is then illuminated by following a similar arrangement to the retrodirective reflector without the AMC, as detailed previously in Section 4.3. The monostatic RCSs due to the antenna structure, reradiated fields, and the total fields are shown in Figure 4.9. It can be seen that regardless of the phase introduced by the connecting cables that impact the phase of the reradiated fields only, the monostatic RCS caused by the structure σ^S is reduced
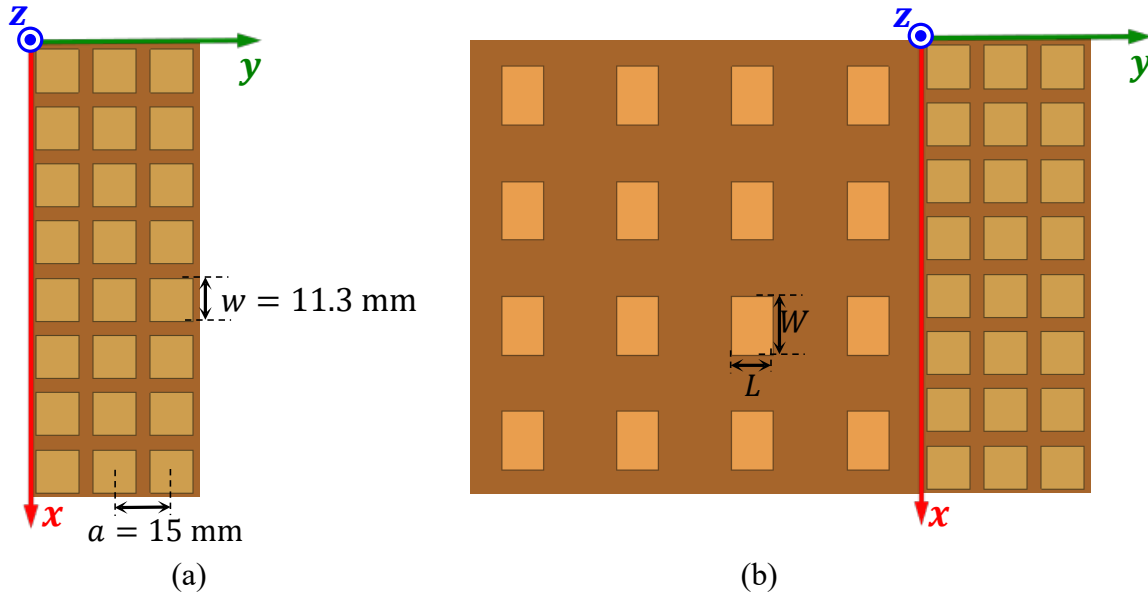
Figure 4.8: Geometries of (a) the Finite Array of the AMC and (b) the 4x4 Array of Rectangular microstrip Patch Antennas Combined With the Finite AMC Array for Canceling the RCS of the Structure.

at and near broadside. Therefor, the total RCS has smaller ripples and the performance becomes less sensitive to the interference by the scattered fields of the structure.

The RCS, which corresponds to the fields scattered by the antenna structure, can be reduced by placing a metasurface with a similar RCS and 180° phase difference with respect to the reflected fields of the antenna array. The range of the phase difference can be relaxed to achieve an RCS reduction of at least 10 dB when the phase difference is maintained within $(180 \pm 37)°$ [13, 43]. Using this criterion, the RCS of various antennas has been reduced for more than 10 dB over a wide frequency band [43–47]; furthermore, a 10-dB RCS reduction is not necessary here. It is sufficient that the RCS of the scattered fields is lower than that of the reradiated fields by a certain factor based on the acceptable level of the ripples in the total field. Consequently, the phase-difference criterion of $(180 \pm 37)°$ can be relaxed further, and a much broader operational bandwidth can be attained. In this model, the metasurface is designed to achieve the RCS-reduction at the operating frequency of the Van Atta reflector to validate the concept, which can be applied over a broader frequency
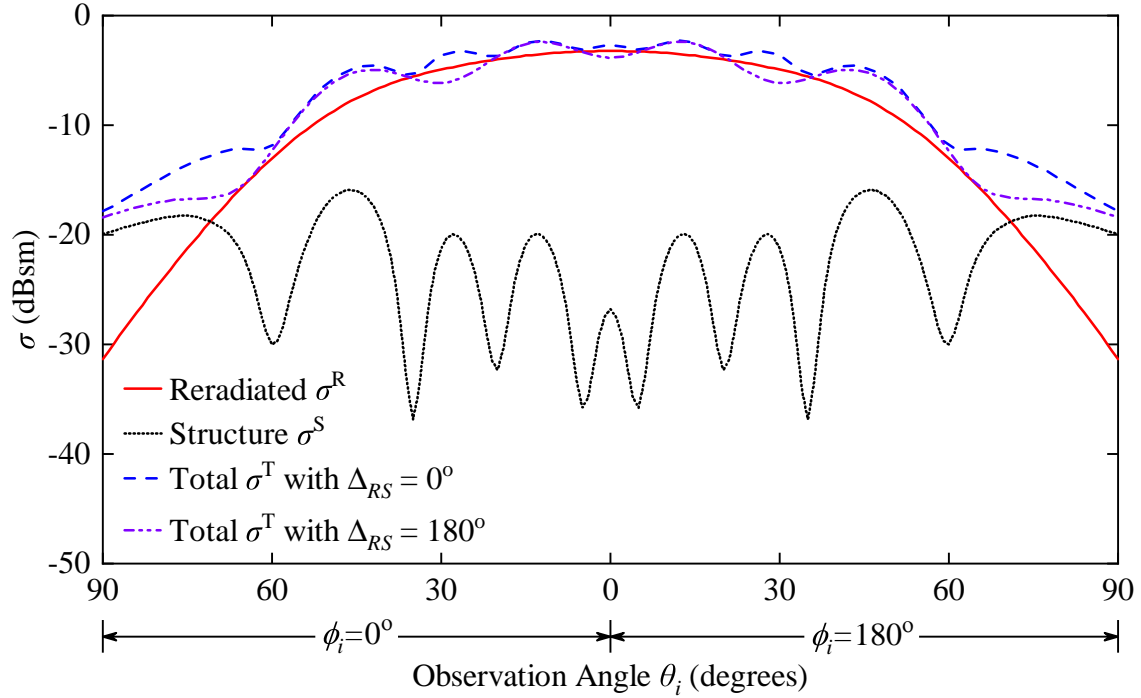
Figure 4.9: The Monostatic RCSs Based on the Reradiated, Scattered, and the Total Fields When the Phase Difference (Δ_{RS}) Between $\mathbf{E^R}$ and $\mathbf{E^S}$ is 0° and 180°.

range.

The scanning capability of the Van Atta reflector depends on the overall gain G_0 of the array, as given by (4.2), where G_0 is determined by the radiation pattern of the single element and the spacing between them. Thus, individual radiating elements with broad beamwidths result in a reflector that responds to larger incident angles. However, antennas with broad beamwidths usually have a lower gain; as a figure-of-merit, the 10-dB beamwidth of the array is considered as its scanning range. In this design, the monostatic RCS plotted in Figure 4.9 shows that the 10-dB beamwidth of the designed array is about 120° in the principle scanning plane (i.e., xz-plane).

4.5   Summary

The concept of retrodirective arrays and its analytical monostatic RCSs have been reviewed. A co-simulation method that allows for decoupling the total scattered fields is introduced. Such a simulation allows the identification and cancellation of the undesired component in the scattered fields (those scattered by the antenna structure). It is shown that *this work enables the use of retrodirective arrays comprised of simple patch antennas while simultaneously addressing the issue of backscattering by using metasurfaces based on AMCs.*

Chapter 5

CONCLUSIONS AND FUTURE WORK

5.1   Conclusions

In the last few years, a new method of reducing the RCS of targets utilizing AMCs was introduced. This method, in contrast to target geometrical alteration, does not require re-shaping of such targets. One of the critical research aspects of this technique is to improve the operational frequency bandwidth while reducing the thickness of the AMCs. *In this dissertation, a procedure to design a wideband RCS-reduction using checkerboard patterned surfaces by utilizing the circuit model of AMC surfaces is proposed and advanced.* The principle of the design is to follow the impact of each AMC parameter (i.e., outer dimensions, substrate thickness, and patch size) on its *bandwidth* and *resonant frequency* and thus expand the overall bandwidth of RCS-reduction. It is demonstrated that by using the proposed guidelines, the RCS-reduction bandwidth can be increased while reducing the thickness of the substrate. Using the proposed method, a 10-dB RCS-reduction bandwidth of 99% has been achieved from 3.95 GHz to 14.70 GHz. The RCS-reduction bandwidth performance of the proposed design was compared with other well-known wideband checkerboard surfaces, and it exhibits the largest 10-dB RCS-reduction bandwidth.

One of the goals of engineering technology is to provide simple and practical solutions to analyze complex problems. Electromagnetic waves scattering from checkerboard surfaces for RCS-reduction applications can be obtained using computationally intensive methods such as FEM. Additionally, high-frequency asymptotic techniques, such as Physical Optics (PO), can be utilized to understand better and provide physical insight into the operation principles of scattering by checkerboard surfaces. *Thus, bistatic scattered fields of various*

74

hybrid surfaces, including checkerboard patterned AMCs surfaces, were obtained and analyzed using PO. The various geometrical configurations AMC structures include hybrid conducting plates (PEC/PMC), hybrid AMC surfaces of two configurations, checkerboard patterned surfaces, and non-uniform checkerboard pattern. The presented analytical models are compared with Finite Element Method simulations using the commercial EM software HFSS. A good agreement is observed between the RCS patterns obtained by the PO analytical model and HFSS at and near the specular directions. Furthermore, the RCS of a non-uniform checkerboard patterned structure is compared with measured data of a fabricated prototype, and a good agreement is attained.

Retrodirective reflector arrays are utilized in many radar and communication systems because of their ability to redirect the scattered fields towards the direction of wave incidence. They can be implemented with any type of radiating element where the total fields generated by the array is the summation between reradiating fields by the antenna element and the array structure. Conventional retrodirective reflectors are sensitive to the interference by the fields scattered from the antenna structure. The method of RCS-reduction using scattering cancellation was utilized to improve the performance of a retrodirective Van Atta reflector antenna array. *Thus, controlled HFSS simulation using Python script allows for the decoupling of the total field into two scattered components (i.e., reradiated and structural).* Subsequently, by using AMC technology, the scattering from the array structure is canceled, which improves the performance of the retrodirective array.

5.2   Future Work

Several research areas were investigated in this dissertation; thus, future research topics extending this work are several. Further logical extensions and advancement can be considered as subsequent studies for future work, which are summarized in what follows:

- The proposed derivation of (3.44) showed that it is accurate for RCS prediction of

non-uniform checkerboard structures, compared to (2.5), when it is limited to two AMCs of equal areas. This increases the degrees of freedom when selecting the AMC surfaces to achieve 10-dB RCS reduction in the specular directions. Therefore, it should be investigated if wider bandwidth of RCS reduction can be achieved.

- The PO-based solutions that were detailed in Chapter 3 are for AMC planar surfaces. However, they can be extended to address scattering of AMCs on dihedral and trihedral corner reflectors.

- The 1-D retrodirective Van Atta antenna array was designed using microstrip transmission lines, and it was illustrated to have smooth reradiated fields utilizing AMCs. This concept can be expanded and applied to 2-D retrodirective arrays. Other array designs, such as the bow-tie and loop antenna elements, can also be considered to extend the bandwidth response of the retrodirective array.

REFERENCES

[1] C. A. Balanis, *Advanced Engineering Electromagnetics*. 2nd Ed., John Wiley & Sons, 2012.

[2] E. F. Knott, J. F. Shaeffer, and M. T. Tuley, *Radar Cross Section*. 2nd Ed., SciTech Pub., 2004.

[3] W. W. Salisbury, "Absorbent body for electromagnetic waves," U.S. Patent 2 599 944, June 10, 1952.

[4] R. L. Fante and M. T. McCormack, "Reflection properties of the salisbury screen," *IEEE Transactions on Antennas and Propagation*, vol. 36, no. 10, pp. 1443–1454, Oct. 1988.

[5] N. Engheta, "Thin absorbing screens using metamaterial surfaces," *IEEE Antennas and Propagation Society International Symposium*, vol. 2, pp. 392–395, 2002.

[6] Z. S. Sacks, D. M. Kingsland, R. Lee, and J.-F. Lee, "A perfectly matched anisotropic absorber for use as an absorbing boundary condition," *IEEE Transactions on Antennas and Propagation*, vol. 43, no. 12, pp. 1460–1463, Dec. 1995.

[7] F. Costa, A. Monorchio, and G. Manara, "Analysis and design of ultra thin electromagnetic absorbers comprising resistively loaded high impedance surfaces," *IEEE Transactions on Antennas and Propagation*, vol. 58, no. 5, pp. 1551–1558, May 2010.

[8] F. Costa and A. Monorchio, "A frequency selective radome with wideband absorbing properties," *IEEE Transactions on Antennas and Propagation*, vol. 60, no. 6, pp. 2740–2747, June 2012.

[9] D. Sievenpiper, "High-impedance electromagnetic surfaces," Ph.D. dissertation, Department of Electrical Engineering, UCLA, 1999.

[10] D. Sievenpiper, L. Zhang, R. F. J. Broas, N. G. Alexopolous, and E. Yablonovitch, "High-impedance electromagnetic surfaces with a forbidden frequency band," *IEEE Transactions on Microwave Theory and Techniques*, vol. 47, no. 11, pp. 2059–2074, Nov. 1999.

[11] M. Paquay, J.-C. Iriarte, I. Ederra, R. Gonzalo, and P. de Maagt, "Thin AMC structure for radar cross-section reduction," *IEEE Transactions on Antennas and Propagation*, vol. 55, no. 12, pp. 6030–6038, Dec. 2007.

[12] J. C. I. Galarregui, A. T. Pereda, J. L. M. de Falcon, I. Ederra, R. Gonzalo, and P. de Maagt, "Broadband radar cross-section reduction using AMC technology," *IEEE Transactions on Antennas and Propagation*, vol. 61, no. 12, pp. 6136–6143, Dec. 2013.

[13] W. Chen, C. A. Balanis, and C. R. Birtcher, "Checkerboard EBG surfaces for wideband radar cross section reduction," *IEEE Transactions on Antennas and Propagation*, vol. 63, no. 6, pp. 2636–2645, June 2015.

[14] A. Y. Modi, C. A. Balanis, C. R. Birtcher, and H. N. Shaman, "Novel design of ultrabroadband radar cross section reduction surfaces using artificial magnetic conductors," *IEEE Transactions on Antennas and Propagation*, vol. 65, no. 10, pp. 5406–5417, Oct. 2017.

[15] S. H. Esmaeli and S. H. Sedighy, "Wideband radar cross-section reduction by AMC," *Electronics Letters*, vol. 52, no. 1, pp. 70–71, Jan. 2016.

[16] D. Sang, Q. Chen, L. Ding, M. Guo, and Y. Fu, "Design of checkerboard amc structure for wideband RCS reduction," *IEEE Transactions on Antennas and Propagation*, vol. 67, no. 4, pp. 2604–2612, April 2019.

[17] A. Y. Modi, C. A. Balanis, and C. R. Birtcher "Novel technique for enhancing RCS reduction bandwidth of checkerboard surfaces," in *IEEE Antennas and Propagation International Symposium*, San Diego, CA, pp. 1911–1912, 2017.

[18] A. Y. Modi, C. A. Balanis, and C. R. Birtcher "AMC cells for broadband RCS reduction checkerboard surfaces," in *IEEE Antennas and Propagation International Symposium*, San Diego, CA, pp. 1915–1916, 2017.

[19] W. Pan, C. Huang, P. Chen, X. Ma, C. Hu, and X. Luo, "A low-RCS and high-gain partially reflecting surface antenna," *IEEE Transactions on Antennas and Propagation*, vol. 62, no. 2, pp. 945–949, Feb. 2014.

[20] Y. Zheng, J. Gao, X. Cao, Z. Yuan, and H. Yang, "Wideband RCS reduction of a microstrip antenna using artificial magnetic conductor structures," *IEEE Antennas and Wireless Propagation Letters*, vol. 14, pp. 1582–1585, 2015.

[21] Y. Jia, Y. Liu, H. Wang, K. Li, and S. Gong, "Low-RCS, high-gain, and wideband mushroom antenna," *IEEE Antennas and Wireless Propagation Letters*, vol. 14, pp. 277–280, 2015.

[22] Y. Liu, K. Li, Y. Jia, Y. Hao, S. Gong, and Y. J. Guo, "Wideband RCS reduction of a slot array antenna using polarization conversion metasurfaces," *IEEE Transactions on Antennas and Propagation*, vol. 64, no. 1, pp. 326–331, Jan. 2016.

[23] C. A. Balanis, M. A. Amiri, A. Y. Modi, S. Pandi, and C. R. Birtcher, "Applications of AMC-based impedance surfaces," *EPJ Appl. Metamat.*, vol. 5, no. 3, pp. 1–15, June 2018.

[24] M. Alyahya, C. A. Balanis, C. R. Birtcher, H. N. Shaman, W. A. Alomar, and S. M. Saeed, "Design of Ultra-Broadband RCS-Reduction Checkerboard Surface Using AMC Circuit Model," in *IEEE Antennas and Propagation International Symposium*, Atlanta, GA, pp. 1691–1692, 2019.

[25] M. Alharbi, M. A. Alyahya, S. Ramalingam, A. Y. Modi, , C. A. Balanis, and C. R. Birtcher, "Metasurfaces for reconfiguration of multi-polarization antennas and Van Atta reflector arrays," *MDPI Electronics*, vol. 9, no. 1262, pp. 1–22, 2020.

[26] J. S. Asvestas, "The physical optics method in electromagnetic scattering," *AIP Journal of Mathematical Physics*, vol. 21, pp. 290–299, 1980.

[27] P. Y. Ufimtsev, *Fundamentals of the Physical Theory of Diffraction.* 2nd Ed., John Wiley & Sons, 2014.

[28] A. Y. Modi, M. A. Alyahya, C. A. Balanis, and C. R. Birtcher, "Metasurface-based method for broadband RCS reduction of dihedral corner reflectors with multiple bounces," *IEEE Transactions on Antennas and Propagation*, vol. 68, no. 3, pp. 1436–1447, March 2020.

[29] Patent, l. C. V. Atta, "Electromagnetic reflector," U.S. Patent 2 908 002, Oct. 1959.

[30] E. Sharp and M. Diab, "Van Atta reflector array," *IRE Transactions on Antennas and Propagation*, vol. 8, no. 4, pp. 436–438, July 1960.

[31] J. Appel-Hansen, "A Van Atta reflector consisting of half-wave dipoles," *IEEE Transactions on Antennas and Propagation*, vol. 14, no. 6, pp. 694–700, Nov. 1966.

[32] S.-J. Chung and K. Chang, "A retrodirective microstrip antenna array," *IEEE Transactions on Antennas and Propagation*, vol. 46, no. 12, pp. 1802–1809, Dec. 1998.

[33] Y. Li and V. Jandhyala, "Design of retrodirective antenna arrays for short-range wireless power transmission," *IEEE Transactions on Antennas and Propagation*, vol. 60, no. 1, pp. 206–211, Jan. 2012.

[34] X. Wang, S. Sha, J. He, L. Guo, and M. Lu, "Wireless power delivery to low-power mobile devices based on retro-reflective beamforming," *IEEE Antennas and Wireless Propagation Letters*, vol. 13, pp. 919–922, 2014.

[35] M. Ettorre, W. A. Alomar, and A. Grbic, "Radiative wireless power-transfer system using wideband, wide-angle slot arrays," *IEEE Transactions on Antennas and Propagation*, vol. 65, no. 6, pp. 2975–2982, June 2017.

[36] W.-J. Tseng, S.-B. Chung, and K. Chang, "A planar van atta array reflector with retrodirectivity in both e-plane and h-plane," *IEEE Transactions on Antennas and Propagation*, vol. 48, no. 2, pp. 173–175, Feb. 2000.

[37] J. G. D. Hester and M. M. Tentzeris, "Inkjet-printed flexible mm-wave Van-Atta reflectarrays: A solution for ultralong-range dense multitag and multisensing chipless RFID implementations for IoT smart skins," *IEEE Transactions on Microwave Theory and Techniques*, vol. 64, no. 12, pp. 4763–4773, Dec. 2016.

[38] S. Christie, R. Cahill, N. B. Buchanan, V. F. Fusco, N. Mitchell, Y. V. Munro, and G. Maxwell-Cox, "Rotman lens-based retrodirective array," *IEEE Transactions on Antennas and Propagation*, vol. 60, no. 3, pp. 1343–1351, March 2012.

[39] M. Ettorre, W. A. Alomar, and A. Grbic, "2-d Van Atta array of wideband, wideangle slots for radiative wireless power transfer systems," *IEEE Transactions on Antennas and Propagation*, vol. 66, no. 9, pp. 4577–4585, Sep. 2018.

[40] C. A. Balanis, *Antenna Theory: Analysis and Design.* 4th Ed., John Wiley & Sons, 2016.

[41] D. M. Pozar, *Microwave Engineering*. 4th Ed., John Wiley, 2012.

[42] ANSYS, Inc., Canonsburg, PA, USA. [Online]. Available: http://www.ansys.com

[43] A. Y. Modi, C. A. Balanis, C. R. Birtcher, and H. N. Shaman, "New class of RCS-reduction metasurfaces based on scattering cancellation using array theory," *IEEE Transactions on Antennas and Propagation*, vol. 67, no. 1, pp. 298–308, Jan. 2019.

[44] A. Y. Modi, C. A. Balanis, C. R. Birtcher, and H. Shaman "Phasor Representation Method for Synthesizing RCS-Reduction Metasurfaces," in *IEEE Antennas and Propagation International Symposium*, Boston, MA, pp. 2279–2280, 2018.

[45] A. Y. Modi, C. A. Balanis, and C. R. Birtcher "Investigation of Checkerboard Metasufaces on Flexible Curvilinear Structure for RCS Reduction," in *IEEE Antennas and Propagation International Symposium*, Boston, MA, pp. 2329–2330, 2018.

[46] Y. Liu, K. Li, Y. Jia, Y. Hao, S. Gong, and Y. J. Guo, "Wideband RCS reduction of a slot array antenna using polarization conversion metasurfaces," *IEEE Transactions on Antennas and Propagation*, vol. 64, no. 1, pp. 326–331, Jan. 2016.

[47] Y. Zheng, J. Gao, Y. Zhou, X. Cao, H. Yang, S. Li, and T. Li, "Wideband gain enhancement and RCS reduction of fabry–perot resonator antenna with chessboard arranged metamaterial superstrate," *IEEE Transactions on Antennas and Propagation*, vol. 66, no. 2, pp. 590–599, Feb. 2018.

APPENDIX A

PHYSICAL OPTICS

A.1   Scattering from PEC

A.1.1   *Parallel Polarization (TE^z) - PEC*

First, by considering parallel-polarized incident fields that are given by (3.10a) and (3.10b) and using the reflection coefficient of a PEC plate (i.e, $\Gamma = -1$), the surface current densities on PEC plate can be found by using (3.13) and (3.15) as

$$M_x = M_y = M_z = 0 \tag{A.1}$$

and

$$J_y \approx J_z \approx 0 \ \text{ and } \ J_x \approx 2H_0 e^{j\beta x' \cos\phi_i} \tag{A.2}$$

Then, the integrals of (3.7a)-(3.7d) can be reduced in the principle xy-plane (i.e., $\theta_s = 90°$ and $0 \leqslant \theta_s \leqslant 180°$) to

$$
\begin{aligned}
N_\theta &= L_\theta = L_\phi = 0 \\
N_\phi &= \iint_S -J_x \sin\phi_s e^{j\beta(x'\sin\theta_s\cos\phi_s + z'\cos\theta_s)}\, dx'\, dz' \\
&= -2aH_0 \sin\phi_s \int_{-b/2}^{b/2} e^{j\beta x'(\sin\theta_s\cos\phi_s + \cos\theta_i)}\, dx' \int_{-a/2}^{a/2} e^{j\beta z'\cos\theta_s}\, dz' \\
&= -2aH_0 \sin\phi_s \int_{-b/2}^{b/2} e^{j\beta x'(\cos\phi_s + \cos\theta_i)}\, dx' \\
N_\phi &= -2abH_0 \sin\phi_s \left[\frac{\sin(X)}{X}\right]
\end{aligned}
\tag{A.3}
$$

where

$$X = \frac{\beta b}{2}(\cos\phi_s + \cos\phi_i)$$

by substituting (A.3) into (3.6a)-(3.6c), the scattered fields can be written as

$$E_r^s \approx E_\theta^s \approx 0 \ \text{ and } \ E_\phi^s \simeq -\frac{j\beta e^{-j\beta r}}{4\pi r}\eta N_\phi$$

Thus,

$$E_\phi^s \simeq abH_0\eta\frac{j\beta}{2\pi}\sin\phi_s \left[\frac{\sin\left(\frac{\beta b}{2}(\cos\phi_s + \cos\phi_i)\right)}{\frac{\beta b}{2}(\cos\phi_s + \cos\phi_i)}\right]\frac{e^{-j\beta r}}{r} \tag{A.4}$$

The RCS can then be written as

$$\sigma_{3\text{-D}} \approx \lim_{r\to\infty}\left[4\pi r^2 \frac{|\mathbf{E}^s|^2}{|\mathbf{E}^i|^2}\right]$$

$$\approx 4\pi\left(\frac{ab}{\lambda}\right)^2\sin^2\phi_s\left|\frac{\sin\left[\frac{\beta b}{2}(\cos\phi_s + \cos\phi_i)\right]}{\frac{\beta b}{2}(\cos\phi_s + \cos\phi_i)}\right|^2 \tag{A.5}$$

A.1.2 Perpendicular Polarization (TM^z) - PEC

Similar to the parallel wave polarization of Subsection *A.1.1*, the surface current densities induced on the PEC plate by a perpendicularly-polarized incident fields which are represented by (3.17a) and (3.17b) can be *approximated* as [using (3.20) and (3.22)]

$$M_x = M_y = M_z = 0 \tag{A.6}$$

and

$$J_x \approx J_y \approx 0 \text{ and } J_z \approx 2\frac{E_0}{\eta}\sin\phi_i e^{j\beta x\cos\phi_i} \tag{A.7}$$

and the integrals

$$N_\phi = L_\theta = L_\phi = 0$$

$$N_\theta = \iint_S -J_z\sin\theta_s e^{j\beta(x'\sin\theta_s\cos\phi_s + z'\cos\theta_s)}\,dx'\,dz'$$

$$= -2\frac{E_0}{\eta}\sin\phi_i\int_{-b/2}^{b/2}e^{j\beta x'(\sin\theta_s\cos\phi_s+\cos\theta_i)}\,dx'\int_{-a/2}^{a/2}e^{j\beta z'\cos\theta_s}\,dz'$$

$$= -2a\frac{E_0}{\eta}\sin\phi_i\int_{-b/2}^{b/2}e^{j\beta x'(\cos\phi_s+\cos\theta_i)}\,dx'$$

$$N_\theta = -2ab\frac{E_0}{\eta}\sin\phi_i\left[\frac{\sin(X)}{X}\right] \tag{A.8}$$

where

$$X = \frac{\beta b}{2} (\cos \phi_s + \cos \phi_i)$$

The scattered fields can then be reduced, by substituting (A.8) into (3.6a)-(3.6c), to

$$E_r^s \approx E_\phi^s \approx 0 \quad \text{and} \quad E_\theta^s \simeq -\frac{j\beta e^{-j\beta r}}{4\pi r} \eta N_\theta$$

Thus,

$$E_\theta^s \approx E_0 ab \frac{j\beta}{2\pi} \sin \phi_i \left[\frac{\sin\left(\frac{\beta b}{2}(\cos \phi_s + \cos \phi_i)\right)}{\frac{\beta b}{2}(\cos \phi_s + \cos \phi_i)} \right] \frac{e^{-j\beta r}}{r} \tag{A.9}$$

The RCS can then be written as

$$\sigma_{3\text{-D}} \approx \lim_{r \to \infty} \left[4\pi r^2 \frac{|\mathbf{E}^s|^2}{|\mathbf{E}^i|^2} \right]$$

$$\approx 4\pi \left(\frac{ab}{\lambda} \right)^2 \sin^2 \phi_i \left| \frac{\sin\left[\frac{\beta b}{2}(\cos \phi_s + \cos \phi_i)\right]}{\frac{\beta b}{2}(\cos \phi_s + \cos \phi_i)} \right|^2 \tag{A.10}$$

A.2   Scattering From PMC

A.2.1   *Parallel Polarization (TE^z) - PMC*

By following procedure of obtaining the RCS for the PEC plate and with consideration that the reflection coefficient of a PMC plate (i.e, $\Gamma = +1$), the current densities can be *approximated* as

$$J_x = J_y = J_z = 0 \tag{A.11}$$

and

$$M_x \approx M_y \approx 0 \quad \text{and} \quad M_z \approx 2\eta H_0 \sin \phi_i e^{j\beta x' \cos \phi_i} \tag{A.12}$$

Afterwards, the integrals of (3.7a)-(3.7d) can be written in the principle xy-plane (i.e., $\theta_s = 90°$ and $0 \leqslant \theta_s \leqslant 180°$) as

$$N_\theta = N_\phi = L_\phi = 0$$

$$L_\theta = \iint_S -M_z \sin\phi_s e^{j\beta(x'\sin\theta_s\cos\phi_s + z'\cos\theta_s)}\, dx'\, dz'$$

$$= -2a\eta H_0 \sin\phi_i \int_{-b/2}^{b/2} e^{j\beta x'(\sin\theta_s\cos\phi_i + \cos\theta_i)}\, dx' \int_{-a/2}^{a/2} e^{j\beta z'\cos\theta_s}\, dz'$$

$$= -2a\eta H_0 \sin\phi_i \int_{-b/2}^{b/2} e^{j\beta x'(\cos\phi_s + \cos\theta_i)}\, dx'$$

$$L_\theta = -2ab\eta H_0 \sin\phi_i \left[\frac{\sin(X)}{X}\right] \tag{A.13}$$

where

$$X = \frac{\beta b}{2}(\cos\phi_s + \cos\phi_i)$$

Then, by substituting (A.13) into (3.6a)-(3.6c), the scattered fields can be written as

$$E_r^s \approx E_\theta^s \approx 0 \quad \text{and} \quad E_\phi^s \simeq \frac{j\beta e^{-j\beta r}}{4\pi r} L_\theta$$

Thus,

$$E_\phi^s \approx -H_0 \eta ab \frac{j\beta}{2\pi} \sin\phi_i \left[\frac{\sin\left(\frac{\beta b}{2}(\cos\phi_s + \cos\phi_i)\right)}{\frac{\beta b}{2}(\cos\phi_s + \cos\phi_i)}\right] \frac{e^{-j\beta r}}{r} \tag{A.14}$$

The RCS can then be written as

$$\sigma_{\text{3-D}} \approx \lim_{r\to\infty}\left[4\pi r^2 \frac{|\mathbf{E}^s|^2}{|\mathbf{E}^i|^2}\right]$$

$$\approx 4\pi \left(\frac{ab}{\lambda}\right)^2 \sin^2\phi_i \left|\frac{\sin\left[\frac{\beta b}{2}(\cos\phi_s + \cos\phi_i)\right]}{\frac{\beta b}{2}(\cos\phi_s + \cos\phi_i)}\right|^2 \tag{A.15}$$

A.2.2   *Perpendicular Polarization (TM^z) - PMC*

Similar to the parallel wave polarization of Subsection *A.1.1*, the surface current densities induced on the PMC plate by a perpendicularly-polarized incident fields which are

given by (3.17a) and (3.17b) can be *approximated* as [using (3.20) and (3.22)]

$$J_x = J_y = J_z = 0 \tag{A.16}$$

and

$$M_y \approx M_z \approx 0 \text{ and } M_x \approx -2E_0 e^{j\beta x' \cos \phi_i} \tag{A.17}$$

and the integrals of (3.7a)-(3.7d) can be written as

$$L_\theta = N_\phi = L_\theta = 0$$

$$L_\phi = \iint_S -M_x \sin \phi_s e^{j\beta(x' \sin \theta_s \cos \phi_s + z' \cos \theta_s)} \, dx' \, dz'$$

$$= 2E_0 \sin \phi_s \int_{-b/2}^{b/2} e^{j\beta x' (\sin \theta_s \cos \phi_s + \cos \theta_i)} \, dx' \int_{-a/2}^{a/2} e^{j\beta z' \cos \theta_s} \, dz'$$

$$= 2aE_0 \sin \phi_s \int_{-b/2}^{b/2} e^{j\beta x' (\cos \phi_s + \cos \theta_i)} \, dx'$$

$$L_\phi = 2abE_0 \sin \phi_s \left[\frac{\sin(X)}{X} \right] \tag{A.18}$$

where

$$X = \frac{\beta b}{2} (\cos \phi_s + \cos \phi_i)$$

The scattered fields can then be reduced, by substituting (A.18) into (3.6a)-(3.6c), to

$$E_r^s \approx E_\phi^s \approx 0 \text{ and } E_\theta^s \simeq -\frac{j\beta e^{-j\beta r}}{4\pi r} \eta L_\phi$$

Thus,

$$E_\theta^s \approx -E_0 ab \frac{j\beta}{2\pi} \sin \phi_s \left[\frac{\sin\left(\frac{\beta b}{2} (\cos \phi_s + \cos \phi_i)\right)}{\frac{\beta b}{2} (\cos \phi_s + \cos \phi_i)} \right] \frac{e^{-j\beta r}}{r} \tag{A.19}$$

The RCS can then be written as

$$\sigma_{3\text{-D}} \approx \lim_{r \to \infty} \left[4\pi r^2 \frac{|\mathbf{E}^s|^2}{|\mathbf{E}^i|^2} \right]$$

$$\approx 4\pi \left(\frac{ab}{\lambda} \right)^2 \sin^2 \phi_s \left| \frac{\sin\left[\frac{\beta b}{2} (\cos \phi_s + \cos \phi_i) \right]}{\frac{\beta b}{2} (\cos \phi_s + \cos \phi_i)} \right|^2 \tag{A.20}$$

86

A.3 Scattering From PEC-PMC Hybrid Surfaces

A.3.1 *Parallel Polarization (TE^z) - PEC-PMC Hybrid Surfaces*

For a TE^z plane wave incident which is given by [(3.10a) and (3.10b)] on PEC-PMC hybrid surfaces (Figure 3.1(c)), the surface current densities on the hybrid surfaces can be found by using the reflection coefficients of both the PEC plate ($\Gamma = -1$) and PMC plate ($\Gamma = 1$)as:

Electric current density $\mathbf{J}_s$ induced on the PEC surface, ($-b_1/2 \leqslant x \leqslant 0$ and $-a/2 \leqslant z \leqslant a/2$), is written as

$$J_y \approx J_z \approx 0 \text{ and } J_x \approx 2H_0 e^{j\beta x' \cos \phi_i} \tag{A.21}$$

Magnetic current density $\mathbf{M}_s$ induced on the PMC surface, ($0 \leqslant x \leqslant b_2/2$ and $-a/2 \leqslant z \leqslant a/2$), is written as

$$M_x \approx M_y \approx 0 \text{ and } M_z \approx 2\eta H_0 \sin \phi_i e^{j\beta x' \cos \phi_i} \tag{A.22}$$

Then, the integrals of (3.7a)-(3.7d) can be solved in the principle xy-plane (i.e., $\theta_s = 90°$ and $0 \leqslant \theta_s \leqslant 180°$) as

$$N_\theta = L_\phi = 0$$

$$N_\phi = \iint_S -J_x \sin \phi_s e^{j\beta(x' \sin \theta_s \cos \phi_s + z' \cos \theta_s)} \, dx' \, dz'$$

$$N_\phi = -2aH_0 \sin \phi_s \int_{-b_2/1}^{0} e^{j\beta x' (\sin \theta_s \cos \phi_s + \cos \theta_i)} \, dx' \int_{-a/2}^{a/2} e^{j\beta z' \cos \theta_s} \, dz' \tag{A.23}$$

$$L_\theta = \iint_S -M_z \sin \phi_s e^{j\beta(x' \sin \theta_s \cos \phi_s + z' \cos \theta_s)} \, dx' \, dz'$$

$$L_\theta = -2a\eta H_0 \sin \phi_i \int_{0}^{b_2/2} e^{j\beta x' (\sin \theta_s \cos \phi_i + \cos \theta_i)} \, dx' \int_{-a/2}^{a/2} e^{j\beta z' \cos \theta_s} \, dz' \tag{A.24}$$

By using (B.1a) and (B.2a), (A.23) and (A.24) can be reduced to

$$N_\phi = -2ab_1 H_0 \sin\phi_s \left[\frac{\sin(2X_1)}{2X_1} - j \sin X_1 \frac{\sin(X_1)}{X_1} \right] \tag{A.25}$$

$$L_\theta = -2ab_2 \eta H_0 \sin\phi_i \left[\frac{\sin(2X_1)}{2X_1} + j \sin X_2 \frac{\sin(X_1)}{X_1} \right] \tag{A.26}$$

where

$$X_1 = \frac{\beta b_1}{2}(\cos\phi_s + \cos\phi_i) \quad \text{and} \quad X_2 = \frac{\beta b_2}{2}(\cos\phi_s + \cos\phi_i) \tag{A.27}$$

Then, the scattered fields can be written as

$$E_r^s \approx E_\theta^s \approx 0 \quad \text{and} \quad E_\phi^s \simeq \frac{j\beta e^{-j\beta r}}{4\pi r}(L_\theta - \eta N_\phi)$$

Thus,

$$
\begin{aligned}
E_\phi^s \approx \eta H_0 a \frac{j\beta}{2\pi} \Bigg\{ b_1 \sin\phi_s \left[\frac{\sin(2X_1)}{2X_1} - j \sin X_1 \frac{\sin(X_1)}{X_1} \right] \\
- b_2 \sin\phi_i \left[\frac{\sin(2X_2)}{2X_2} + j \sin X_2 \frac{\sin(X_2)}{X_2} \right] \Bigg\} \frac{e^{-j\beta r}}{r}
\end{aligned}
\tag{A.28}
$$

Therefor, the RCS can then be written as

$$
\begin{aligned}
\sigma_{\text{3-D}} &\approx \lim_{r\to\infty} \left[4\pi r^2 \frac{|\mathbf{E}^s|^2}{|\mathbf{E}^i|^2} \right] \\
&\approx \frac{4\pi r^2}{\eta^2 H_0^2} |E_\phi^s|^2
\end{aligned}
\tag{A.29}
$$

where E_ϕ^s is found from (A.28).

A.3.2 *Perpendicular Polarization (TM^z) - PEC-PMC Hybrid Surfaces*

A procedure similar to that used for the TE^z plane wave incident can be used to derive the scattered fields from PEC-PMC hybrid surfaces (Figure 3.1(c)) for TE^z incident plane wave. Thus, by using (3.6a)-(3.6c) and based on the TM^z incident wave that is given by (3.17), the scattered fields can written as

$$E_r^s \approx E_\phi^s \approx 0$$

88

$$E_\theta^s \approx E_0 a \frac{j\beta}{2\pi} \Big(b_1 \sin\phi_i \left[\text{sinc } 2X_1 - j \sin X_1 \text{ sinc } X_1 \right]$$

$$- b_2 \sin\phi_s \left[\text{sinc } 2X_2 + j \sin X_2 \text{ sinc } X_2 \right] \Big) \frac{e^{-j\beta r}}{r} \qquad \text{(A.30)}$$

$$E_\theta^s \approx E_0 a \frac{j\beta}{2\pi} \Bigg\{ b_1 \sin\phi_i \left[\frac{\sin(2X_1)}{2X_1} - j \sin X_1 \frac{\sin(X_1)}{X_1} \right]$$

$$- b_2 \sin\phi_s \left[\frac{\sin(2X_2)}{2X_2} + j \sin X_2 \frac{\sin(X_2)}{X_2} \right] \Bigg\} \frac{e^{-j\beta r}}{r} \qquad \text{(A.31)}$$

where X_1 and X_2 can be found by (A.27). Then, the RCS can then be written as

$$\sigma_{3\text{-D}} \approx \lim_{r\to\infty} \left[4\pi r^2 \frac{|E^s|^2}{|E^i|^2} \right]$$

$$\approx \frac{4\pi r^2}{E_0^2} \left| E_\phi^s \right|^2 \qquad \text{(A.32)}$$

where E_ϕ^s is found from (A.31).

A.4   Scattering From AMC1-AMC2 Hybrid Surfaces - Configuration-1

A procedure similar to that used for the PEC-PMC hybrid surfaces can also be applied to find the scattered fields of the AMC1-AMC2 hybrid surfaces [Figure 3.1(d)]. For AMC1 $(-b_1/2 \leqslant x \leqslant 0$ and $-a_1/2 \leqslant z \leqslant a_1/2)$ and by using its reflection coefficient of Γ_{AMC1}, the induced current densities can be summarized as follows:

$$M_x = M_y = 0 \ \text{ and } \ M_z = \eta H_0 \sin\phi_i e^{j\beta x \cos\phi_i} \left(1 + |\Gamma_{\text{AMC1}}| e^{j\angle\Gamma_{\text{AMC1}}} \right) \qquad \text{(A.33)}$$

$$J_y = J_z = 0 \ \text{ and } \ J_x = H_0 e^{j\beta x \cos\phi_i} \left(1 - |\Gamma_{\text{AMC1}}| e^{j\angle\Gamma_{\text{AMC1}}} \right) \qquad \text{(A.34)}$$

Then, the integrals of (3.7a)-(3.7d) can be written in the principle xy-plane as

$$N_\theta = L_\phi = 0$$

$$N_\phi = \iint_S -J_x \sin\phi_s e^{j\beta(x'\sin\theta_s\cos\phi_s + z'\cos\theta_s)} \, dx' \, dz' \qquad \text{(A.35)}$$

$$L_\theta = \iint_S -M_z \sin\theta_s e^{j\beta(x'\sin\theta_s\cos\phi_s + z'\cos\theta_s)} \, dx' \, dz' \qquad \text{(A.36)}$$

By using (B.1a) and (B.2a), (A.35) and (A.36) can be reduced to

$$N_\phi = -a_1 b_1 H_0 \sin\phi_s \left[\frac{\sin(2X_1)}{2X_1} - j\sin X_1 \frac{\sin(X_1)}{X_1} \right] \left(1 - |\Gamma_{\text{AMC1}}| e^{j\angle\Gamma_{\text{AMC1}}}\right) \quad \text{(A.37)}$$

$$L_\theta = -a_1 b_1 \eta H_0 \sin\phi_i \left[\frac{\sin(2X_1)}{2X_1} - j\sin X_1 \frac{\sin(X_1)}{X_1} \right] \left(1 + |\Gamma_{\text{AMC1}}| e^{j\angle\Gamma_{\text{AMC1}}}\right) \quad \text{(A.38)}$$

where $X_1 = \frac{\beta b_1}{2}(\cos\phi_s + \cos\phi_i)$.

Then, the scattered fields of AMC1 can written as

$$E^s_{r_{\text{AMC1}}} \approx E^s_{\theta_{\text{AMC1}}} \approx 0 \quad \text{and} \quad E^s_{\phi_{\text{AMC1}}} \approx \frac{j\beta e^{-j\beta r}}{4\pi r} \left(L_\theta - \eta N_\phi\right)$$

Thus,

$$E^s_{\phi_{\text{AMC1}}} \approx C_1 \left[\frac{\sin(2X_1)}{2X_1} - j\sin X_1 \frac{\sin(X_1)}{X_1} \right] \left[\sin\phi_s \left(1 - |\Gamma_{\text{AMC1}}| e^{j\angle\Gamma_{\text{AMC1}}}\right) \right.$$
$$\left. - \sin\phi_i \left(1 + |\Gamma_{\text{AMC1}}| e^{j\angle\Gamma_{\text{AMC1}}}\right) \right] \frac{e^{-j\beta r}}{r}$$

$$\text{(A.39)}$$

where $C_1 = a_1 b_1 \eta H_0 \frac{j\beta}{4\pi}$.

Similarly, the scattered fields of AMC2 ($0 \leqslant x \leqslant b_2$ and $-a_2/2 \leqslant z \leqslant a_2/2$) can written as

$$E^s_{r_{\text{AMC2}}} \approx E^s_{\theta_{\text{AMC2}}} \approx 0 \quad \text{and} \quad E^s_{\phi_{\text{AMC2}}} \approx \frac{j\beta e^{-j\beta r}}{4\pi r} \left(L_\theta - \eta N_\phi\right)$$

Thus,

$$E^s_{\phi_{\text{AMC2}}} \approx C_2 \left[\frac{\sin(2X_2)}{2X_2} + j\sin X_2 \frac{\sin(X_2)}{X_2} \right] \left[\sin\phi_s \left(1 - |\Gamma_{\text{AMC2}}| e^{j\angle\Gamma_{\text{AMC2}}}\right) \right.$$
$$\left. - \sin\phi_i \left(1 + |\Gamma_{\text{AMC1}}| e^{j\angle\Gamma_{\text{AMC1}}}\right) \right] \frac{e^{-j\beta r}}{r}$$

$$\text{(A.40)}$$

where $C_2 = ab_2\eta H_0 \frac{j\beta}{4\pi}$ and $X_2 = \frac{\beta b_2}{2}(\cos\phi_s + \cos\phi_i)$.

Accordingly, the RCS can then be written as

$$\sigma_{\text{3-D}} \approx \lim_{r\to\infty}\left[4\pi r^2 \frac{|\mathbf{E}^s|^2}{|\mathbf{E}^i|^2}\right]$$

$$\approx \frac{4\pi r^2}{\eta^2 H_0^2}\left|E^s_{\phi_{\text{AMC1}}} + E^s_{\phi_{\text{AMC2}}}\right|^2 \tag{A.41}$$

where $E^s_{\phi_{\text{AMC1}}}$ and $E^s_{\phi_{\text{AMC2}}}$ are found from (A.39) and (A.40), respectively.

A.5   Scattering From AMC1-AMC2 Hybrid Surfaces - Configuration-2

For the AMC1-AMC2 hybrid surfaces (configuration-2) that is shown in Figure 3.1(e), the integrals of AMC2 ($-b_1/2 \leqslant x \leqslant b_1/2$ and $-a_1 \leqslant z \leqslant 0$) can be expressed in the xy-principle plane as

$$N_\theta = L_\phi = 0 \tag{A.42}$$

$$N_\phi = -a_1 b_1 H_0 \sin\phi_s \left[\frac{\sin(X_1)}{X_1}\right]\left(1 - |\Gamma_{\text{AMC1}}|e^{j\angle\Gamma_{\text{AMC1}}}\right) \tag{A.43}$$

$$L_\theta = -a_1 b_1 \eta H_0 \sin\phi_i \left[\frac{\sin(X_1)}{X_1}\right]\left(1 + |\Gamma_{\text{AMC1}}|e^{j\angle\Gamma_{\text{AMC1}}}\right) \tag{A.44}$$

where $X_1 = \frac{\beta b_1}{2}(\cos\phi_s + \cos\phi_i)$.

Then, the scattered fields of AMC1 can written as

$$E^s_{r_{\text{AMC1}}} \approx E^s_{\theta_{\text{AMC1}}} \approx 0 \quad \text{and} \quad E^s_{\phi_{\text{AMC1}}} \approx \frac{j\beta e^{-j\beta r}}{4\pi r}\left(L_\theta - \eta N_\phi\right)$$

Thus,

$$E^s_{\phi_{\text{AMC1}}} \approx C_1 \frac{\sin(X_1)}{X_1}\left[\sin\phi_s\left(1 - |\Gamma_{\text{AMC1}}|e^{j\angle\Gamma_{\text{AMC1}}}\right)\right.$$

$$\left. - \sin\phi_i\left(1 + |\Gamma_{\text{AMC1}}|e^{j\angle\Gamma_{\text{AMC1}}}\right)\right]\frac{e^{-j\beta r}}{r} \tag{A.45}$$

where $C_1 = a_1 b\eta H_0 \frac{j\beta}{4\pi}$.

Similarly, the scattered fields of AMC2 ($-b_2/2 \leqslant x \leqslant b_2/2$ and $0 \leqslant z \leqslant a_2$) can written

as

$$E^s_{r_{\text{AMC2}}} \approx E^s_{\theta_{\text{AMC2}}} \approx 0 \quad \text{and} \quad E^s_{\phi_{\text{AMC2}}} \approx \frac{j\beta e^{-j\beta r}}{4\pi r}\left(L_\theta - \eta N_\phi\right)$$

Thus,

$$\begin{aligned}
E^s_{\phi_{\text{AMC2}}} \approx C_2 \frac{\sin\left(X_2\right)}{X_2} &\Big[\sin\phi_s \left(1 - |\Gamma_{\text{AMC2}}|e^{j\angle\Gamma_{\text{AMC2}}}\right) \\
&- \sin\phi_i \left(1 + |\Gamma_{\text{AMC2}}|e^{j\angle\Gamma_{\text{AMC2}}}\right)\Big] \frac{e^{-j\beta r}}{r}
\end{aligned} \tag{A.46}$$

where $C_2 = a_2 b_2 \eta H_0 \frac{j\beta}{4\pi}$ and $X_2 = \frac{\beta b_2}{2}\left(\cos\phi_s + \cos\phi_i\right)$.

APPENDIX B

INTEGRATION FORMULAS

$$\int_0^c e^{j\alpha z}\, dz = \frac{e^{\alpha jz}}{j\alpha}\Big|_0^c = \frac{1}{j\alpha}\left[e^{j\alpha c} - 1\right]$$

$$= \frac{1}{j\alpha}\left[\cos(\alpha c) + j\sin(\alpha c) - 1\right]$$

$$= c\,\frac{\sin(\alpha c)}{\alpha c} + \frac{1}{j\alpha}\left[\cos(\alpha c) - 1\right]$$

Since: $\cos(x) - 1 = -2\sin^2\left(\frac{x}{2}\right)$

$$\int_0^c e^{j\alpha z}\, dz = \frac{e^{\alpha jz}}{j\alpha}\Big|_0^c = c\,\frac{\sin(\alpha c)}{\alpha c} + j\left[\frac{2\sin^2(\frac{\alpha}{2}c)}{\alpha}\right]$$

$$= c\,\frac{\sin(\alpha c)}{\alpha c} + j\left[c\,\sin(\frac{\alpha}{2}c)\,\frac{\sin(\frac{\alpha}{2}c)}{\frac{\alpha}{2}c}\right]$$

Thus

$$\int_0^c e^{j\alpha z}\, dz = c\left[\frac{\sin(\alpha c)}{\alpha c} + j\sin(\frac{\alpha}{2}c)\,\frac{\sin(\frac{\alpha}{2}c)}{\frac{\alpha}{2}c}\right] \tag{B.1a}$$

$$\int_{-c}^0 e^{j\alpha z}\, dz = \frac{e^{\alpha jz}}{j\alpha}\Big|_{-c}^0 = \frac{1}{j\alpha}\left[1 - e^{-j\alpha c}\right]$$

$$= \frac{1}{j\alpha}\left[1 - \cos(\alpha c) + j\sin(\alpha c)\right]$$

$$= c\,\frac{\sin(\alpha c)}{\alpha c} + \frac{1}{j\alpha}\left[1 - \cos(\alpha c)\right]$$

Since: $1 - \cos(x) = 2\sin^2\left(\frac{x}{2}\right)$

$$\int_0^c e^{j\alpha z}\, dz = \frac{e^{\alpha jz}}{j\alpha}\Big|_0^c = c\,\frac{\sin(\alpha c)}{\alpha c} - j\left[\frac{2\sin^2(\frac{\alpha}{2}c)}{\alpha}\right]$$

$$= c\,\frac{\sin(\alpha c)}{\alpha c} + j\left[c\,\sin(\frac{\alpha}{2}c)\,\frac{\sin(\frac{\alpha}{2}c)}{\frac{\alpha}{2}c}\right]$$

$$= c\,\frac{\sin(\alpha c)}{\alpha c} - j\left[c\,\sin(\frac{\alpha}{2}c)\,\frac{\sin(\frac{\alpha}{2}c)}{\frac{\alpha}{2}c}\right]$$

Thus

$$\int_{-c}^0 e^{j\alpha z}\, dz = c\left[\frac{\sin(\alpha c)}{\alpha c} - j\sin(\frac{\alpha}{2}c)\,\frac{\sin(\frac{\alpha}{2}c)}{\frac{\alpha}{2}c}\right] \tag{B.2a}$$